BRAIN TISSUE MECHANICAL CHARACTERIZATION AND DETERMINATION OF BRAIN RESPONSE UNDER CONFINED BLASTS EXPLOSIONS

A Dissertation
Submitted to the Graduate Faculty
of the
North Dakota State University
of Agriculture and Applied Science

By

Asghar Rezaei

In Partial Fulfillment of the Requirements
for the Degree of
DOCTOR OF PHILOSOPHY

Major Department:
Mechanical Engineering

October 2015

Fargo, North Dakota

North Dakota State University
Graduate School

Title

Brain Tissue Mechanical Characterization and Determination of Brain Response under Confined Blasts Explosions

By

Asghar Rezaei

The Supervisory Committee certifies that this ***disquisition*** complies with North Dakota State University's regulations and meets the accepted standards for the degree of

DOCTOR OF PHILOSOPHY

SUPERVISORY COMMITTEE:

Dr. Ghodrat Karami
Chair

Dr. Mariusz Ziejewski

Dr. Fardad Azarmi

Dr. Kenneth Ruit

Dr. Kalpana Katti

Approved:

11/12/2015	Dr. Alan Kallmeyer
Date	Department Chair

ABSTRACT

Mechanical experimental tests including stress relaxation, simple monotonic ramps, and impact loads were performed on porcine brain tissues to investigate the response of the brain under different loading scenarios. Linear viscoelastic models were employed to determine the applicability and limitations of the linear mechanical models in tension. In addition the lowest and highest stress values, which can be possibly applied to the tissue due to change in the strain rates, were investigated using stress relaxation experiments to implicitly address the two levels of strain rates. Porcine brainstem samples were tested in six stress relaxation experimental settings at strain amplitudes ranging from 5% to 30% in compression. The lowest stress was directly measured from long-term responses of stress relaxation experiments when the stress values remained constant. The highest stress level was determined by using the quasi-linear viscoelasticity theory and estimating the instantaneous stress of the samples at six strain amplitudes. It was hypothesized that there is a correlation between the two pure elastic behaviors. The hypothesis was true as a strong linear correlation was found between the two elastic responses. The results showed that the instantaneous stress values were 11 times greater than the long-term stress values, practically similar across all strain amplitudes.

In the second part of the thesis, a number of computational studies were conducted using a validated human head model. The head model included major components of human head and underwent different blast scenarios in open and confined spaces. The study investigated the effect of reflections from the walls. The results show that when the head was in the vicinity of the wall, the biomechanical parameters were dramatically increased, especially in the corners. Comparing brain biomechanical parameters in confined, semi-confined, and open spaces under blast loads, the brain sustained greater stress and strain values, with larger duration of the loads, in confined spaces. Also, a primary blast injury (PBI) with a tertiary blast injury (TeBI) in a confined space was compared. The results indicated that the PBI due to the incident shock wave was much more injurious than TeBI due to blunt impact.

ACKNOWLEDGEMENTS

Foremost, I express sincere gratitude to my advisor, Dr. Ghodrat Karami, for his guidance, understanding, motivation, and immense knowledge, and most importantly, for his sincere friendship and continuous support during my graduate studies at NDSU.

I want to thank my committee member, Dr. Mariusz Ziejewski, for his guidance and support in my research. Special thanks go to my committee member Dr. Fardad Azarmi for his guidance in research and friendship throughout my PhD program. Also I am grateful to Dr. Kenneth Ruit from the University of North Dakota for agreeing to serve as a committee member and for his guidance and technical assistance in brain tissue preparation. I am also grateful to Dr. Kalpana Katti from the Department of Civil Engineering for agreeing to serve as a committee member.

My sincere thanks also go to Dr. Dan Dragomir-Daescu and Sean McEligot from the Division of Engineering at the Mayo Clinic in Rochester MN, for offering me a two-year graduate internship with financial support.

I also acknowledge the Army Research Office (ARO) for the financial support of this research. Special thanks to the Animal Science Department at NDSU for providing porcine brain tissues.

I also thank Mehdi Salimi-Jazi, Samad Javid, and Hesam Sarvghad-Moghaddam for their friendship and their technical assistance in my research as well as the Haugen family in Fargo ND and the Kvernen and Richardson families in Rochester MN for their sincere friendship and assistance.

Last but not the least, I gratefully thank my wife, Rafat, for her continuous support, her patience, her tolerance, and for allowing me the opportunity to pursue my study and finish my research, and I thank my parents for their spiritual support.

DEDICATION

I dedicate this thesis to my wife, Rafat; my children, Sheida and Arya; and also to my parents.

TABLE OF CONTENTS

LIST OF TABLES

Table Page

LIST OF FIGURES

CHAPTER 1. INTRODUCTION

1.1. Motivation

Brain injury is one of the leading causes of disability and death, occurring due to a wide range of incidents such as falls, sport injuries, traffic accidents, and war zone injuries (2). In battle fields, exposure to blast loads and bullet impacts are the main cause of traumatic brain injury (TBI). In blast scenarios, the mechanism of TBI is different, as there is no observable sign of skull fracture or external bleeding, and yet severe TBI occurs. Many civilians as well as military personnel undergo blast induced TBI. Due to the complexity of the situation, it is very difficult or impossible to determine the severity of TBI and take effective mitigation action. The situation is far more complicated if the blast occurs in enclosed spaces. Many reports show the rate of morbidity and mortality in such environments is much higher than in open spaces (3).

Understanding the mechanism of injury and how brain tissue responds to such loading conditions are of paramount concern to researchers in their quest to both promote preventive actions and to attenuate the severity of the trauma. Unfortunately, the literature is not mature in biomechanics of brain injury and there is a need for further analyses. This research is a computational and an experimental study that investigates blast induced TBI. In the experimental part, brain tissue will be characterized by performing several experiments to find the mechanical properties of the tissue which are necessary for computational studies. As the response of the tissue is dictated by the employed constitutive equation, a three dimensional (3D) nonlinear mechanical model is proposed to explain the behavior of the brain. The second part of this research study determines the mechanism of blast induced TBI in different spaces with a focus on confined spaces. The study investigates the effect of confinement and blast wave reflections on the injury-related biomechanical parameters such as intracranial pressure (ICP) and shear stress of a validated finite element head model. It captures an understandable image of what happens to the tissue in complex blast environments and computationally measures the severity of related injuries.

1.2. Background

On average, , about 1.7 million people sustain TBI each year in the US, of which 52,000 result in death (4). Even in the presence of cerebrospinal fluid (CSF) which cushions movement of the brain inside the skull, sudden movement of the brain due to impact loading or head kinematical motion can cause TBI (5). Most often, the impact on the head or neck can cause elongation of the brainstem in axonal directions and create damage. Such injury may cause death because the brainstem is the pathway for most cranial nerves, and it plays a vital role in basic attention and consciousness.

In the literature of the head injury biomechanics, computational studies, especially finite element analysis (FEA), are of great importance to help researchers determine various aspects of TBIs. Complex scenarios which are impossible to perform experimentally can be simulated, and if the models are well validated, a variety of significant results can be derived. FEA can accurately measure several injury-related biomechanical parameters at the tissue level including ICP, shear stress, and strain of brain tissue. In addition to macroscale analysis; modeling can be performed in smaller scales to determine the stresses on the axons and extra cellular matrix as well (6). However, the accuracy of the FEA depends on multiple parameters, one of which is the constitutive equation implemented for the material that dictates the estimated response of the material. Except for brain tissue, all the elements of the head can be acceptably modeled as elastic materials (7). Brain tissue, on the other hand, is materially complicated, showing both elasticity and viscosity in its mechanical behaviors. The governing equation of brain tissue plays the most important role in the prediction of the brain biomechanical parameters. An extensive variety of constitutive laws have been proposed for brain tissue in the literature. However, the complexities in brain tissue material, as well as the loading scenarios, have made it impossible for the proposed constitutive laws to accurately predict brain response under a multiple loading conditions.

1.3. Human Head Anatomy

The human head is the most vulnerable part of the human body and consists of many complex components. Several of the major head components play important roles in transferring loads to the brain. Of the major components, scalp is the outermost layer of the head. It is made of five different layers of soft tissues covering the bony structure. The skull, including 22 bones, houses the brain and plays the most protective role for the brain under head impact scenarios. The skull has a complicated geometry with the thickness ranging from 3.9 to 9.35 mm in men and from 3.4 to 8.2 mm in women. The occipital bone is the thickest bone found in the skull structure (8). The skull's geometry gives it the ability to absorb impact energy for the brain's protection. CSF is a fluid that occupies the space between the skull and the brain. Beside its important physiological functions, CSF has a vital influence on the reduction of transferred load to the brain and also prevents skull/brain contacts. The presence of fluid around the brain distributes pressure on the whole skull and brain.

The brain as a soft tissue is the most important and complicated part of the head. It weighs around 1.5 kg, almost one third of the head's weight. The brain is totally covered by a strong layer of pia mater. The brain consists of cerebellum, cerebrum, and the brainstem. The brainstem, which sends messages to different parts of the body, contains the pons, midbrain and medulla oblongata. The brain, comprised of white and gray matters, is buoyant in the CSF. Figure 1 illustrates in more detail the parts of a human head in a sagittal view (9). From a biomechanical point of view, the major head components provide protection for brain tissue.

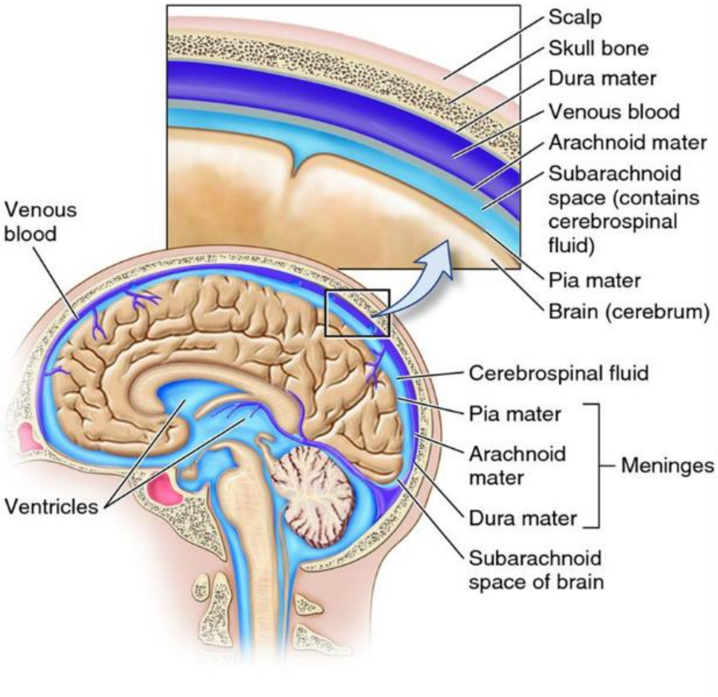

Figure 1. A sagittal view of a human head showing different layers (9)

1.4. Research Objectives and Scope

1.4.1. Material Characterization of Brain Tissue

The constitutive equations are of great importance in computational studies, as they may significantly influence the accuracy of the results. The primary objective of the experiments was to characterize the mechanical properties of porcine brain tissue and to investigate its responses under different loading conditions. Initially a number of mechanical tests were performed to validate the sample preparations, and to test the protocol and repeatability of the experiments. Then, different loading conditions such as creep recovery, stress relaxation, monotonic ramp, and loading/unloading conditions were applied to the samples of brain tissue. Several linear mechanical models were used to predict the response of the brain tissue in the linear region. Linear viscoelastic as well as Quasi-linear viscoelastic (QLV) equations were also implemented to mimic the tissue behavior in the nonlinear region. All mechanical tests were performed on brain tissue and brainstem tissue in macroscale.

1.4.2. Computational Analysis of Blast Induced TBI

The main goal of the computational studies was to determine the response of the human brain, in terms of injury-related biomechanical parameters, under blast loads when the head experiences blast wave reflections from the walls of confinement. In the first stage of the computational studies, the finite element head model, the wave propagation in the air domain, and its reflections from the walls were verified against different experimental studies. Then, several numerical investigations were conducted to examine the effect of reflections on primary blast injury (PBI) when the head was placed in the vicinity of a wall. In addition, the effect of different spaces; confined, semi-confined, and open; were investigated and the severity of PBI in the three situations were discussed. The translational effect of blast wind was also modeled as an important issue. PBI due to a direct shockwave incident was compared with a tertiary blast injury (TeBI) due to the blunt impact of the head with a confronting wall.

CHAPTER 2. MATERIALS AND METHODS IN EXPERIMENTAL STUDIES

2.1. Introduction

A large number of experimental investigations have been carried out for the last few decades. Numerous tests have been performed on human brain tissue in macroscale (for example: Estes (10), Galford & McElhaney (11), Bilston & Lawrence (12), and Donnely & Medige (13)). The majority of the research, on the other hand, characterizes brain tissue of animals such as rat, porcine, and bovine (6,11,14-16), mainly due to availability and also to minimize post mortem time for testing purposes (15).

Brain tissue, materially, is very complex to be treated as an engineered material in the determination of its characteristics. Different protocols and sample preparation techniques have been employed, due to a lack of standardization. Also, different sample shapes and sizes from several regions of the brain have been prepared for experimental purposes. There are also several differences between samples of one study to another such as animal sex, age, and breed. That is why a wide range of mechanical properties is found in the literature for any specific region of tissue (17). Therefore, to obtain consistent material properties of the brain, the literature of sample preparation needs to be thoroughly reviewed, and solid validations made in order to trust the results.

2.2. Sample Preparation

In this part of the experiments, several fresh porcine brains were acquired from the Animal Science Department facilities at North Dakota State University (NDSU) as by product. The animals were healthy, in the range of six months and older. The brains as well as their brainstems were removed from the head carefully. They were immediately put in a physiological saline solution to prevent dehydration and were transported to the laboratory. To prevent any mechanical decay, they were kept cold at 3 to 5 °C but not frozen. In Figure 2, a typical swine brain, brainstem and its parts are shown.

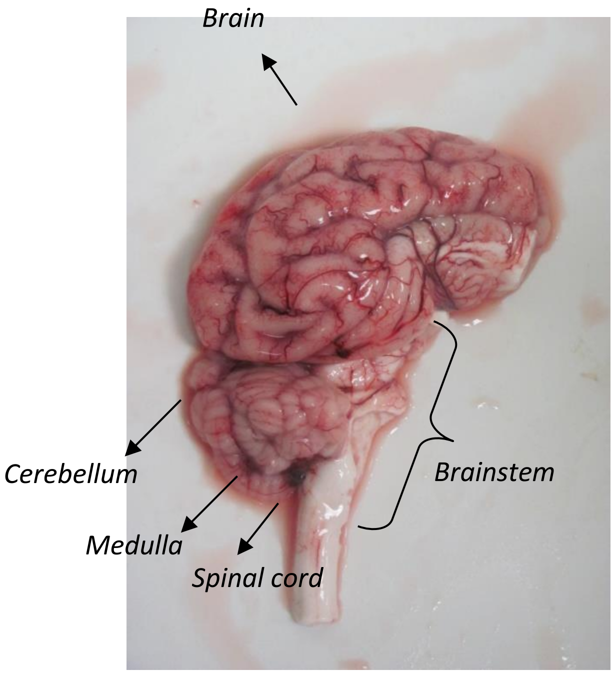

Figure 2. A hemisphere of the swine brain and the brainstem

2.3. The Mechanical Testing Machine

The test was performed at room temperature (~22 ◦C) using an Electroforce machine 3220 (Bose Corp, Eden Prairie, MN, USA). The machine is an accurate tool for macroscale characterization and can perform various types of mechanical tests. The machine has been widely used for brain tissue mechanical testing (17). A 2.5 N and a 20 N capacity high resolution load cell (Bose Corp, Eden Prairie, MN, USA) were utilized for the experimental purposes. All tests were conducted on the first day post mortem. The device can be easily switched to force or displacement control, which is necessary for different loading conditions. Care should be taken to correctly find the zero force and displacement, without any unwanted tissue deformation before starting the experiments. The device gives the operator the ability to move the upper platen precisely before starting the experiments.

2.4. Experimental Protocol

For different testing purposes, the samples were prepared from different regions of the porcine brain, including the brain and the brainstem. The tissue was very soft and could adhere to the tools. Therefore, different sample preparation methods were used for different regions of the brain.

2.4.1. Brain Tissue Samples

All tests were conducted within 14 hours post mortem. The brain tissue samples were excised from the frontal and parietal lobes of each hemisphere. The procedure followed the test protocol by Miller and Chinzei (14) for uniaxial compression tests. This made it difficult to cut small samples. In order to accurately cut the samples, a steel pipe with sharp edges was prepared to prepare samples, all in cylindrical geometry with the diameter of 25.4 mm. Also, surgical scalpels were used to cut the samples in 9 mm to 10 mm height. In terms of size, the samples were similar, which made the comparison of the results possible. The samples from brain tissue were used only for compression experiments. Figure 3 shows a cylindrical sample prepared for compression tests.

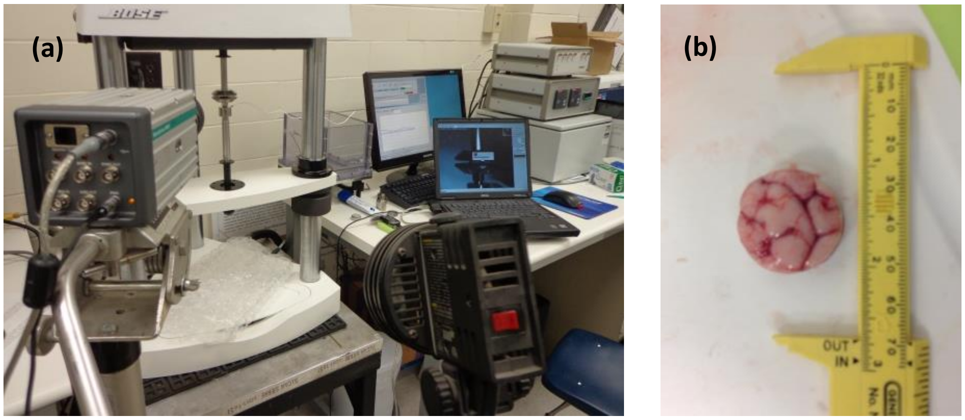

Figure 3. Sample preparation and experimental setup (a) the Electroforce machine (b) a cylindrical brain tissue sample for a compression test

2.4.2. Brainstem Tissue Samples

A number of samples were prepared from brainstem tissue. The parts of the brainstem harvested for some of the experiments were from the medulla oblongata and the transitional area between the medulla and spinal cord. This part of the brain is populated by axons and can be acceptably assumed to be a unidirectional composite. As samples from the brainstem were smaller than from the brain, sample preparation was more challenging. The accuracy of cutting the samples is important, as inaccurate cutting may contribute to errors in the stress and strain rate of the samples. Sharp surgical scalpels were used to carefully cut the specimens perpendicular to the axonal direction.

Brainstem samples were used for both tension and compression experiments. The ratio of length to width or diameter of the specimen was important, as an optimal ratio could guarantee the effect of stress concentration and stress triaxiality to be reduced. The lengths of the samples were based on the physical limitation of the specimens and the testing machine. As shown in Figure 4, the cross sectional areas of the samples had complex shapes and were difficult to measure. For accurate measurement, images of the cross sectional areas were provided before each individual test, and ImageJ software version 1.48 (Wayne Rasband, National Institutes of Health, USA) was used to precisely calculate the size of the areas.

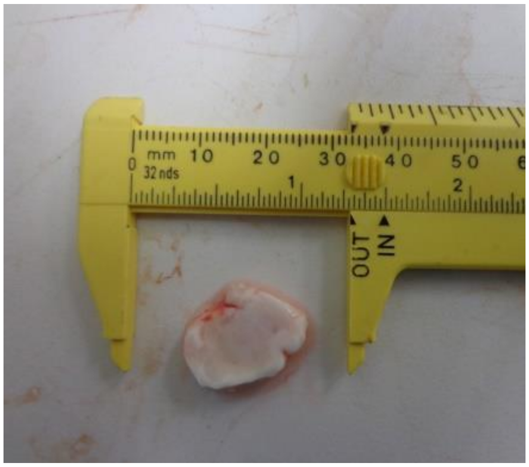

Figure 4. Cross sectional brainstem tissue sample prepared for compression tests

For tensile testing configurations, samples were prepared with the length of 18.5±1.5 mm (mean ± SD) and cross sectional areas of 70 to 100 mm^2. For compression tests, the samples were prepared with the length of about 5±0.7 mm (mean ± SD). The average cross sectional area was 93±30 mm^2 (mean ± SD).

To prepare for compressive loads to the tissues, the surface of each of the platen was humidified with a surgical lubricant (Surgilube, Fougera Pharmaceuticals Inc.) in order to approximate unconfined tissue compression. Samples were then carefully located on the lower platen and the upper platen was precisely moved downward until it touched the sample. A very small amount of load was applied to the tissue in order to guarantee a perfect attachment of the sample with platens.

To test in tension, cyanoacrylate, an instant type of glue, was used to connect the samples between the platens. Figure 5 shows the testing machine with a sample glued to the two platens for a stress relaxation experiment

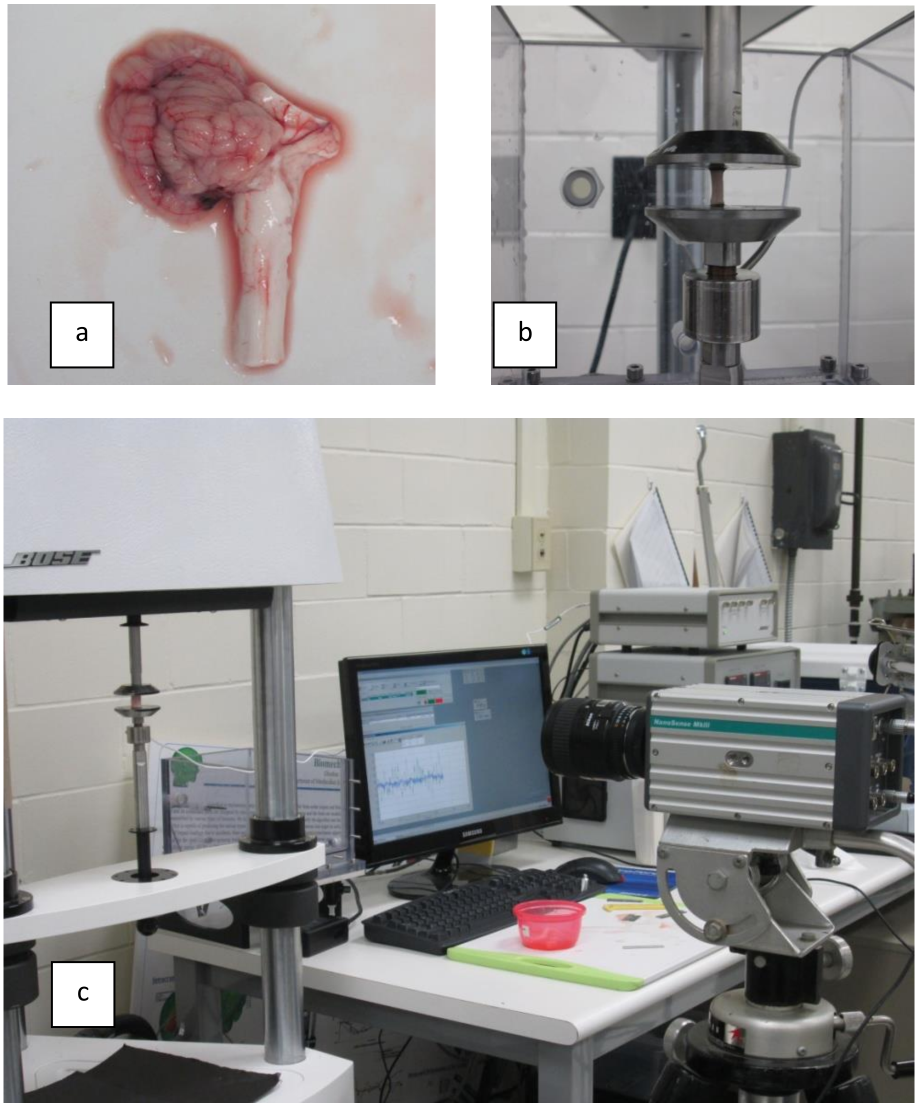

Figure 5. Sample preparation procedure and test protocol for the stress relaxation tests: (a) the brainstem cut from the porcine brain, (b) gluing the cylindrical sample of the brainstem between two platens, (c) Electroforce machine ready for the test with a high speed camera to record sample deformation

The procedure of testing was similar to that of Miller’s work (18) in which the tissue was subjected to an applied load in tension. To assure appropriate attachment, the upper platen was moved downward in such a way that the sample contacted the lower platen that was already glued. The testing device gives the operator the ability to move the upper platen precisely before performing the experiments. All tests were performed 30 seconds after attachment for assurance that the tissue was strongly attached to the platens. During the tests, observations were made to ensure a uniform attachment and homogeneous deformation, which guarantees an accurate macroscale characterization.

2.5. Mechanical Testing on Tissue Samples

Simple monotonic ramps, creep recovery, and stress relaxations in both tension and compression were performed on brain tissue samples. As expected, the behavior of the viscoelastic materials changes with time, and that the strain rate plays a major role on the response of the samples. Simple tensile or compressive tests might not be suitable for viscoelastic material characterization as the samples behave differently under various rates. Stress relaxation tests, on the other hand, can be conducted by the convenient method of applying a sudden strain and keeping it constant over a period of time. The stress decays and the deflection can be measured and monitored over time. As the test is applied to the substances under a constant strain, the effect of strain rate would be eliminated. More importantly, the response of the substance in the linear region is a scale of relaxation modulus and can be simply derived. Creep recovery is also similar to a stress relaxation test where a sudden force is applied to the sample and kept constant over time. Creep recovery, however, is technically difficult to perform by mechanical testing machines when the amounts of applied loads are very small. In case of soft tissue samples, the machines cannot follow a high force rate.

2.5.1. Mechanical Testing in Tension

Stress relaxation tests were conducted in tension on brainstem samples to determine the viscoelastic parameters of the substance at 3% strain level under small deformation analysis. The initial strain rates in the relaxation tests were about 5.55/sec for all samples, taking about 6 milliseconds to reach a 3% strain level. In Figure 6, the averaged value of the stress function with time is depicted for 10 specimens, including their standard deviations. The tests were performed on samples at the mentioned strain level (3%) in which the tissue behaved linearly (19). The error bars show the variation and limitation in the results for different tests conducted on specimens due to variation in samples, errors in data acquisition, as well as errors in locating the zero stress and strain in the onset of the loading. A major part of the error comes from the initial part of the test, i.e., calculating the instantaneous response of the tissue. It should be mentioned that the results of the stress relaxation at 3% strain level were used to derive material properties of axons and extra cellular matrix in microscale level (6).

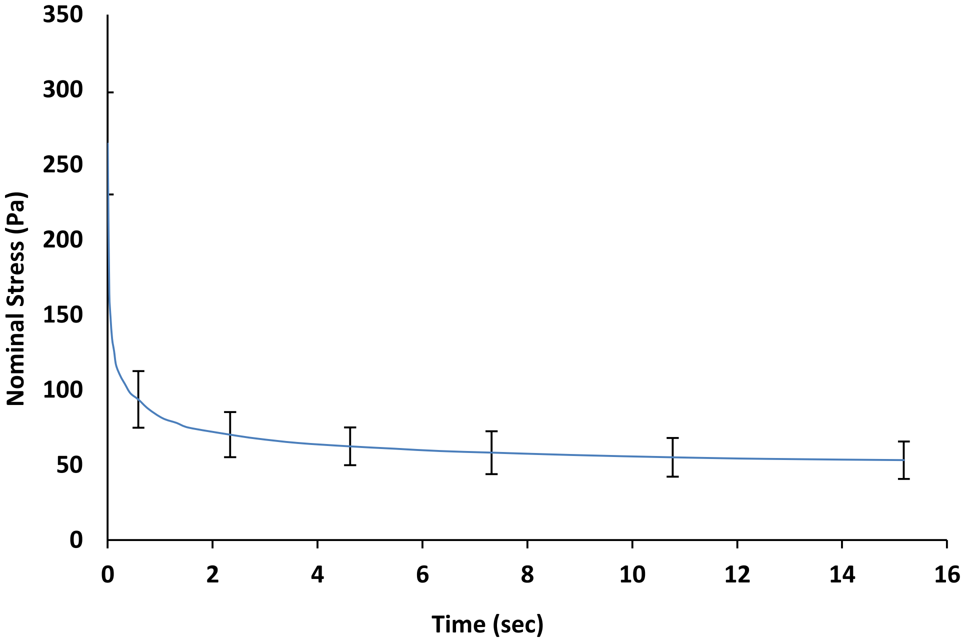

Figure 6. The averaged stress relaxation test results in tension on the swine brainstem at 3% strain including the error bars

Also simple tensile monotonic ramps were performed at two strain rates including 5×10^{-4}/s as a slow loading rate and 5×10^{-1}/s as a high loading rate (Figure 7). Due to increase in strain rate, the nominal stress increased up to about four times, showing rate dependency of the tissue. Additionally, loading-unloading scenarios were performed on brainstem tissue at strain rates of 0.3/s and 0.003/s (Figure 7).

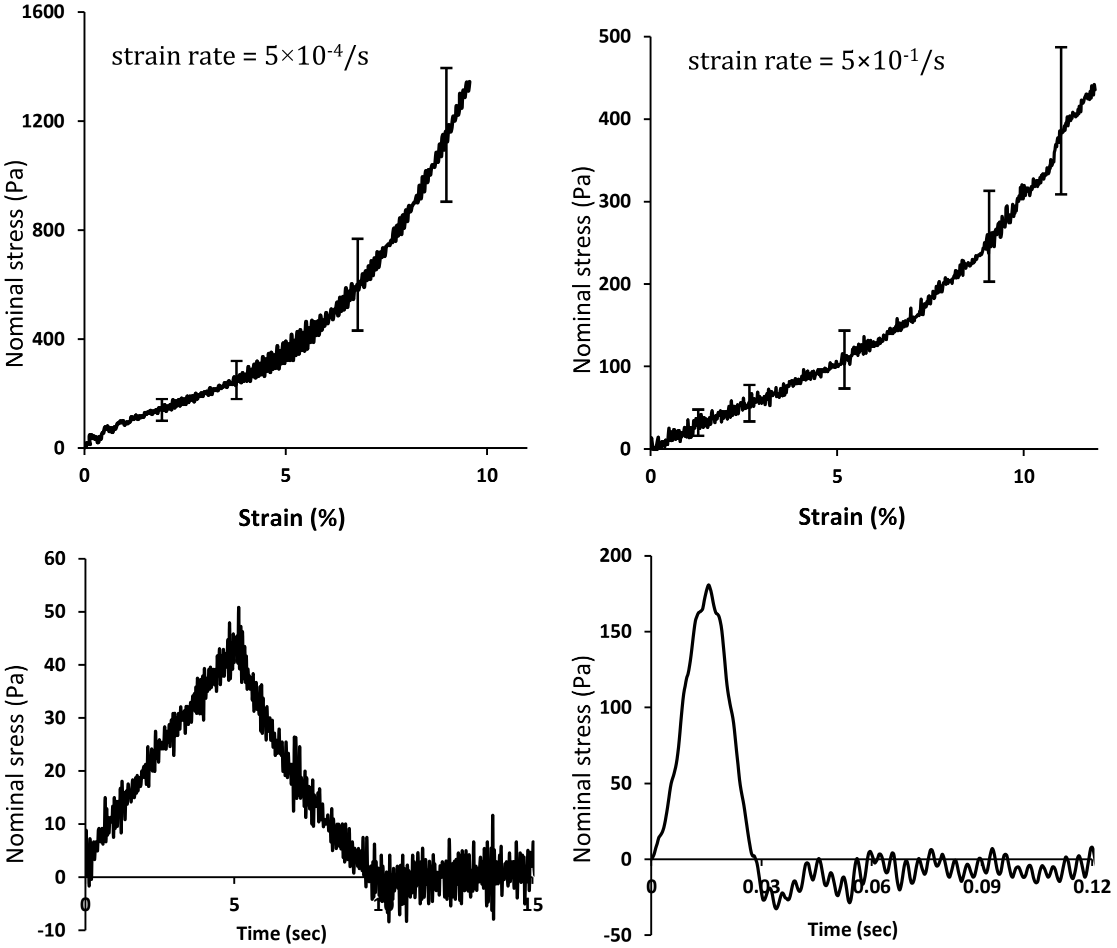

Figure 7. Tensile monotonic ramps and loading/unloading conditions in tension on brainstem tissue at different strain rates

2.5.2. Mechanical Testing in Compression

For brainstem tissue samples from the medulla oblangata, stress relaxation tests were conducted at 6 nominal strain amplitudes of 5% (n=4), 10% (n=3), 15% (n=4), 20% (n=4), 25% (n=4), and 30% (n=3) in compression. The ramp part of the test was set to 20 mm/s, at which noises and vibrations from the machine did not significantly affect the response of the tissue. The results of nominal stresses on the brainstem samples were averaged at each strain level as shown in Figure 8. The initial maximum stresses from stress relaxation tests varied from about 400 kPa at 5% strain value to 3600 kPa at 30% strain value.

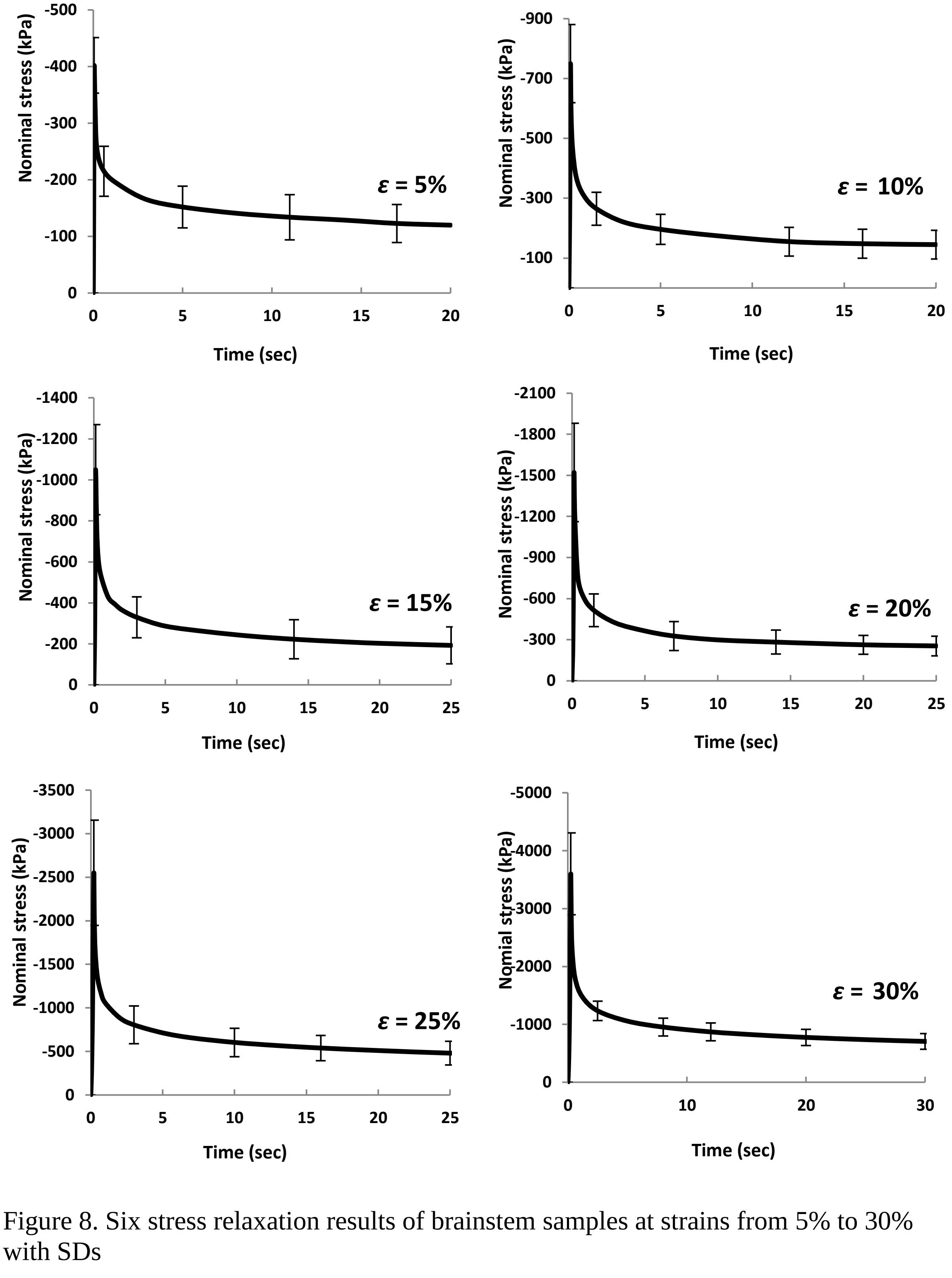

Figure 8. Six stress relaxation results of brainstem samples at strains from 5% to 30% with SDs

The implementation of mathematical equations was done by Matlab R2010a (The Mathworks, Natick, Massachusetts) and Mathematica Wolfram 8 (Wolfram Research Inc., Champaign, Illinois). The JMP version 10.0.0 (SAS Institute Inc., NC, USA) was also used for all the statistical analyses in this study.

2.5.3. Experimental Validations

Unlike many engineered materials, no standard protocol is available for testing soft biological tissues such as brain. However, the results of the study can be compared with similar published data from literature. For porcine tissue, we could not find any studies on similar regions of the brainstem to compare with our results. However, for other regions of brain tissue, we found several studies and compared their results with our results of monotonic ramps and stress relaxation experiments. For the porcine brain tissue samples, stress relaxation experiments were performed at 50% initial strain (n=2) and simple monotonic ramp compression tests at strain rates of 0.64/s (n=2) and 0.1/s (n=3). Figure 9 shows the results from stress relaxation and simple ramp experiments in compression on porcine brain tissue samples in this study along with similar results from two previous studies by Miller and Chinzei (14) and Prevost et al. (17). As shown, the results are very similar among studies with the largest difference found in stress relaxation comparisons when the difference in stress varied from about 330 Pa to 540 Pa (Figure 9c). All the stresses and strains were nominal. The initial maximum stresses from stress relaxation tests varied from about 400 kPa at 5% strain value to 3600 kPa at 30% strain value.

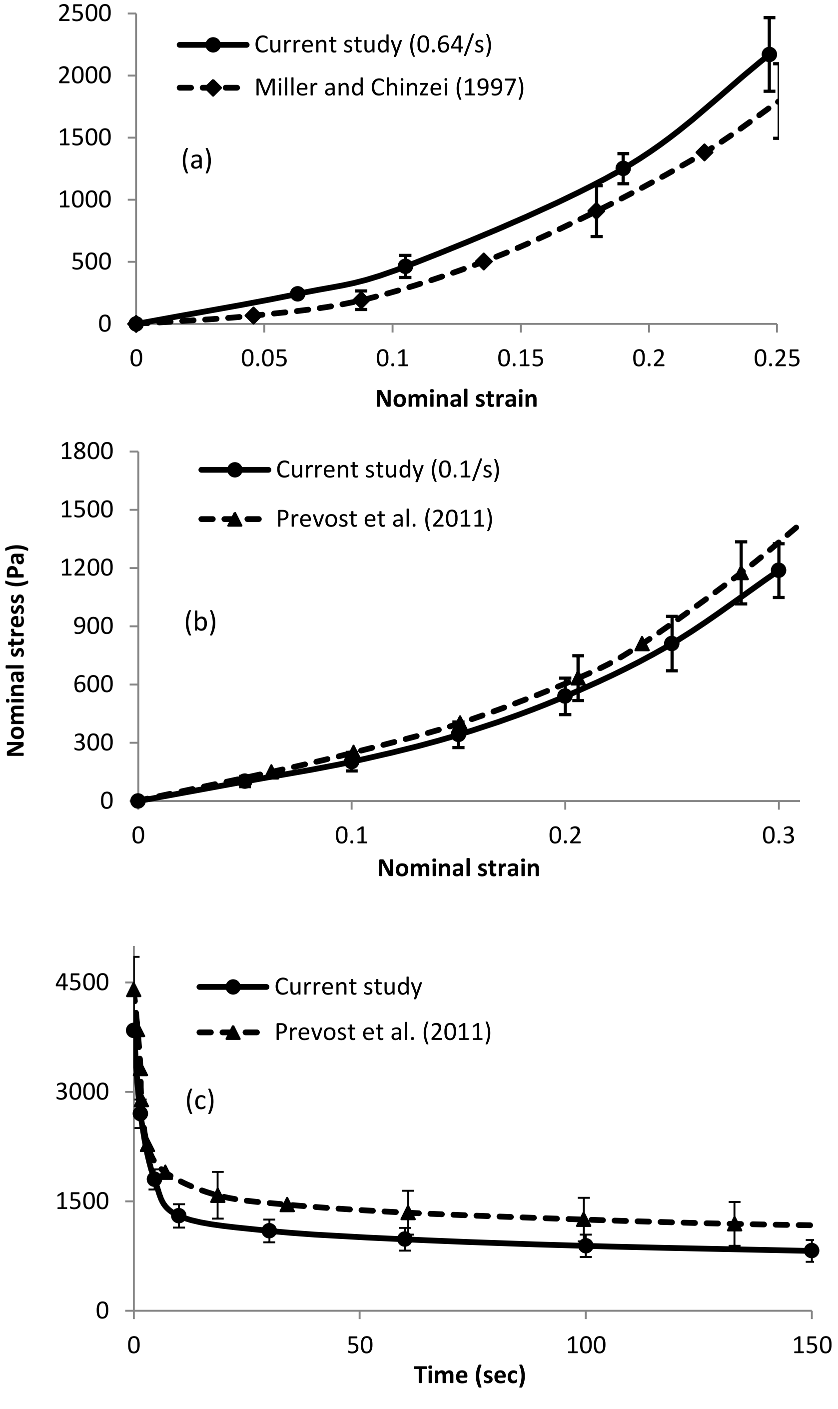

Figure 9. Results of the experimental data compared with previous studies; simple monotonic compression tests (a) at the rate of 0.64/s; (b) at the rate of 0.1/s; and (c) stress relaxation at 50% strain level

With regard to experimental setting, the testing protocol for brain tissue was similar to the protocol used for brainstem tissue. The only difference was the use of a more accurate and sensitive load cell for the smaller brainstem specimens for which smaller amounts of force were needed. Good agreement was found between our results and the results from previous studies. The largest difference was found between the results of our stress relaxation study and those of Prevost et al. (17). This difference was likely due to the fact that the samples in the research of Prevost et al. (17) were preloaded by about 30 Pa which may possibly have affected the estimated stress values.

CHAPTER 3. BRAIN TISSUE LINEAR CONSTITUTIVE EQUATIONS

3.1. Introduction

Compared to other parts of the brain, there is little data available on the mechanical properties of the brainstem. In an experimental computational study, brainstem tissue was used under stress relaxation testing to estimate the material characteristics of brain tissue constituents in microscale (6). They found the viscoelastic characteristics of axons and extra cellular matrix using an optimization method in the linear region of the tissue. Experimental tests were conducted in the study of Arbogast et al. (20) on porcine brain tissue from the pons, as part of the brainstem, to estimate its shear relaxation function based on a quasi-linear viscoelasticity constitutive behavior assumption. Three levels of peak strain (2.5%, 5%, and 7.5%), with the strain rate of greater than 1/sec, have been considered to investigate the directional dependence of the material characteristics. In another study, Arbogast and Margulies (19) performed oscillatory shear tests on adult swine brainstem in three perpendicular directions, with samples taken from the middle to the upper parts of the brainstem. They calculated complex shear moduli with a range of frequencies between 20-200 Hz, for three different strain levels, in which the substances may have been assumed to behave quasi-linearly. They showed that the brainstem exhibits considerable transversely isotropic behavior. They also performed a similar experiment on cerebral tissue and concluded that the brainstem shows a stiffer response. Ning et al. (21) have introduced a constitutive response formula for the brainstem under large shear deformations. They considered the brainstem as a transversely isotropic viscoelastic material and characterized it in three mutual directions. They used a combined method of a genetic algorithm optimization as well as finite elements to determine the mechanical properties of the brainstem.

For constitutive characterization of human or animal body tissues, linear viscoelastic models have been widely used. Although such models are approximate, they are systematic, simple, and easily understandable. In this respect, it is proved that viscoelastic resemblance provides a good modeling of the tissue behavior. A series of creep and stress relaxation experimental data on brain, dura, and scalp of human and monkey tissue has been reported by Galford and McElhaney (11), in which the behavior of the tissue was represented by a four-element viscoelastic model. They determined the parameters of the model, showing a close creep compliance curve with the experimental data. Estes (10) has conducted an investigation on the human brain and interpreted its mechanical properties in terms of a standard-solid viscoelastic model, a combination of a Kelvin model and a linear spring in series, and determined the mechanical parameters of the tissue model as $R_1 = 27.58\ kPa$, $R_2 = 13.03\ kPa$ and $\eta_2 = 2.17\ kPa\text{-}s$ where R_1, R_2 and η_2 are springs and dashpot constants, respectively. Bilston and Lawrence (12) have performed a series of tensile experiments on human cervical spinal cord at different strain rates and interpolated the data by parameters of a four-element viscoelastic model. They determined their viscoelastic model parameters of the springs and dashpots as $R_1 = 0.65 \pm 0.36$ and $R_2 = 10.6 \pm 8.2\ MPa$, $\eta_1 = 119 \pm 49\ MPa\text{-}s$, and $\eta_2 = 15.0 \pm 13.1\ MPa\text{-}s$. In another effort, Donnely and Medige (13) have used a standard-solid model to characterize the shear properties of human brain tissue. They obtained the following data for brain tissue; $R_1 = 550\ Pa$, $R_2 = 291\ Pa$ and $\eta_2 = 9.4\ Pa\text{-}s$.

It is acknowledged that brain tissue inherently has a nonlinear viscoelastic behavior (13,14,22). However, the tissue similar to the majority of viscoelastic materials behaves linearly under small deformation and the employment of linear viscoelastic constitutive models under such conditions is reasonable. In this regard, several research characterizing schemes have been introduced to measure the linear viscoelastic characteristics of human brain tissue (23-26). Such models have been widely implemented in commercial software packages such as Ls-Dyna (Livermore Software Technology Corp., Livermore, CA, US) and Abaqus (Abaqus Inc., Providence, RI, US). The purpose of these studies has been to determine the level of stresses/strains on linear viscoelastic brain tissue under a wide range of conditions from low velocity impacts to complex blast load scenarios (27-30). However, it must be emphasized that the precise degrees of accuracy and approximation in simulation of such nonlinear behavior with these linear models are still unknown.

The overall objective of this chapter was to show the credibility and to examine the accuracy of various types of linear mechanical viscoelastic models to properly simulate the characteristics of porcine brainstem. The predictions by standard-solid, Zener, four-element, and three-term Prony series models, as representatives of linear viscoelastic behavior, were to be examined against the experimental brainstem response with tensile stress relaxation at 3% strain. The unknown coefficients of the constitutive equations for all the models were estimated and then the ability of each model to predict the behavior of tissue samples was determined. Also, the tissue behavior under tensile ramps as well as impact strains was examined to verify the applicability of the models.

3.2. Linear Viscoelastic Models

Since the simplest forms of viscoelastic mechanical models, Voigt and Maxwell, which include only one spring and one dashpot, cannot predict reasonably the response of viscoelastic materials, various combinations of these two models, with addition and assemblage of different mechanical elements, have been widely introduced (Figure 10) (10-13).

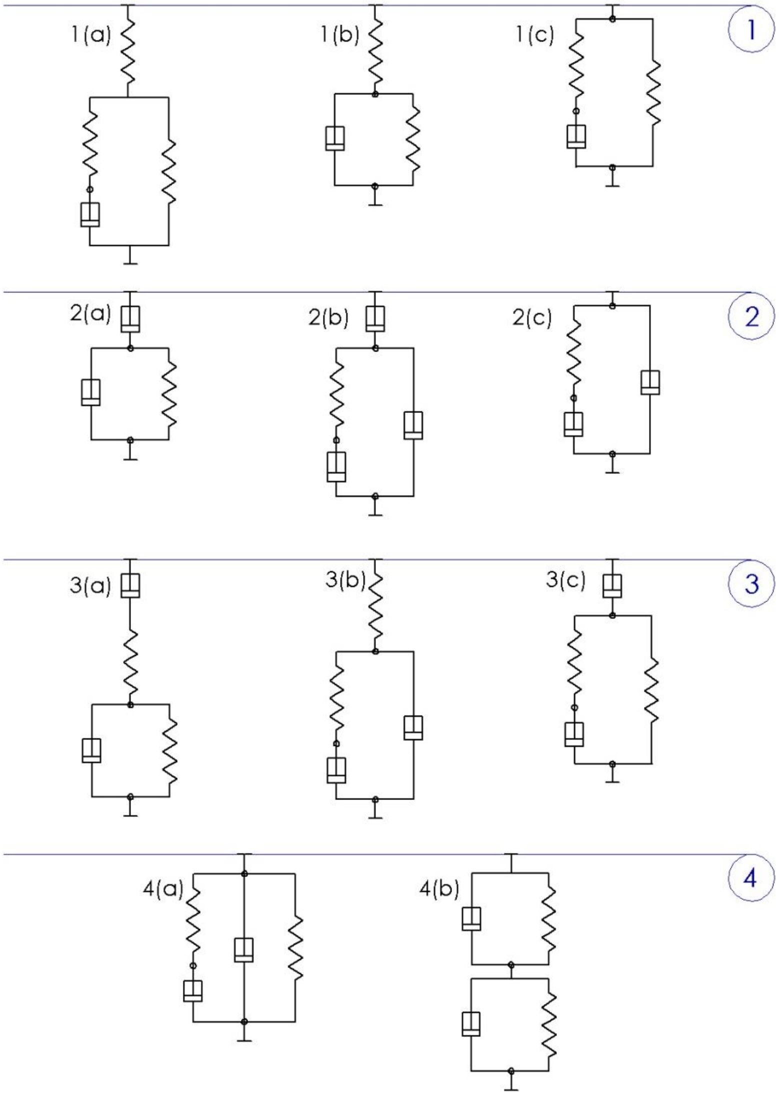

Figure 10. Four groups of mechanical models which are the basic three-element or four-element mechanical models or combinations of them

Among the models shown in Figure 10, group 1 shows a solid-like behavior with instantaneous and delayed elastic deformation. Models 1b and 1c in this group are known as the “standard-solid”. Model 1c, is also referred to as the Zener model. Group 2 exhibits liquid-like characteristics with viscous flow and a delayed elasticity property. Also, Group 3 has an instantaneous elastic response followed by viscous flow and a delayed elastic behavior. In group 3, model 3a is known as “four-element” or Burger model, which consists of simple Voigt and Maxwell models in series. Finally, group 4 represents delayed elasticity behavior with two retardation times (31).

The Zener, standard-solid, and four-element models were considered in this study, as they have been examined by a number of researchers to materially model the human brain under impact conditions (11-13).

Having digitized the behavior of the brainstem experimentally, the linear and nonlinear viscoelastic models and the Prony series was used to simulate the tissue behavior. The experimental data was thus fitted to the assumed constitutive simulation model equation. An optimization procedure was employed to find the parameters of the assumed constitutive model. The technique for the fitting procedure was a nonlinear least-square method to search the best fit for the measured data (Mathematica, Wolfram). The parameters of the springs and dashpots and the parameters of the Prony series were estimated. Tensile ramps as well as triangular loads were also applied to samples with different loading speeds, to verify the solutions and to examine the effect of strain rates on the tissue response and, most importantly, to determine the performance and reliability of the models under such conditions. Once the mechanical properties of the tissues are correctly obtained, it is possible to predict the behavior of the substance under different tensile scenarios.

3.2.1. Zener Model

This model is a combination of the Maxwell and an elastic spring in parallel (Figure 11a) and is more realistic than the simple Maxwell and Voigt models in predicting the response of the tissue material under stress and strain. The governing equation of the Zener model can be written as:

$$\frac{\eta_1}{R_1}\dot{\sigma} + \sigma = \left(1 + \frac{R_2}{R_1}\right)\eta_1\dot{\varepsilon}_2 + \varepsilon R_2 \tag{1}$$

The Zener model yields the following time-dependent stress relaxation function under a displacement ramp:

$$\sigma = \varepsilon_0\left(R_2 + R_1 e^{\frac{R_1}{\eta_1}t}\right) \tag{2}$$

In the above equation, ε_0 denotes the sudden strain on the samples. The parameters of this constitutive equation can be found through the optimization procedure, once it was fitted to the experimental stress relaxation data of tissue. The values for the parameters were found R_1 = 6.14 *kPa*, R_2 =2.31 *kPa*, η_1 = 0.53 *kPa-s*.

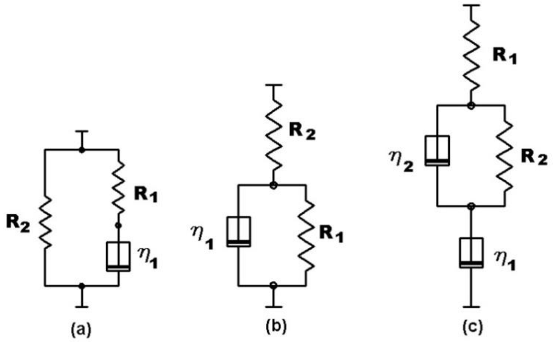

Figure 11. The three most well-known mechanical models; (a) Zener, (b) standard-solid, (c) four-element

3.2.2. *Standard-solid Model*

This model is a combination of simple Voigt with an elastic spring in series (Figure 11b). This model can realistically predict the response of the tissue material under stress and strain. The governing equation of the model can be written as:

$$\frac{\eta_1}{R_1R_2}\dot{\sigma}+\frac{R_1+R_2}{R_1R_2}\sigma=\frac{\eta_1}{R_1}\dot{\varepsilon}+\varepsilon \tag{3}$$

If a sudden constant strain, ε_0, is applied to the standard-solid model, its constitutive law yields the time-dependent stress as:

$$\sigma=\frac{\varepsilon_0R_2}{R_1+R_2}\left(R_1+R_2e^{-\frac{R_1+R_2}{\eta_1}t}\right) \tag{4}$$

Using the optimized solution procedure, this equation yields the following numeric values when fitted to the tissue experimental data: $R_1 = 3.17$ *kPa*, $R_2 = 8.45$ *kPa*, $\eta_1 = 1.00$ *kPa-s*. Figure 12 shows the response of the tissue and the predicted values obtained from application of different mechanical models. While the constitutive equations of the Zener and the standard-solid are different, the responses of both models coincide. This can be explained by the fact that both are comprised of two springs and one dashpot with different layouts leading to the same constitutive equations. Apparently the locations of the components have no major impact on the outcome. As shown in Figure 12, both of these three-element mechanical models correlate well with the experimental data. However, the predicted stress decays earlier than experimental data. This indicates the incapability of the model in precise prediction of the viscous response of the brain tissue.

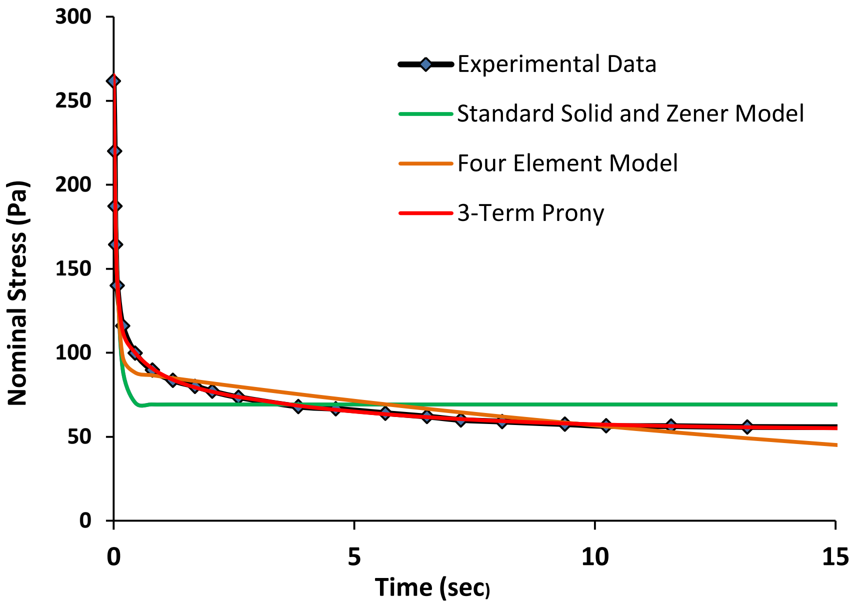

Figure 12. Tensile stress relaxation experimental data at 3% strain along with the responses mechanical models and three-term Prony series

3.2.3. Four-element Model

As depicted in Figure 11c, this model is a combination of Maxwell and Voigt models in series. The four-element model has been used with fair success in predicting linear behavior of brain tissue (11) and is rather an accurate predictor for stress relaxation and creep-recovery tests. The constitutive law of the model is a second order differential equation as follows:

$$\sigma + \left(\frac{\eta_1}{R_1} + \frac{\eta_2}{R_2} + \frac{\eta_3}{R_3} \right) \dot{\sigma} + \frac{\eta_1 \eta_2}{R_1 R_2} \ddot{\sigma} = \eta_1 \dot{\varepsilon} + \frac{\eta_1 \eta_2}{R_2} \ddot{\varepsilon} \tag{5}$$

The four-element model predicts the stress relaxation under a displacement ramp as follows:

$$\sigma = C_1 e^{pt} + C_2 e^{qt} \tag{6}$$

with

$$p,q=\frac{-R_1\eta_1-R_2\eta_1-R_1\eta_2\mp\sqrt{-4R_1R_2\eta_1\eta_2+(R_1\eta_1+R_2\eta_1+R_1\eta_2)^2}}{2\eta_1\eta_2}$$

and

$$C_1=R_1\varepsilon_0-\frac{R_1\varepsilon_0-A}{p-q},\qquad C_1=\frac{R_1\varepsilon_0 p-A}{p-q}\quad\text{with}\quad A=-\varepsilon_0R_1^2\left(\frac{\eta_1+\eta_2}{\eta_1\eta_2}\right)$$

By fitting this equation to the experimental stress relaxation data of the brainstem, the constitutive parameters of this model were extracted. Considering the similar properties of these models as shown in Figure 12, the four-element model behavior is relatively acceptable. The four-element model behavior also deviates from the experimental data in a longer duration and thus is not a good predictor for the long-term characteristics of the substance. The constitutive coefficients were derived through optimization by fitting the experimental data and the results obtained are: R_1 =8.7, R_2 =4.64 *kPa*, η_1 =5.58 and η_2 = 0.84 *kPa-s*.

3.2.4. Prony Series Models

In examining the mechanical properties of a linear viscoelastic material under an arbitrary loading condition, deformation history plays an important role. The constitutive equation of a solid viscoelastic material is time dependent and includes the history of deformation. A common form for these constitutive laws can be represented by the Prony series form. Also, among many curve-fitting techniques, the Prony series, as a response to generalized Maxwell model, are repeatedly adopted because of the precise fitness to the data, and their simplicities and capabilities in mathematical manipulations. To present the constitutive law in the form of the Prony series, the stress function of the tissue in linear region can be expressed as follows (32):

$$\sigma = E(t)\varepsilon_0 \qquad E(t) = E_0\left[\alpha_\infty + \sum_{i=1}^{N_E} \alpha_i{}^E e^{(-\frac{t}{\tau_i^E})}\right] \tag{7}$$

Where *E(t)* is the relaxation function, N_E the number of components, E_0 the short-term modulus, τ_i^E the relaxation time of each Prony series component. Also α_∞ and $\alpha_i{}^E$ are the relative moduli. Eq. (7) is valid when the duration of the initial ramp in the stress relaxation test is very small compared with the smallest relaxation time of the tissue. In this situation, the tissue reacts as an elastic substance for the instantaneous ramp. Otherwise, quasi-linear viscoelasticity must be implemented. E_0, the short-term modulus is the modulus at the fast load limit. The long-term modulus, E_∞ in tension can be derived as follows:

$$E_0 = \alpha_\infty + \sum_{i=1}^{N_E} \alpha_i{}^E \qquad E_\infty = \alpha_\infty E_0 \tag{8}$$

Three-term Prony series were fitted to the experimental data and the coefficients were found through the optimization procedure. The data computed from the sample data for the relaxation times τ_i^E are 0.044, 0.519, and 4.17 sec and the relative moduli α_i^E are 0.54, 0.136, and 0.12, respectively. In Figure 12, the Prony series predictions are compared with the experimental data for 3% strain level. It can be concluded that three-term Prony series illustrates a very good agreement with the experimental data. Based on the stress functions, the relaxation functions decaying moduli are calculated and are shown in Table 1.

Table 1. Relaxation function, *E(t)*, for the models

Models	**Relaxation functions (kPa)**
Standard-solid and Zener	$2306.95 + 6138.27e^{-t/0.0865}$
Four-element	$5706.83e^{-t/0.0629} + 2994.74e^{-t/21.786}$
Three-term Prony	$1802.43 + 4773.66e^{-t/0.044} + 1064.11e^{-t/0.52} + 1201.82e^{-t/4.177}$

Short-term and long-term moduli can be derived from to the results listed in Table 1. The short-term modulus is equal to the relaxation modulus at time zero, while the long-term modulus is the modulus when time goes to infinity. The values for these parameters are presented in Table 2.

Table 2. Short-term and long-term moduli (Pa) of the brainstem for different models

Models	**Short-term Modulus**	**Long-term Modulus**
Standard-solid and Zener	8445	2306.95
Four-Element	8701.57	0
Three-term Prony series	8824	1802.43

3.3. Efficiency of the Models

The Mechanical behavior of the tissue can be predicted under different circumstances such as tensile ramps after characterization of its mechanical properties. For this purpose, some experiments were performed on the brainstem under tensile loads at two different strain rates. Using the relaxation function of the models, *E(t)*, one can theoretically apply a simple tensile ramp similar to the experiments on the samples using a convolution integral stress function as follows (31):

$$S = \int_0^t E(t-\tau)\frac{\partial \varepsilon}{\partial \tau} d\tau \tag{9}$$

Figure 13 shows the response of the samples and all of the models under tensile tests at two different strain rates of 5×10^{-4} and 5×10^{-1} sec^{-1}, respectively.

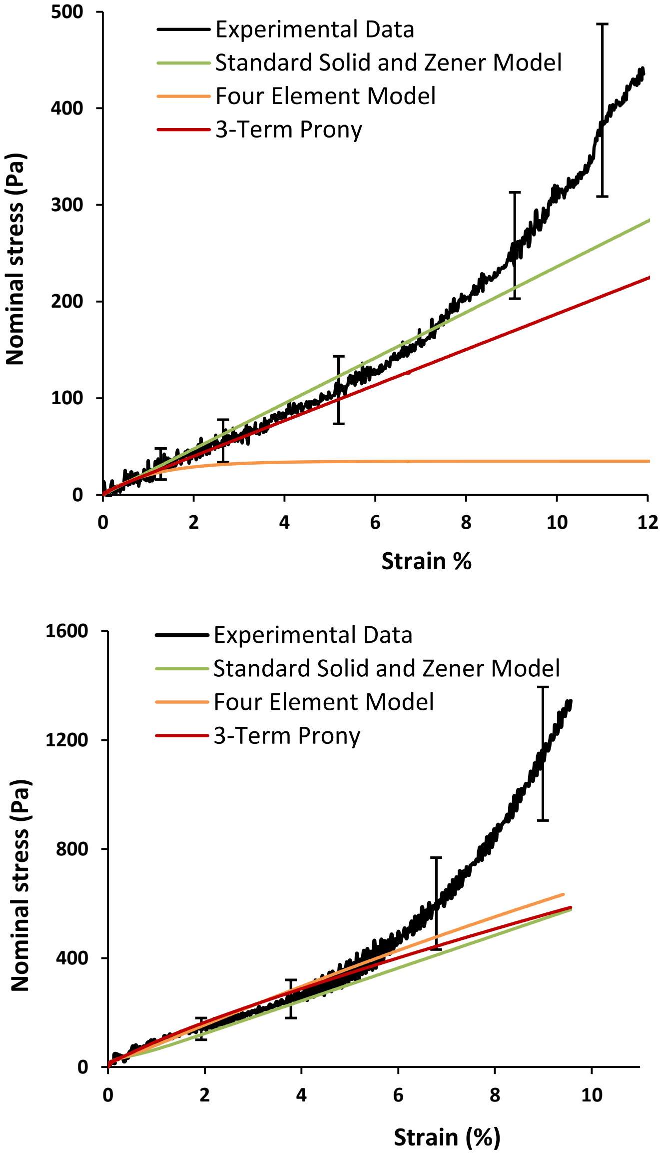

Figure 13. Tensile tests on the brainstem together with the responses from mechanical models and Prony series at the rate of (a) 5×10^{-4}, (b) 5×10^{-1} sec^{-1}

As can be seen in Figure 13a, all linear models, with the exception of four-element, can nearly predict the response in small deformation (stains up to 6%) with the three-term Prony series showing better performance. These linear models however fail at higher strains. At the strain rate of 5×10^{-1}/sec, linear models follow the tissue behavior similarly (Figure 13b). The models correlate well with the tissue behavior under 6% strain, but their predictions further than that deviate very much from the true tissue behavior. This can be explained that linear mechanical models can follow the brainstem tissue in small deformation (up to 6%), regardless of the strain rate. The independency from strain rate in this region can be verified in Figure 14 where the samples are subjected to tensile impact strains (about 1.5%) with two different frequencies (0.1 and 40 Hz).

The linear models follow the tissue behavior accurately under both mentioned strain rates. Interestingly, at the high strain rate, all of the models show similar performance, regardless of the number of dashpots or springs in the model, due to the fact that only springs are responsible for bearing the load and the dashpots lock up at such rates.

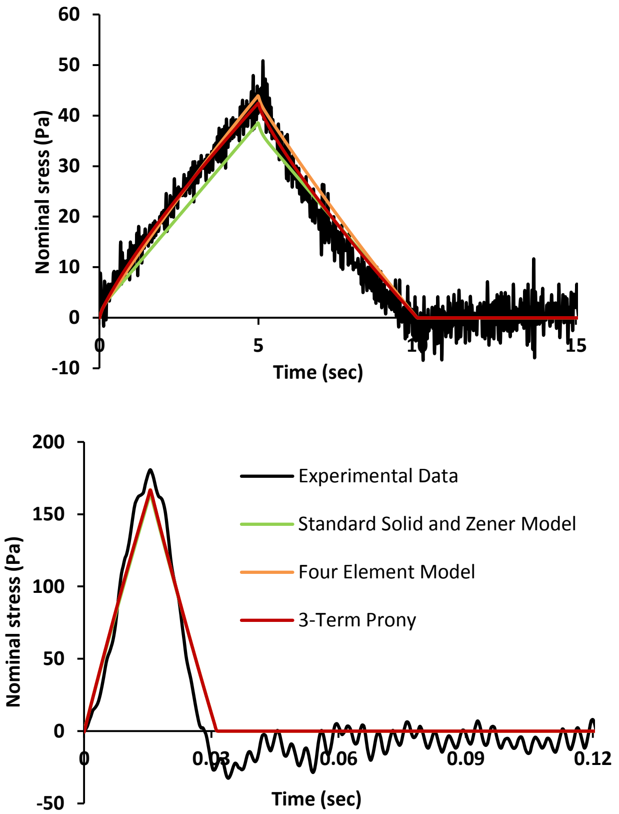

Figure 14. Two different impact strains on the samples in small deformation (1.5% of strain): (a) low strain rate; (b) high strain rate. For the sake of simplicity, only the positive parts of the models' response are calculated, and the time history behaviors after

The tensile stress-strain curve of the brainstem can be divided into the three regions as shown in Figure 13; the first region is a small nonlinear region in the very beginning of the tissue response, followed by a second region of almost linear behavior up to 6% strain. The third region, which is fully nonlinear, shows the slope of the stress-strain curve is increasing. In this region, depending on the strain rate, a small increase in strain may contribute to a notable increase in stress. The linear models can only predict the response of the tissue in the first and second regions approximately, and they essentially fail to predict the behavior in the third region.

Three-term Prony series and standard-solid models show maximum and minimum correlations, that is, 0.998 and 0.974, respectively. These results show an acceptable correlation with the tissue behavior. As the number of elements in the rest of the mechanical models increases, the resemblance improves, as shown by their correlation factors. The Prony series with three terms aptly describes the behavior of the brainstem under stress relaxation. The correlation for the tensile ramp with lower strain rate indicates that the four-element model does not work properly in such situations. The reason is that the long-term modulus of the model goes to zero (Table 2), and as the duration of the tensile ramp is far more than the relaxation times of the model, the level of stress remains constant after the duration goes beyond the largest relaxation time.

3.4. Conclusion

In this chapter, the experimental as well as the predicted results were presented by linear viscoelastic constitutive models for the response of the porcine brainstem under stress relaxation, tensile ramp, and impact strain loadings. Different loading scenarios were applied to the tissue and compared with the models to address the validity and applicability of different linear models. The models' predicted constitutive equations were interpolated by the experimental data and their parameters were extracted by optimization. Under a stress relaxation scenario, the standard-solid and Zener models illustrated identical behavior with a fairly good resemblance to the tissue response, as they have the same form of equation. The four-element model was found to have a good trend with the tissue, but still cannot predict the long-term behavior. Three-term Prony series, on the other hand, were found to appropriately fit the experimental data and can accurately simulate the behavior of the brainstem under stress relaxation. It indicates that increase in number of terms results in the more accurate simulation. The tensile tests, on the other hand, illustrated that the performance of linear models were acceptable only up to about 6% of strain (small deformation), regardless of the loading rate. The impact strain applied to the tissue verified the independency of the performance of the linear models on the strain rate in small deformation. For larger deformation, the linear models kept deviating from the response of the real tissue. Consequently, the extent of their application is not advised in larger deformation, as such linear models may overestimate/underestimate the response of the tissue under such conditions.

CHAPTER 4. BRAIN TISSUE NONLINEAR CONSTITUTIVE EQUATIONS

4.1. Introduction

Upon an impact load, brain tissue experiences diverse mechanical stresses. TBI may occur when induced stresses exceed the physiologic limits which currently are not fully understood. Thus, to predict injuries, accurate measurement of generated stresses in brain tissue would be very beneficial. It is known that the brain shows both elastic and viscous behavior (33). A great deal of effort has been devoted to describing brain tissue material properties using linear viscoelastic behavior assumptions (6,34). Quasilinear and nonlinear viscoelastic theories have also been developed for large deformations (14,35,36). The majority of these studies characterized the tissue in simple compression or tension experiments. In some of these studies, the brain was characterized by simultaneously measuring the elastic and viscous responses (17,37), while in some other studies, only the elastic characteristics were addressed to identify the tissue response (14,22,38). Pure elastic responses are obtainable only at extremely low and extremely high strain rates, which cannot be achieved using commercial testing machines for simple monotonic ramp experiments. The presence of viscosity, however, makes complete characterization of the brain material difficult.

The main aim of the current chapter was to estimate the instantaneous and long term elastic stresses in the brainstem. To this end, 6 sets of stress relaxation experiments were used at 6 different strain amplitudes in compression. Long-term responses of the tissue were measured directly from the experiments. Also initial instantaneous (short-term) stresses were defined as the highest induced stresses in the tissue by implementing a QLV constitutive model.

4.2. Quasi-linear Viscoelastic Model

In order to describe the response of soft biological tissues, such as the brain, in the nonlinear region, the QLV theory has been vastly employed. The QLV theory was first formulated by Guth et al. (39) for natural and synthetic rubbers and then introduced by Fung (40) for soft biological tissue. This theory has been used for explaining the behavior of ligaments and tendons (41,42). It has also been utilized to characterize the mechanical properties of brain tissue in nonlinear regions at different high strain rates (35,43). By implementing the QLV formulation, the nonlinearity, as well as the time and history dependency of the tissue can be well addressed. According to the QLV theory, the stress relaxation function of tissue is expressed as:

$$\sigma(t) = \int_{-\infty}^{t} G(t-\tau)\frac{\partial\sigma^{c}(\varepsilon)}{\partial\varepsilon}d\varepsilon(\tau) \tag{10}$$

Where $\sigma^{c}(\varepsilon)$ is the response of the substance to an instantaneous applied strain, ε. $G(t)$, representing the time-dependency of the material, is the reduced relaxation function which is normalized by the stress at $t = 0^{+}$ as follows:

$$G(t) = \frac{\sigma(t)}{\sigma(0^{+})} \text{ and } \quad G(0^{+}) = 1 \tag{11}$$

Equation (10) for the case of stress relaxation function of the tissue is simply expressed as:

$$\sigma(t) = G(t) \times \sigma^{c}(\varepsilon) \tag{12}$$

The instantaneous response of the tissue, $\sigma^{c}(\varepsilon)$, is assumed as an exponential function as:

$$\sigma^{c}(\varepsilon) = A(e^{B\varepsilon} - 1) \tag{13}$$

where A and B are tissue constants. This function considers the initial ramp step as a function of strain. For the relaxation function, $\mathrm{G(t)}$, the following expression is used:

$$G(t) = ae^{-bt} + ce^{-dt} + ge^{-ht} + k \tag{14}$$

In this equation *a*, *b*, *c*, *d*, *g*, *h*, and *k* are material constants that must be derived. The first three terms on the right hand side of the Equation (5) were used by Toms et al.(41). The problem with the first three terms is that when time goes to infinity, the long-term response of the model goes to zero, which does not accurately reflect the true behavior of the tissue in the long time. In the QLV modeling utilized in the research presented here, constant *k* was added to calculate the long-term behavior of the tissue. To address the instantaneous elastic behavior of the tissue more accurately, the QLV theory was implemented on stress relaxation experiments at strain levels from 5% to 30%, and parameters of the QLV equation were obtained.

4.3. Instantaneous and Long-term Stresses

Depending on the strain rate, the tissue may experience different stress levels at a specific applied strain that should be described in the model. It should be noted that both responses are elastic and bound the stress domain on the substance. Figure 15 shows a typical range of viscoelastic tissue responses under different loading conditions. Accurate determination of both elastic responses is essential because it directly relates to the determination of the constants of the springs and the dashpot.

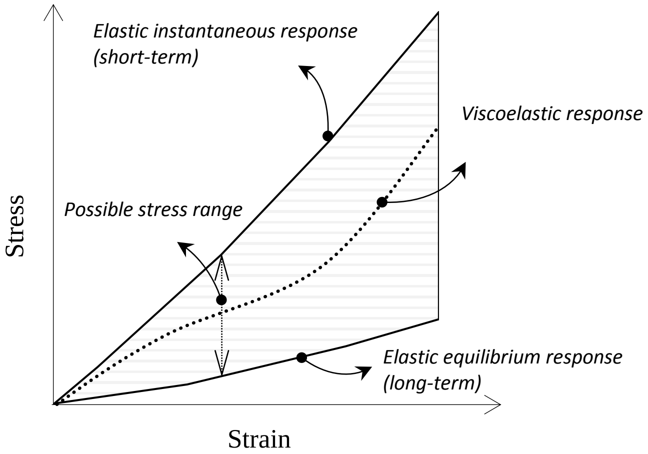

Figure 15. Possible range of stress-strain curve for viscoelastic brain material

The methods used in this study minimized the effect of viscosity to determine the two elastic responses that have not been previously addressed. The long-term responses of each stress relaxation test were directly recorded from the experiments. Thus the tissue stress values were estimated from 30 to 50 s after the measured force remained constant, times after which the estimated stress levels did not change significantly with time. This procedure was used for all initial strain values to find the lower bound response of the material. For instantaneous stresses, the QLV mathematical model was fitted to the results of stress relaxation experiments. Then the global optimization toolbox in Matlab (Version R20102a, MathWork, MA, USA) was used to find the optimal constants of the QLV model. The method provided the global minimum solution by starting from several initial values in the search domain. JMP software (Version 10.0.0, SAS Institute Inc., NC, USA) was used for statistical analyses and the significance level was set to 0.05. Table 3 indicates all the constants of the tissue in terms of the QLV explanation at different strain levels. A significant and negative association was noted between constant *B* and strain values (P=0.005). The association for constant A was insignificant (P=0.25). The association between constant *k* and strain values was significant (P=0.046). The remaining constants did not show any associations with strain.

Table 3. Results of QLV theory for brainstem tissue

QLV constants	**Nominal strain (%)**					
	5	**10**	**15**	**20**	**25**	**30**
A	421.148	317.926	294.548	169.177	510.577	773.359
B	14.636	14.791	11.507	12.475	9.047	7.383
a	0.485	0.224	0.543	0.576	0.662	0.102
b	11.484	3.438	11.438	10.154	16.179	0.093
c	0.172	0.483	0.182	0.150	0.138	0.633
d	0.509	31.957	1.201	1.160	1.120	18.660
g	0.208	0.156	0.140	0.139	0.098	0.160
h	0.024	0.258	0.118	0.180	0.100	1.445
k	0.135	0.137	0.136	0.135	0.102	0.105

Then, the instantaneous stress of the brainstem was calculated at each strain level from Eq. (3) when $t = 0^+$. As the strain increased, the instant response also increased as illustrated in Figure 16. Table 4 indicates the variation of the long-term and instantaneous stress responses of the tissue using the QLV theory.

Table 4. Short-term or instantaneous stress values of the tissue from QLV theory

Strain level (%)	**5**	**10**	**15**	**20**	**25**	**30**
Long-term Stress (Pa)	110	140	185	245	450	635
Short-term Stress (Pa)	454	1078	1361	1882	4391	6310

Figure 16 shows both instantaneous and equilibrium elastic behaviors of the tissue with strain.

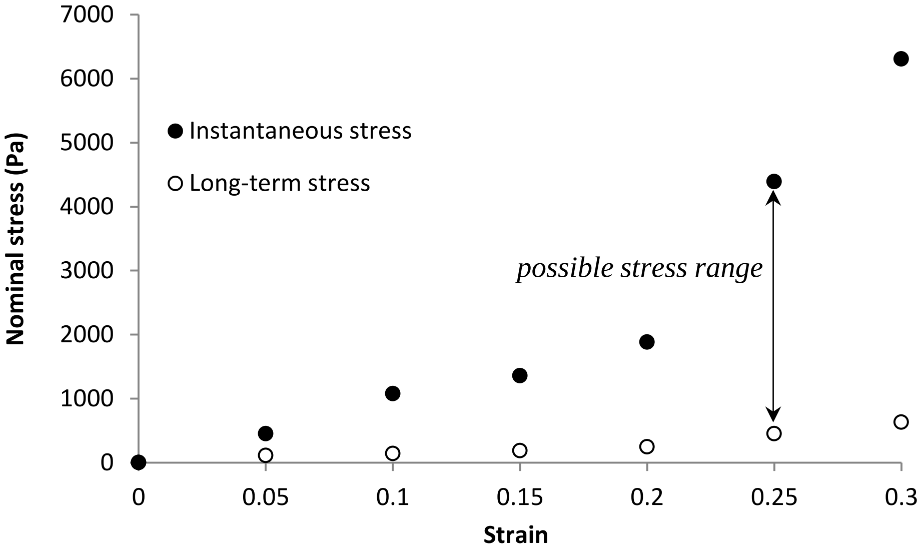

Figure 16. Instantaneous and long-term of the tissue over strain

The two elastic responses were addressed differently to propose brain tissue constitutive equations in prior studies (38). Mendis et al. (22) assumed a strain rate of 0.08/s as quasi-static and neglected the effect of viscosity. The respective strain rate in the study by Miller and Chinzei (14) was performed at a very small value of 0.64×10^{-5}/s. In addition, Miller and Chinzei (14) assumed that the strain rate of 0.64/s was high enough to ignore the effects of the time-dependent relaxation parameters in their proposed model. Pervin and Chen (44), however, were able to increase the strain rates on brain tissue up to 3000/s, using a modified split Hopkinson pressure bar. They observed an increase in stress values, showing the effect of viscosity even at such high strain rates. In fact, the presence of viscosity makes it difficult to identify the long term and instantaneous responses of the tissue at very low and very high strain rates by applying monotonic ramps. In contrast, in this study several individual stress relaxation experiments were conducted at different strain amplitudes on tissue samples to address both elastic responses. Our results showed that under initial strain levels of larger than 20%, the rate of change in both stresses increased. This may hint to the nature of tissue nonlinearity, which unfortunately cannot be well addressed with simple monotonic ramps on the tissue. The application of QLV gives a better estimation of the short term response as the highest possible stress experienced by the tissue.

Based on a linear regression analysis, a strong linear correlation was found between the two elastic responses ($P<0.001$). The relation was captured by the linear equation $y=ax-b$ where y and x are instantaneous and long-term stresses, respectively. The constants were estimated along with 95% confidence interval (CI) as follows: a = 11.0 (10.2, 11.9) and b = 666.36 (365.1, 967.6). Also both elastic stress values for bovine brain tissue were derived from the data published in the study figure of Laksari et al. (2012) and a similar regression analysis was performed. Similar to the porcine brainstem tissue, the resulting relation between the two elastic responses was linear with instantaneous stresses. The corresponding constants were however different at a = 6.4 and b = 274.27. Figure 17 compares the results of linear regression analyses for the current study and the study by Laksari et al. (2012).

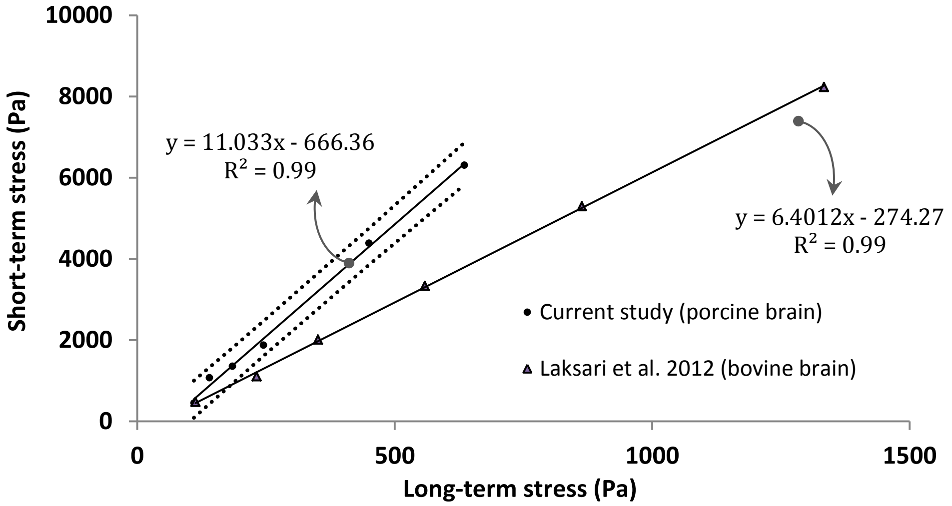

Figure 17. Correlation between short-term and long-term stresses of the brainstem, starting at 5% strain level for each graph and show the CI for our porcine brainstem; similar regression lines for bovine data derived from previous studies are also presented

It is known that instantaneous stress cannot be directly obtained from experiments, due to technical issues such as overshoot, vibrations, and testing machine limitations (42). However, a strong correlation between the instantaneous and long term responses (R^2=0.99) suggested that the instantaneous response could be estimated from the long term response of the tissue. This result is noteworthy because the long-term response can be easily measured directly from experiments. Independent of initial strain amplitude, the strong relation between the two behaviors also showed that the actual stress varied about 11 fold. From literature, a similar strong linear correlation was found between the two elastic responses for the bovine brain tissue (16). This similarity in the linear relations between the two elastic responses for both porcine and bovine suggests that a linear correlation might also hold between the two elastic responses for other types of brain tissues, including possibly human brain tissue. However, the slope for the regression line of the bovine brain tissue was found to be smaller than that of the porcine brain tissue, which underscores the need to perform experiments with each particular brain tissue. This difference in slopes may explain the difference in the stiffness of the two different brain tissue materials.

4.4. Relaxation Modulus of the Tissue

The reduced relaxation moduli of the brainstem were measured at different strains. Figure 18 shows the results for the initial second of the test time interval, during which the responses varied considerably. As illustrated, the relaxation modulus varied from one strain level to another. However, the moduli derived at 25% and 30% strain values were very similar. The moduli at 15% and 20% were also similar to one another, but dissimilar from the results obtained at the other strain levels.

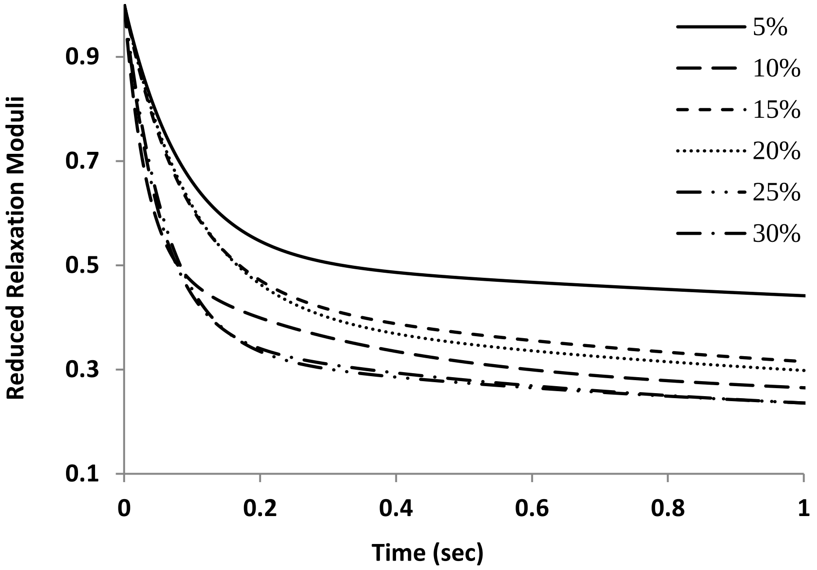

Figure 18. Reduced relaxation moduli at different strain levels for porcine brainstem

Surprisingly, while the moduli should be independent of strain values, our experiments showed that they varied considerably with strain. This strain dependency of the relaxation modulus may be due to model truncation, as the viscous part of the tissue is considered linear. In reality, the viscous part of the tissue might be nonlinear (15), thus the application of the QLV theory may not be capable to represent the complexity of tissue behavior in the nonlinear viscoelastic regions. This finding suggests that the characterization of brain tissue using the QLV theory at only one strain amplitude may not be applicable for the whole range of tissue deformations, and multiple strain amplitude experiments must be performed to calculate a reasonable set of constants.

4.5. Hyperelastic Model for Elastic Responses

Hyperelastic models have been employed for soft biological tissues in several studies (15,17,22,38). The developed models were based on SEDF which can be expressed in terms of the invariants (I_i) of the left Cauchy Green strain tensor (Finger tensor), $\mathbf{B} = \mathbf{F} \cdot \mathbf{F}^T$, where **F** is the deformation tensor. In the research presented here, the brain tissue material was considered as incompressible homogeneous isotropic material. For an incompressible material, the SDEF can then be written in the following form:

$$W = \sum_{p,q=0}^{n} C_{pq}(I_1 - 3)^p (I_2 - 3)^q \tag{15}$$

$$I_1 = \text{Trace}\,[\mathbf{B}], \quad I_2 = \frac{I_1 - \text{Trace}[\mathbf{B^2}]}{2}$$

The stress function can be obtained by taking the derivative of SEDF with respect to the extension ratio as follows:

$$\mathbf{S} = \frac{\partial W}{\partial \lambda}, \qquad \boldsymbol{\sigma} = \frac{1}{J}\mathbf{F} \cdot \mathbf{S} \cdot \mathbf{F}^T, \qquad J = \det(\mathbf{F}) \tag{16}$$

where **S** and **σ** are 2nd Piola-Kirchhoff and Cauchy stress, respectively. Employing the Cayley-Hamilton theorem, the stress function can be expressed in terms of invariants as follows:

$$\boldsymbol{\sigma} = 2\frac{\partial W}{\partial I_1}\mathbf{B} - 2\frac{\partial W}{\partial I_2}\mathbf{B}^{-1} \tag{17}$$

In terms of the Finger tensor, the Mooney-Rivlin model is expressed as follows:

$$\boldsymbol{\sigma} = C_{01}\mathbf{B} - C_{10}\mathbf{B}^{-1} - p\mathbf{I} \tag{18}$$

where $\mathbf{I}$ is the unit matrix and p is a hydrostatic pressure which is added to satisfy the boundary conditions. C_{01} and C_{10} are constants of the material that should be measured.

Then Mooney-Rivlin model was employed to describe the stress functions in the equilibrium and instantaneous states. The hyperelastic constants were found to be C_{01}=16222 and C_{10}=-16947 for instantaneous response, and C_{01}=1084.5 and C_{10}=-995.5 for long-term response. Then from the generalized form of Equation (15), we kept constants C_{01}, C_{10}, and C_{11}, which is the Mooney-Rivlin equation with addition of the constant C_{11}. The hyperelastic constants resulted in C_{01}=-30173.54, C_{10}=27040.41, and C_{11}=-22795 *Pa* for the instantaneous; and C_{01}=-4361.16, C_{10}=3837.78, and C_{11}=-2557.45 *Pa* for the long-term stress function of the material. Figure 19a and 19b show how short-term and long-term stresses were fitted to the hyperelastic model. Strong correlation of 99% was found between the generalized hyperelastic models and the results of the study presented here (P<0.0001). The possible stress on the tissues ranged between these two elastic stress functions as demonstrated in Figure 19c. This figure illustrates an important characteristic of the tissue in which the two binding curves are elastic with no evidence of influence from the dashpot. More importantly, the response of the tissue, under every circumstance, remained bound between the curves, regardless of the strain rate.

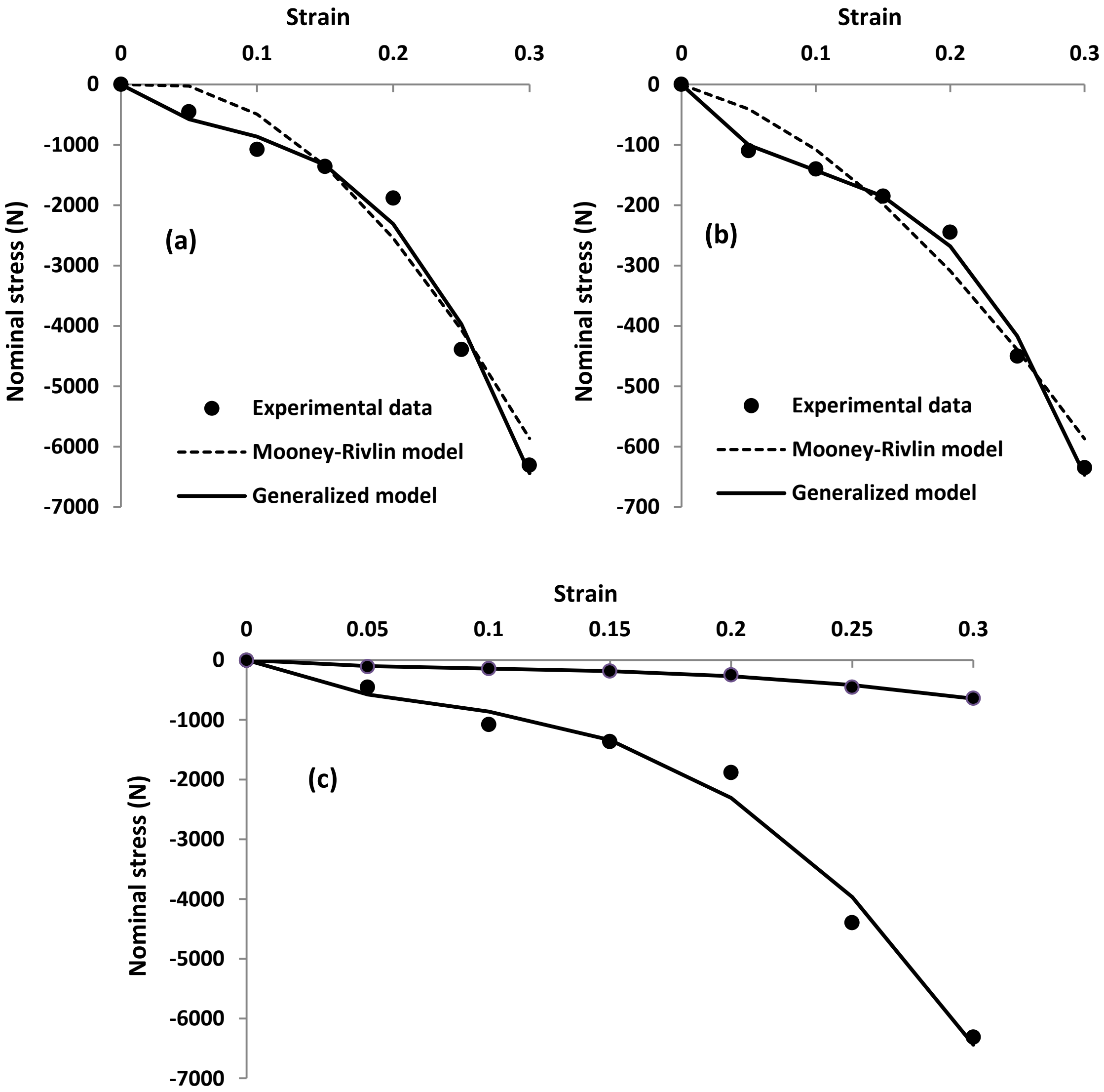

Figure 19. The Mooney-Rivlin and generalized models explaining the (a) instantaneous and (b) equilibrium stress states; (c) both responses, including experimental data and generalized model, limit the possible range of stress that the brainstem may experience at a specific stain value

4.6. Conclusion

In this chapter, the QLV was employed independently at each strain value to estimate the corresponding instantaneous stress value, and the long-term stress values were measured from the experimental data. The two elastic responses can potentially be employed for high velocity impacts such as blast loading scenarios, under which the tissue behaves close to its instantaneous response. A strong linear correlation was found between the short-term and long-term behaviors of porcine brainstem tissue. The linear trend was found on bovine brain tissue from previous studies. The short-term stress for our porcine brainstem was found to be 11 times larger than the long-term stress, similar for all initial strain levels. The reduced relaxation modulus was found to vary with strain, suggesting multiple strain experiments are needed to better investigate the range of applicability of the QLV theory. Also a generalized hyperelastic model was found to explain well both the short-term and long-term responses of porcine brainstem tissue in compression.

CHAPTER 5. TRAUMATIC BRAIN INJURY UNDER BLAST

5.1. Introduction

Annually, TBI is responsible for 50,000 deaths and 235,000 hospitalizations nationwide (4). From a biomechanical point of view, an assault to the head creates mechanical forces and motions (translation and rotation), and results in an elevation of ICP (45). An increase in the relative displacement and shear stress/strain on the brain tissue also damages the structure of the brain, including the axons and extracellular matrix (26,46). Acceleration and deceleration of brain tissue may lead to skull/brain contact resulting in contusion, observed in different parts of brain tissue. Relative motions between the skull and brain may cause several types of injuries such as intracerebral hematomas and cerebral contusions (26). Brain injury results when the injury related biomechanical parameters increase beyond the tolerated normal values. Threshold values have been defined for each of these biomechanical parameters for TeBI (47,48). To discuss the severity of an injury, one can compare these threshold values to the values obtained from a biomechanical head, brain, and tissue response analysis.

Blast is a predominant cause of TBI. This is a major threat to soldiers in battlefronts. Explosions generate powerful travelling shock waves that interact with the human head, resulting in severe damage to brain tissue or death., Zuckerman (49) classified brain injuries due to blasts into primary, secondary, or tertiary injuries, based on physical outcomes to the body. A primary blast injury (PBI) occurs when there is direct exposure of the human body to blast waves. PBI is frequently undiagnosed and underestimated, because it can cause severe internal damage without any external signs. A secondary blast injury (SBI) also results from a blast and is defined as trauma caused by objects propelled by a blast that impacts the body. With tertiary blast injury (TeBI) explosions create blast winds that propel the body to hit enclosing walls, or other obstructing objects. Kluger et al. (50) discussed what they called quaternary brain injury, in which blast causes thermal burning effects. They also introduced the quinary blast injury, which is produced by delayed effects from blast exposure such as toxic effects by chemicals.

The space in which an explosion occurs plays a major role in the severity of human injuries. In an open space, the blast creates a sudden increase in air pressure at the front of the shock wave. This is due to the expansion of the blast waves that is followed by a rapid decreasing pressure during the positive phase, as well as part of the sub-atmospheric phase, which is called the rarefaction phase (51). There are several studies on the blast-head interaction in open spaces having been conducted on PBIs; Moss et al. (52) studied the interaction of a blast wave and the human head. They showed that direct action of a blast wave on a human head model leads to skull flexure that causes brain injury even at the low pressure of 1 bar. Chafi et al. (53) theoretically determined the response of the human brain under a blast using a finite element approach. They estimated the variation of ICPs in coup and contrecoup sites, and measured the maximum principal strain and maximum shear stress in different areas of the brain. Taylor and Ford (28) evaluated brain injuries when the head was exposed to a blast overpressure of 1.3 MPa. They also measured the ICP, the volumetric tension, and the deviatoric shear stress of the brain. They proposed that the stress generated in local areas may cause different axonal injuries. In another study, Ganpule et al. (54) studied the interaction of a surrogate human head and blast wave in a shock tube both experimentally and computationally.

They showed that the skull deforms in a complex way, oscillating around the brain. They also showed that the deformation of brain tissue is governed by the pressure wave.

In a confined space, however, the blast wave reflecting off walls contributes to creating additional irregular and complex shockwaves. In most cases with a longer duration, the shockwaves are capable of transferring higher amounts of energy to the human body (3,55). It has been proven that for shorter durations, a larger amount of overpressure can be tolerated, but a longer duration of loading makes the injury situation more severe and harmful (56). This is the reason that the severity of injuries and the rate of mortality are lower in open spaces than in confined spaces (3,55). The pressure increase is higher at the corners and near the walls due to reflections. The literature of blast-head interaction in confined spaces is not mature. There are only a few studies related to the effect of confinement. In this regard, Zhang and Sharma (57) examined the exposure of a three-dimensional (3-D) idealized human head to a blast of trinitrotoluene (TNT). Different scenarios of blasts were considered to examine the effects of the reflections; in open space, on the ground, and with the head placed near a concrete wall. They showed that the effect of reflecting walls is considerable only on the region of the brain closest to the wall. More recently, Sevagan et al. (58) computationally studied the effect of several parameters in an infantry vehicle such as boundary conditions, impact velocity, and seat arrangement by employing a dummy/vehicle model. They concluded that the effect of blast impact is more pronounced than blunt impact. In general, most of the studies on blast-related injuries are only focused on the interaction of the head with the incident shock wave. In such studies, the reaction of the brain is measured for a short period of time (less than 10 milliseconds) after the blast. Usually, movement of the head and the consequences of the reflected waves from the enclosing walls are neglected. No computational study has been reported on tertiary injury, particularly as a consequence of exposure to a blast. When complex wave environments (confined space) are analyzed, several complicated and nonlinear phenomena interact that must be simulated concurrently.

From chapter 5 to 8 of the thesis, the computational investigations focus on blast induced TBI, mainly in confined spaces. The studies presented here have been published previously (59-61), investigating the biomechanical responses of the brain of a head model during exposure to the shock front of a blast wave (which might cause PBI). The effects of reflections off the walls of confinement are assessed while the head is located in the vicinity of the wall. To this end, confined, semi-confined, and open spaces are modeled and compared. Additionally, the study addresses a blunt impact of the human head as a result of translation from the blast wind (which might cause TeBI) in both open space and a complex wave environment. Then the results of PBI and TeBI are compared. Different injury related biomechanical parameters are computationally estimated and compared. The study provides insight into the severity and modes of injuries in confined space explosions. In the case of TeBI investigations, the data are collected for about 40 milliseconds, until the head motion stabilizes.

5.2. Materials and Methods

5.2.1. The Finite Element Head Model

The size and geometry of the 50th percentile deformable human head model used in the research presented here was derived from a 3-D head structure using a Magnetic

Resonance Tomography (MRT) method adapted from Horgan and Gilchrist (27). This head model included different head layers as shown in Figure 20.

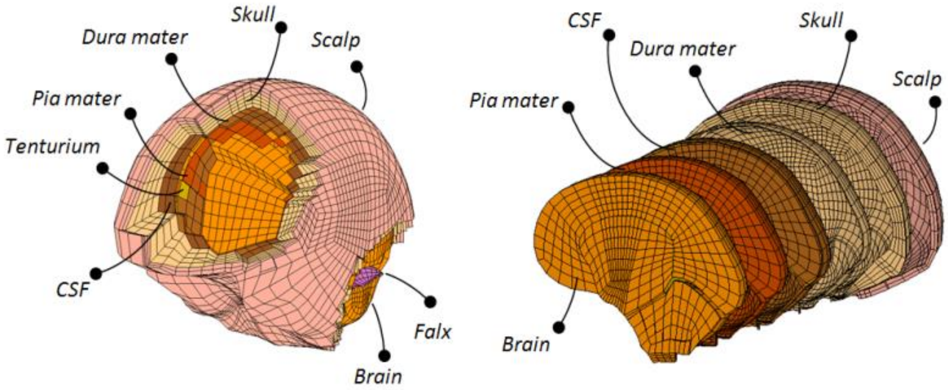

Figure 20. Finite element human head model and its essential components (59)

The skull was modeled with an open foramen magnum to show a more realistic ICP variation (62). The scalp, skull, dura, pia, falx, and tentorium were assumed to have a linear elastic response (63-65). The mathematical model that explained the response of CSF was based on the Hugoniot pressure $\dot{p} = K\dot{\varepsilon}$, where $\dot{p}$ is the pressure rate and K is the bulk modulus (66). Also $\dot{\varepsilon}$ denotes the volumetric strain rate. Constitutive relations for the brain material were assumed in a wide range, from linear elastic to nonlinear hyper-viscoelastic (11,22,67). In simulations of the current research, the brain was assumed to have viscoelastic properties and its material constants were derived from Ruan et al. (63) who used human data from the research of Galford and McElhaney (11).

Table 5 shows the material properties and the element types of the head components. The membranes were modeled as four-node shell elements. The brain, CSF, skull, and scalp, however, were modeled using eight-node constant stress formulation solid elements.

Table 5. Material properties of human head components and their element types

Tissue	Constitutive model	Element types and thickness	Mechanical Properties		
			Density (Kg/mm^3)	Elastic Modulus (MPa)	Poisson’s ratio
Scalp	Linear elastic	Solid, 6mm	1.2×10^{-6}	16.7	0.42
Skull	Linear elastic	Solid, variable	1.8×10^{-6}	15,000	0.21
Dura, falx, tentorium	Linear elastic	Shell, 1mm	1.13×10^{-6}	31.5	0.45
Pia mater	Linear elastic	Shell, 1mm	1.13×10^{-6}	11.5	0.45
CSF	Fluid-Type elastic	Solid, 1.3mm	1.04×10^{-6}	Incompressible K=2,190	-
Brain					
Viscoelastic	Density (Kg/mm^3)	Bulk Modulus (MPa)	Short-term Modulus (kPa)	Long-term Modulus (kPa)	Decay Factor (ms^{-1})
Solid element	1.04×10^{-6}	128	528	168	35

In order to properly and accurately model the interactions of the various parts when the head experienced different types of loading conditions, appropriate contact conditions were defined between each element of the head and brain. Contacts between the membranes and the brain were considered as tied node-to-surface. The remaining contacts were considered tied surface-to-surface type (53).

In all computational studies, the head was assumed to be free-floating, assuming that for the first few milliseconds, the neck and body have little influence on the head response under the sudden applied load on the head. This assumption has been shown to be logical in previous studies (68). In addition, the effects of the trunk on the head due to the relative velocity were assumed to be negligible because the blast wind is applied not only to the head but also to the trunk. While the projection areas and the densities of the head and the rest of the body are different, the head and the body move with nearly identical velocity for the duration of several milliseconds. This fact has been demonstrated in research work by Fletcher and Bowen (69), studying the translational effect of the blast wind. In our computational modeling, the effect of gravitational force was ignored.

5.2.2. *Blast Wave Propagation*

Detonation is the result of a sudden release of energy that produces a sudden rise in pressure, heat, sound, and light. The rapid exothermic oxidation of the substance into the form of gas creates the blast. To determine the behavior of the explosive gas, its equation of state (EOS) must be defined based on its state variables. This EOS explains pressure-volume-energy relationships of the gaseous form of detonation. Jones-Wilkins-Lee (JWL) is the most well-known EOS which has been verified by hydrodynamic experiments (70). JWL EOS is expressed as:

$$p = A\left(1-\frac{\omega}{R_1 V}\right)e^{R_1 V} + B\left(1-\frac{\omega}{R_2 V}\right)e^{R_2 V} + \frac{\omega E}{V} \tag{19}$$

where ω, A, B, R_1 and R_2 are the constant parameters that are defined by the user; V is the relative volume; and E is the internal energy per initial volume. All are derived from the explosive handbook by Dobratz and Crawford (71). The JWL equation is simple, fairly accurate, and widely used in detonation analysis. Most importantly, it is possible to employ a gradual increase in size of the medium elements to decrease the computational cost (72), but it is essential to have a fine and uniform FE mesh for detonation to gain rational results (70,72). In this thesis, air is assumed to be an ideal gas. The linear polynomial EOS for air can be simply written as: $p=(\gamma-1)\frac{\rho}{\rho_0}E$ with γ=1.4, E=0.25 MPa, and ρ_0 = 1.29×10^{-3} g/cm^3. In this chapter, p is air pressure, E internal energy per initial volume, ρ_0 initial density, and ρ air density. Also, γ is the polytropic ratio of specific heats. The cut-off pressure is set to zero to stop the creation of negative pressure.

The detonation and air domain were created in Altair Hyper Work 11.0 (Altair Engineering, Troy, Michigan). As the processor and postprocessor, LS-Dyna software 971 (Livermore Software Technology Corp., Livermore, California) was employed for the simulations in this research. Also the penalty method was implemented to simulate fluid structure interactions. Shear stresses, pressures, and strains at different areas of the brain were monitored and determined in all scenarios.

In order to model the blast propagation in FE analysis, the ALE formulation, which is a combination of the Lagrangian and Eulerian approach, is used, benefiting the advantages and minimizing the disadvantages of the two methods (73). ALE maintains the element shape inside the domain and allows the use of a purely Lagrangian description at the boundaries. The ALE approach is explained by the fundamental principles in physics explaining the behavior of any continuous medium; conservation of mass, momentum, and energy. The ALE form of the Navier-Stokes equations including conservation of mass and balance of momentum equations is explained by the following equations (74):

$$\frac{\partial\rho}{\partial t}=-\rho\frac{\partial v_i}{\partial x_i}-w_i\frac{\partial\rho}{\partial x_i} \tag{20}$$

$$\frac{\partial v_i}{\partial t} = -(\sigma_{ij,j} + \rho b_i) - \rho w_i \frac{\partial v_i}{\partial x_j} \tag{21}$$

where σ_{ij} is the Cauchy stress tensor and b_i is the external body force per unit mass. The velocity of the material is denoted by v_i, the velocity of the mesh by u_i, and the relative velocity $w_i = v_i - u_i$. The Cauchy stress tensor is explained as:

$$\sigma_{ij} = -p\delta_{ij} + \mu(v_{i,j} + v_{j,i}) \tag{22}$$

where p is the pressure, μ is the dynamic viscosity, and δ_{ij} is Kronecker's delta.

The balance of energy:

$$\rho \frac{\partial E}{\partial t} = \sigma_{ij} v_{i,j} + \rho b_i v_j - \rho w_j \frac{\partial E}{\partial x_j} \tag{23}$$

where E is the specific total energy per unit volume. The multi-material ALE formulation allows the FE mesh to move independently of the material flow. Upon impact of the head with blast waves, the transferred load to the head can be calculated through a penalty-based FSI technique. In this method, a coupling resistance force is calculated based on the penetration depth (70).

5.3. Validations of the Computational Results

5.3.1. Blast Simulation

Validation of blast-head simulation interaction remains a challenge. In the literature, several cadaver tests have been used to validate computational modeling of blunt impact. In recent studies, shock tube tests have been employed in blast scenarios, to examine the interaction of surrogate head models with the blast waves (54,74). In most of these experiments, only the kinematical responses of the dummy heads were measured and used for the validation of computational simulations. Robert et al. (74) developed a human head model and a physical human head surrogate with the identical dimensions of their head model. For brain tissue matter, they employed Sylgard gel 527. They measured and compared the pressure inside the brain for the head model and for the surrogate. This work is regarded as a big step. However, in reality, the finite element models of real human heads used in computational studies are far different from the surrogates, because the surrogates do not include the complications of the human head. This question still remains for full validation of any head model in use. Perhaps parametric studies by such models can provide a base for analysis and at some stage can become a platform for validation.

The accuracy of simulating blast wave propagation in a closed field and the wave reflections from wall(s) were validated against experimentally measured pressure published by Edri et al. (1). Several experimental blast scenarios in the published study were reproduced in a semi-confined space with an opening on the top. The reflected pressure values were measured at specific locations inside the space (Figure 21). In the computational study, 1.5 kg TNT was used for explosion. In multiple experiments, the pressures at the equivalent coordinates were monitored. Due to symmetry of the space, one fourth of the environment was used for the modeling purposes, which considerably reduced computational cost and running time of the study. Also, to ensure accuracy, several mesh sizes were considered for the air domain, as well as for the TNT material, leading to an optimum mesh size for the analyses.

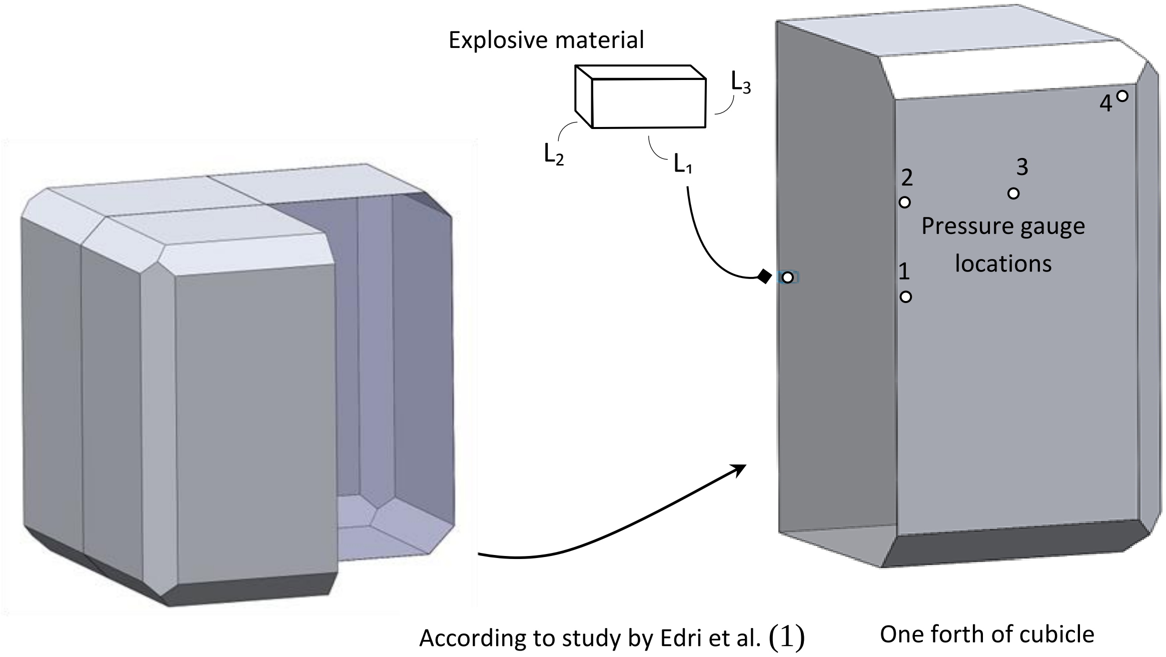

Figure 21. 3-D view of one quarter of the cubicle, the instrumented wall, gauge locations and HE detonation position (L_1=156×L_2=134× L_3=52 mm^3) (59)

Close agreement can be seen by comparing the pressure values produced in the computational analyses against the experimental data (Table 6).

Table 6. Comparison of the reflected pressure from the explosion; experimental data from the study of Edri et al. (1) vs. the numerical simulation

Gauge No.	Pressure (kPa)		Error%
	Experimental	**FE Simulation**	
1	2125.2	2412	13.5
2	1117.0	1037	7.1
3	990.47	877	11.45
4	1469.8	1370	6.8

5.3.2. Head Impact Simulation

The human head model in the thesis presented here has been validated under impact load several times. Originally, Horgan and Gilchrist (27) verified it against different commonly referenced cadaveric experiments (67,75,76). This head model has also been previously employed under different blast scenarios as well as blunt impact with acceptable results (29,53,77,78).

The computational modeling was validated against experiment No. 37 of Nahum et al. (67) to assure the appropriate implementation of parameters such as boundary conditions and material properties. The Nahum et al. (67) experiment has been used as a de facto standard to validate several computational research projects in the biomechanics of head impact. In experiment No. 37, a cylindrical mass with a weight of 5.59 kg and a speed of 9.94 m/s impacts the head which is inclined 45 degrees from the brain Frankfort plane. To simulate the impact situation, a semi-sinusoidal input force with amplitude of 7900 N was applied to the head in the research presented here. Figure 22 compares the ICP in the coup and contrecoup sites of the brain for the simulation to the corresponding measurements in the cadaver test. As depicted, the simulation accurately predicted the response of the brain. The close agreement of the results met the requirements for the simulation.

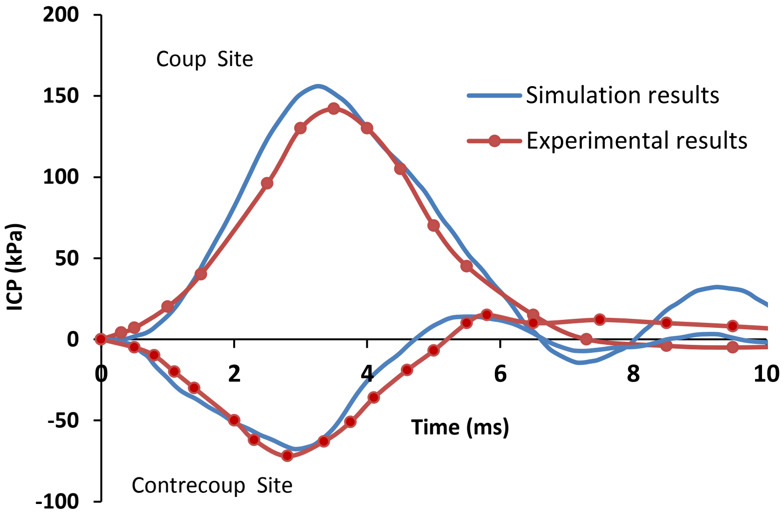

Figure 22. Validation of computational studies with the impact on the forehead of a human cadaver, performed by Nahum et al. (67) in which the brain ICP variations were compared (61)

CHAPTER 6. EFFECTS OF REFLECTIONS FROM WALLS ON THE HEAD

6.1. The Confined Space and the Head Stand-off Positions

Two cubic confined spaces were considered to simulate the effect of walls on the brain biomechanical parameters; the sides of the small space measured 1000 mm, and the sides of the large space were1450 mm. The mesh size varied from about 4 mm to 23 mm from the detonation location to the farthest location of the space, respectively. For a fair comparison, the size of the mesh in both spaces kept essentially the same. The mesh size and its variation are shown in Figure 23.

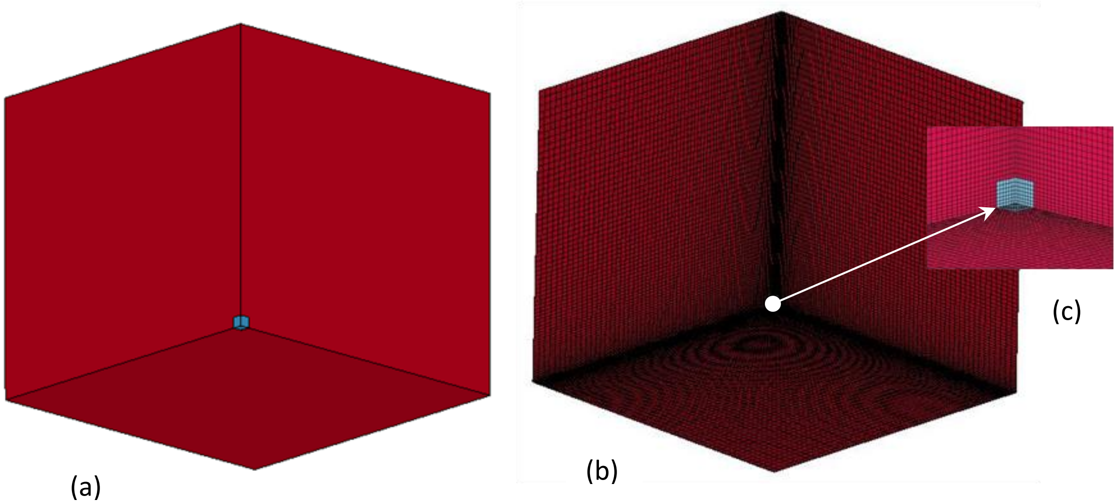

Figure 23. The confined space (a), the FEM discretized space (b), and the explosive material used in the simulation (c); while the detonation mesh is fine and uniform, the space (air) has undergone a variation of size when it has been away from the detonation (59)

In these experiments, the head model was placed at 3 stand-off positions away from the HE charge. The positions were devised to be either close to or away from walls of confinement (Figure 24). A total of 6 positions were assumed. The first three positions were in the large closed space indicated by A, B, and C. The heads were exposed to the incident shockwaves, since these positions were away from the neighboring wall. The remaining three positions were in the small closed space indicated by D, E and F, where the walls were close to the head models. Therefore, these heads experienced the incident shockwaves as well as the reflections off the neighboring wall(s). To be fairly compared with each other, paired positions A and D, B and E, as well as C and F were located at the same coordinates with the same orientation and distance of the head model with respect to the detonation. For the case studies presented in this chapter, the head was lifted up 300 mm from the ground level. A cubic 57gr TNT was located in the top left corner of the two spaces.

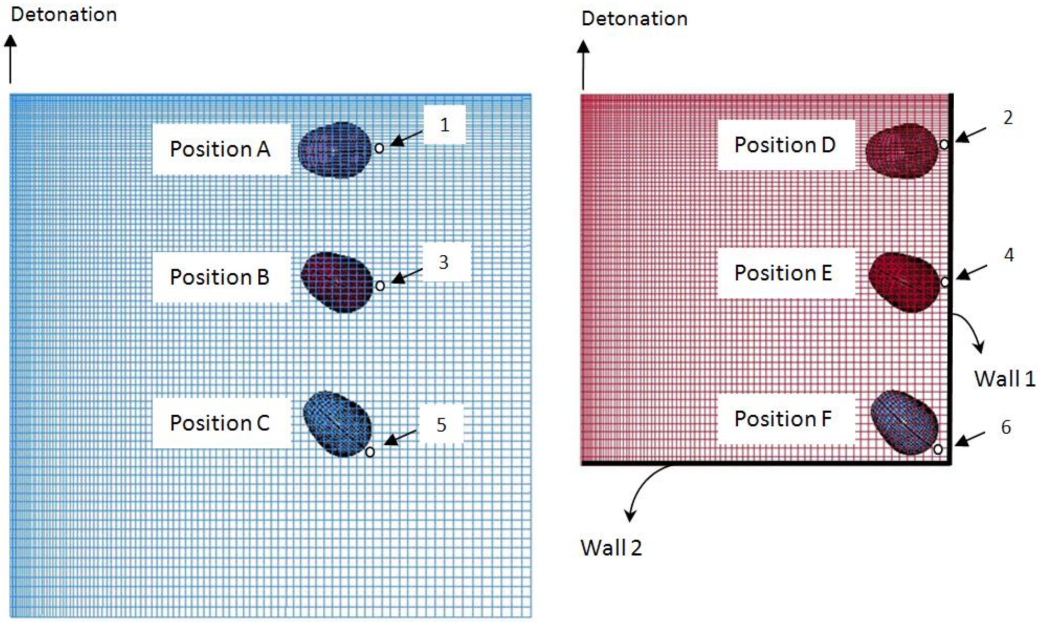

Figure 24. Positions and orientation of the human head model in the two environments (top view): Paired Positions A and D have the orientation of 0° and standoff of 860mm; Paired Positions B and E have the orientation of 30° and standoff of 1000mm; Paired Positions C and F have the orientation of 45° and standoff of 1200mm (59)

The data were collected from small regions of the brain and the skull. Then the averaged values of the biomechanical parameters of interest were calculated and compared for each paired position (for instance paired B and E) (59).

6.2. The Computational Results

6.2.1. Pressure Wave Magnification due to Reflections from the Walls

To estimate the variation of blast wave propagation inside the two spaces, the head models were first absent from the spaces, and the blast scenarios were simulated. Then, the pressure at points of interest (points 1, 3, and 5 near the walls, and points 2, 4, and 6 far from the walls) were measured. The pressure waveforms at points in the small and large spaces with the same standoff positions were compared. The results of the comparison are illustrated in Figure 25, where large differences in pressure magnitude can be observed in the pressure amplitudes at the same standoff distance points.

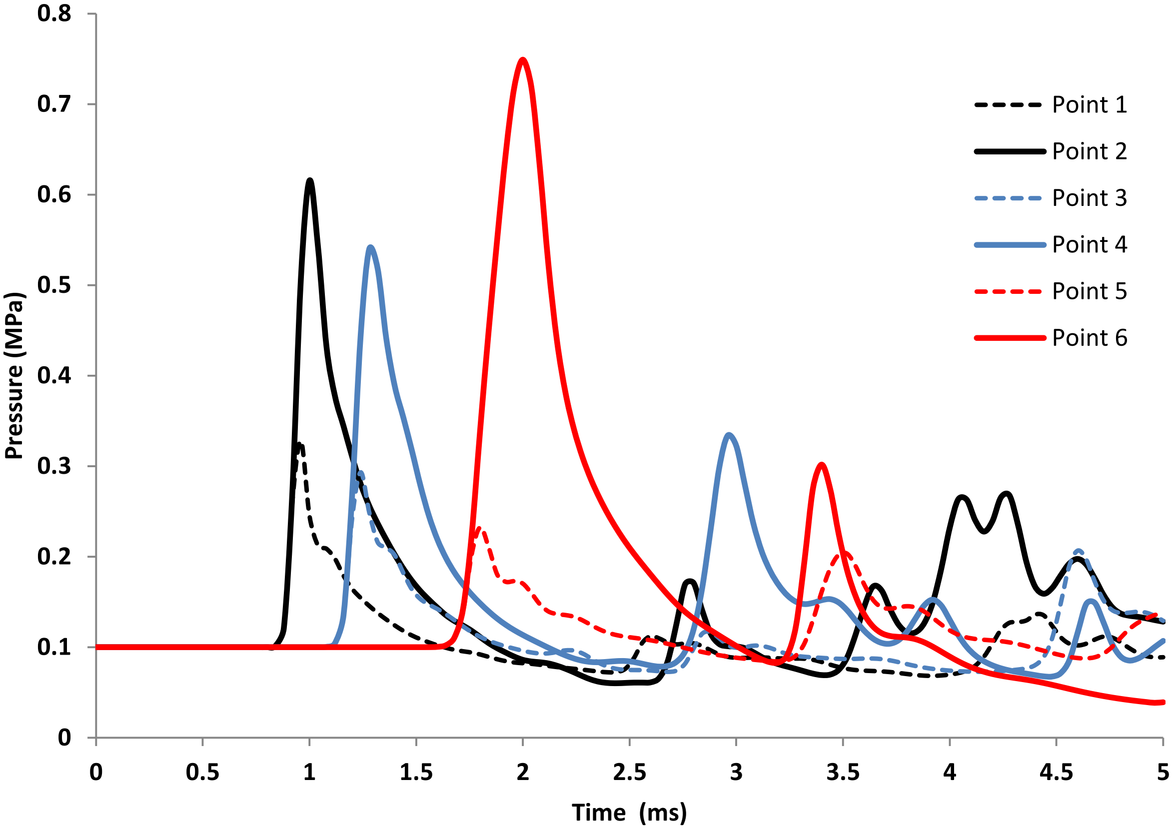

Figure 25. Blast wave overpressure at the coordinates where the heads would later be tested (59)

The increased pressure difference for points 2, 4, and 6 resulted from the shock wave reflections created by the presence of neighboring wall(s). The differences between pressure values at point 1 and 2, as well as points 3 and 4 both showed about 2-fold increase when measured near the wall. The difference increased up to four times, when point 6 was compared with point 5. Here the cumulative reflected pressures from the two neighboring corner walls caused this increase.

6.2.2. The Reflected Shockwaves from Initiation to Reflection

The shockwave propagations in the small environment are shown in Figure 26. In this test, the human head model was located in the corner most distant from the detonation. A notable reflection was not realized from the walls or the ground which were immediately adjacent to the detonation (Figure 26b, Figure 26c, and Figure 26d). Figure 26f illustrates that reflections were initiated at the instant shockwaves hit the walls to either side of the head. Figure 26g through Figure 26k illustrate the reflections that propagated throughout the space. Figure 26i shows the time that reflections of the two walls hit the head. Reflections were continually generated until they hit the human head model in the corner. Due to symmetry in this domain, the reflections from the two walls hit the head simultaneously. This can be the worst scenario.

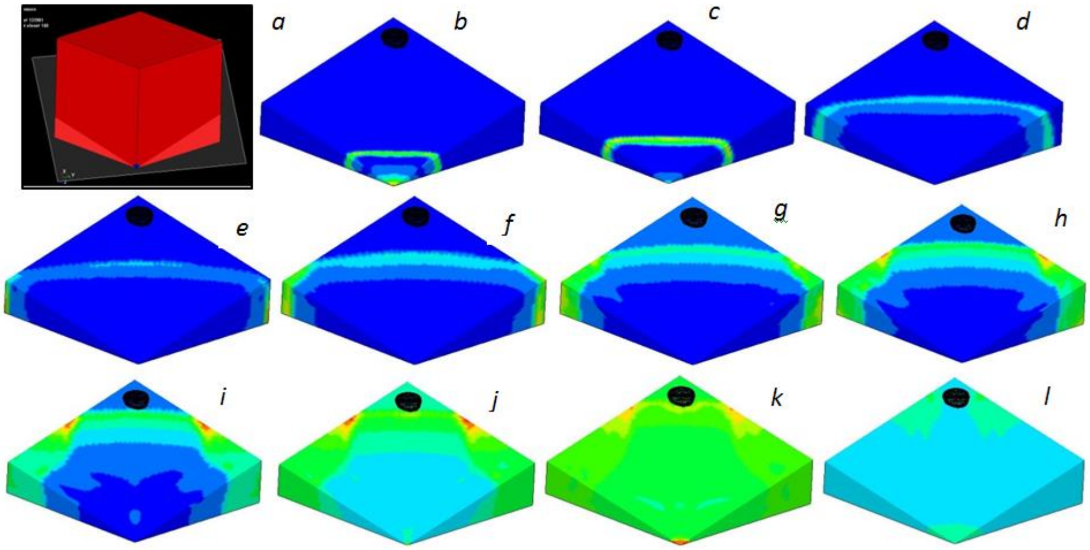

Figure 26. Blast overpressure wave propagation with the human head model placed in the corner at position F; the medium is cut for better observation of wave propagation around the head (59)

6.2.3. Human Head Model Responses

For all 6 given blast scenarios, several injury-related biomechanical parameters were collected and compared, including pressure on the human skull, ICPs, brain rigid body accelerations, brain strains and stresses, and brain maximum shear stresses.

6.2.3.1. The skull pressure

The post-blast pressure on the skull of each of the six head models is shown in Figure 27. While pressures at points 1 and 2 (without head models in the spaces) showed a significant difference (Figure 25), pressures on the skull of the head models at positions A and D were not found to different to a similar degree.

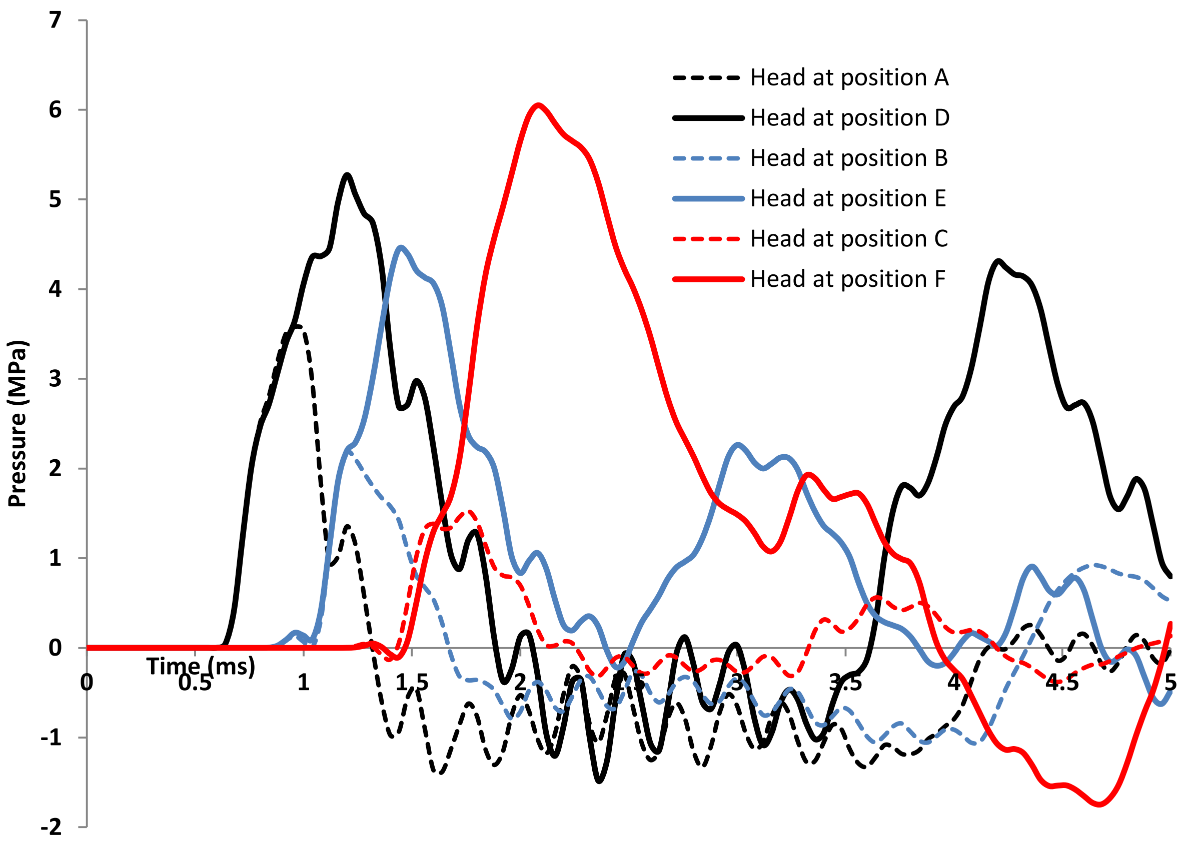

Figure 27. Pressure applied on the skull at all positions; pressures at A, B and C are shown with dashed lines; pressures at D, E and F are shown with solid lines (59)

The pressure on the skull at position D increased about 50% compared with that at position A. The pressure on the skull at position E was notably higher than that at position B (Figure 27). The difference between skull pressure at positions C and F were even higher (about 4 times) than the ones at the other paired positions. It was caused by the reflections from the two walls hitting the head model.

6.2.3.2. Variations of ICP

In all scenarios, the pressure on brain tissue was considerably less than that on the skull, due to the presence of CSF. The pressure values were collected from the areas showing maximum ICP variations. Compared with position A, the increase of nearly 25% in ICP was recorded on the brain at position D (see Figure 28). The increase at position E was even higher. In the corner at position F, the ICP was considerably increased compared with its counterpart position at C.

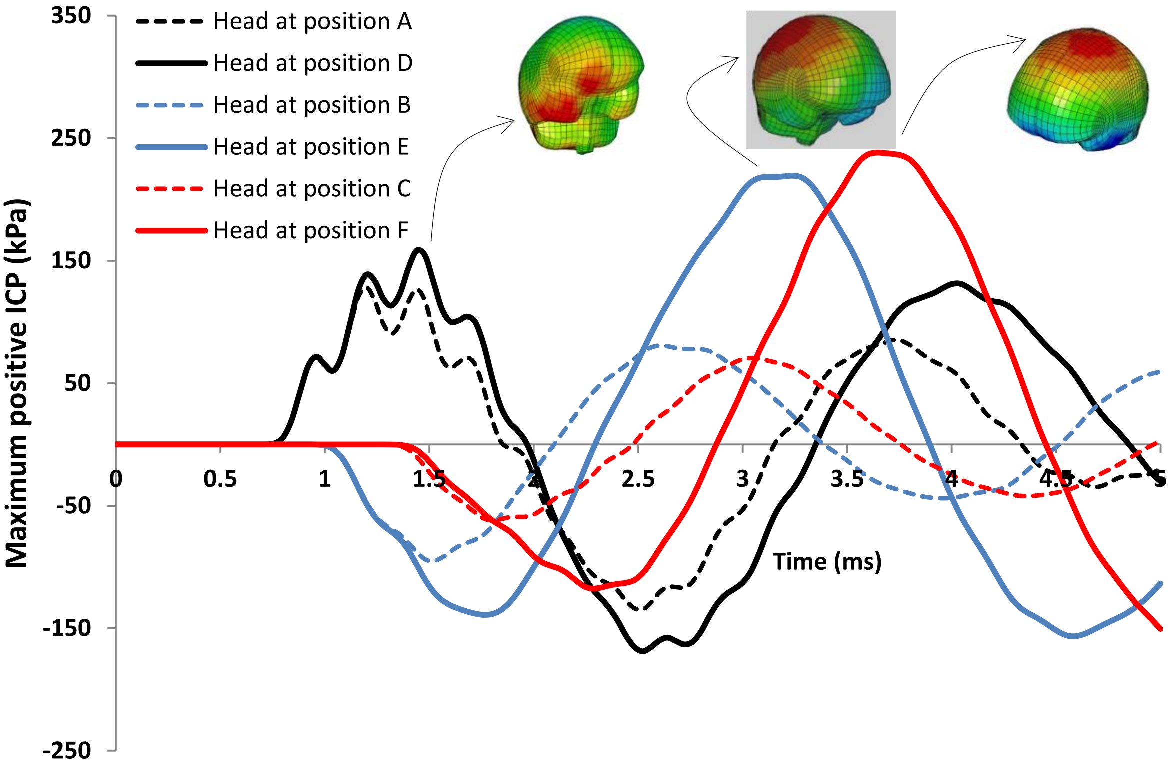

Figure 28. ICP variations in coup site for the given locations (59)

The pattern of the ICP change was similar in the contrecoup site (Figure 29). The negative pressure on the head at position D was about 55% higher than that at position A. The difference between maximum pressures at positions E and B was even greater (about 100 kPa at position B to 280 kPa at position E). Likewise, the difference in pressure at positions C and F became even higher as the head was located at the corner of the space.

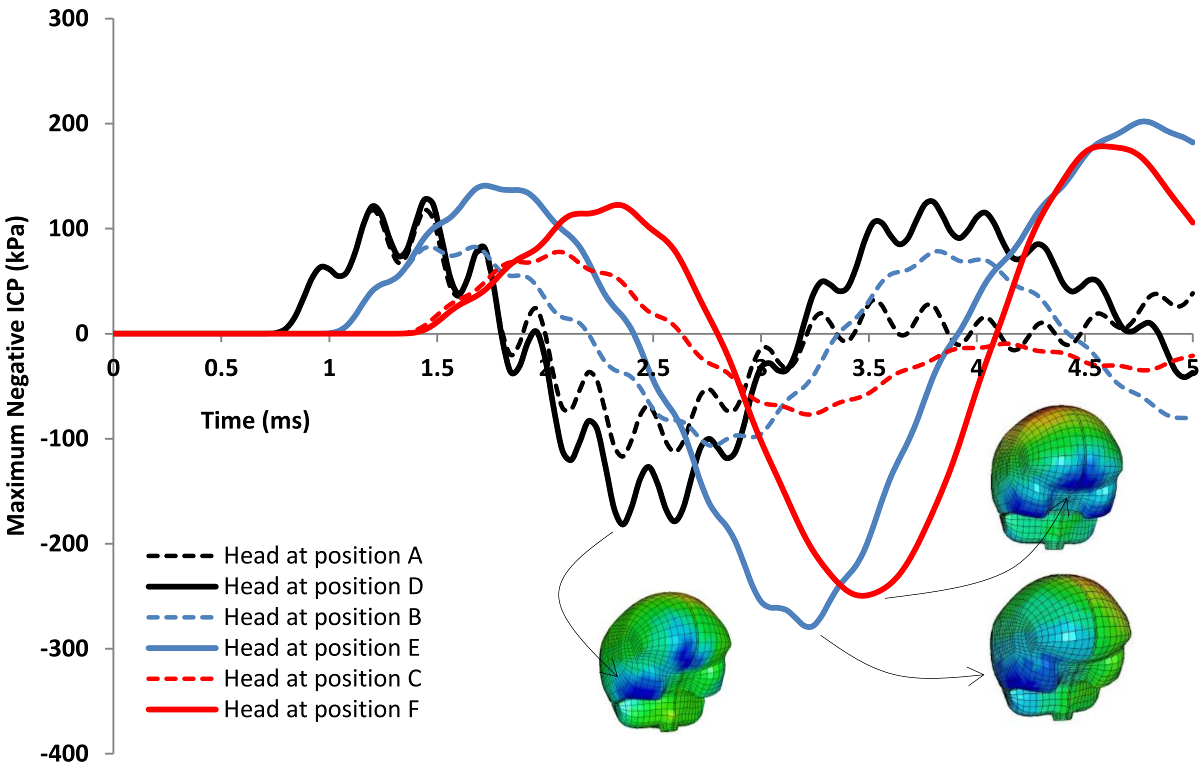

Figure 29. ICP variations in countercoup site for the given positions (59)

6.2.3.3. The head acceleration

For all cases reported in this chapter, rapid acceleration and deceleration waveforms are shown in Figure 30. Similar observation to ICP changes can be reported for the variation of accelerations of the brain. The maximum acceleration and maximum ICP were seen at almost the same time. As a result of reflected blast waves, the head model located in the corner with the largest standoff position experienced a maximum acceleration of about 400g.

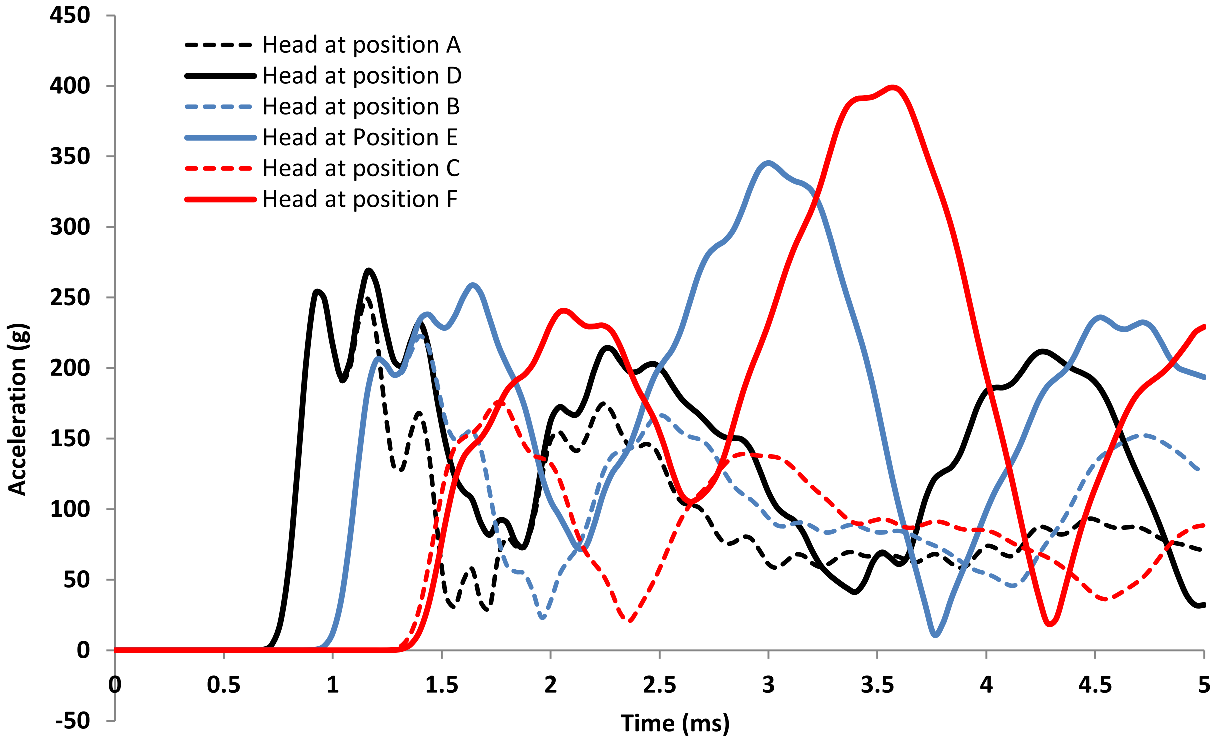

Figure 30. Rigid body acceleration of the brain at different positions (59)

6.2.3.4. The brain shear stresses

Figure 31 depicts maximum shear stresses at different positions. The variation of shear stresses on the brain was measured similar to other biomechanical metrics. The difference in shear stress values on the brains at positions A and D was not significant. Similar to the changes in ICP and acceleration, shear values at position E showed larger increase than that at position E. The largest shear stress value found to be at position F in the brainstem (Figure 31).

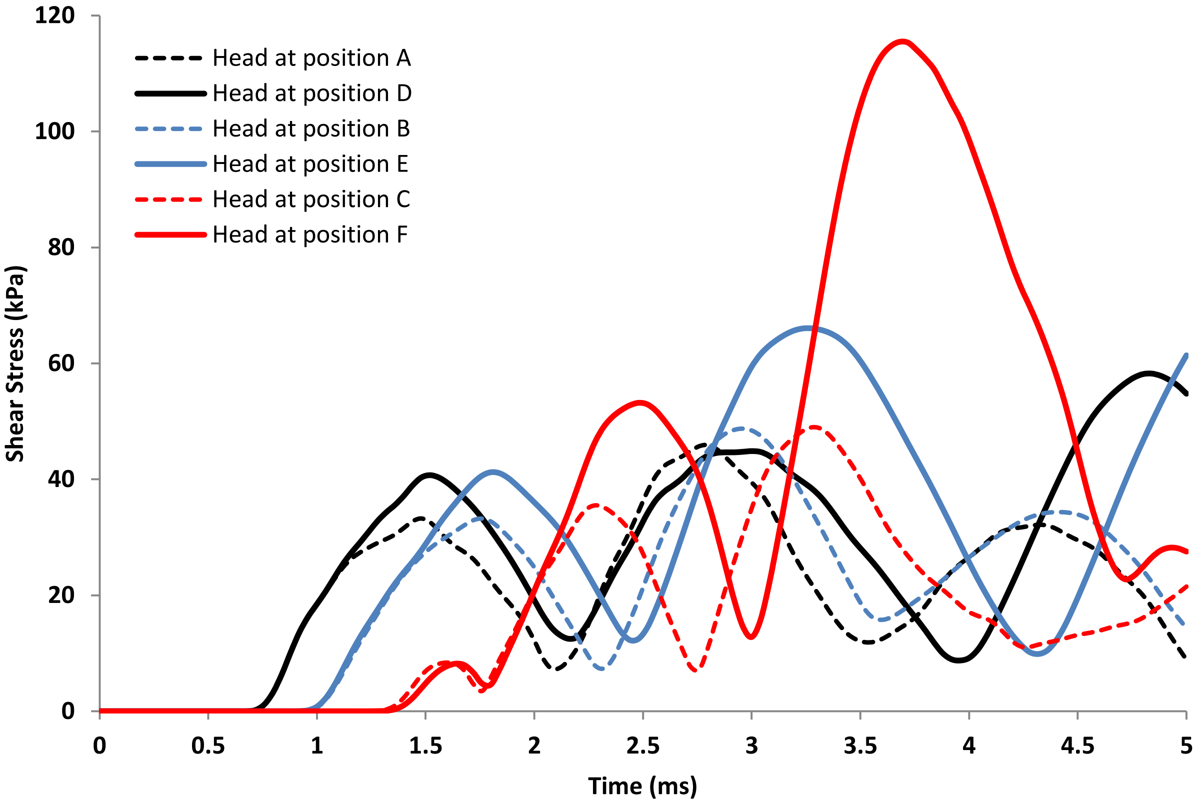

Figure 31. Shear stress variations on brain tissue at the given positions; the incident pressures are shown in dashed lines and the effect of reflected pressure are shown in solid lines. Brainstem showed maximum shear stress in all cases (59)

6.2.3.5. The brain principal strains and stresses

Figure 32 shows principal stresses and strains at positions C and F (the results of other cases are not reported here). The data were collected from brainstem tissue that showed the maximum variations. With the head model positioned at F in the corner, both principal strain and stress values found to be the largest. The strain on the brainstem at F was found to be three fold greater than that at C. Similar discussion would be applicable for principal stress values.

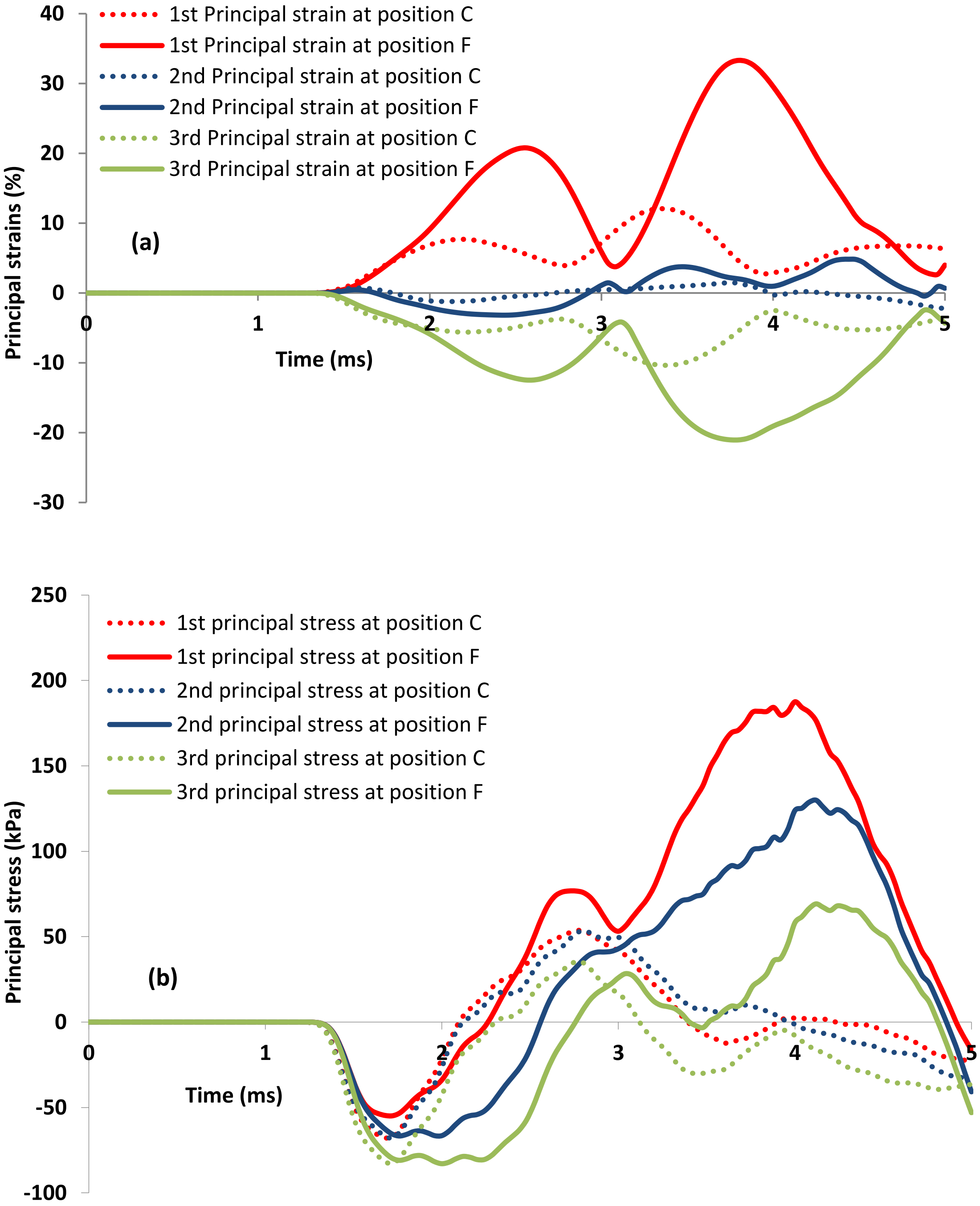

Figure 32. The change in the principal strains (a) and stresses (b) in brainstem tissue (59)

6.3. Discussions

This chapter presented the effect of walls and their reflections on the variation of biomechanical parameters. The head model was placed at different positions and different distances from HE locations. It was shown that the pressure on the skull was as large as 4 to 6 MPa for different scenarios. The level of transferred pressure to the brain reduced to about 150 kPa to 250 kPa due to the presence of CSF (about a 25-fold reduction).

As shown in Figure 25, the increase in pressure due to reflections from wall(s) of confinement was about two-fold. The pressure on the brain and skull, however, did not increase by two-fold. For instance, the skull at position D did not experience a significant increase in pressure compared to the skull placed at the same standoff distance but far from the wall. This may be due to the fact that in this specific location and orientation of the head the pattern of the blast wave was changed as soon as the waves hit the head. The change in the pattern of blast waves might change the direction of reflections not to hit the head or reduce their strength. In such a situation, the position of the head with respect to detonation played an important role.

At positions B and E, the higher pressure rise may be explained in a similar way. Consequently, the overpressure due to the wall was reflected to the head and increased the pressure level on the skull as depicted in Figure 27. For positions C and F, the scenario was the most serious, as there were reflections from both walls to the head, and as expected, the head experienced more reflected shock wave overpressure. The skull and brain underwent a tremendous amount of increase in pressure. The acceleration of the brain and its rate of changes were also increased considerably. A similar scenario could explain the brain shear stresses. Table 7 shows different loading magnitudes in different scenarios as well as the amount of magnification due to the vicinity of the wall.

According to Table 7, magnification increased from case 1 to case 3. The maximum magnifications occurred in the corner, and the skull, for instance, underwent more than a 300% magnification.

Table 7. The skull pressure, ICPs, brain resultant acceleration and shear stress at different locations and the percentage of change when the head is near the wall as compared to the one away from the wall (59)

The head at different positions under blast		Skull pressure (**MPa**)	Positive ICP (**kPa**)	Negative ICP (**kPa**)	Acceleration (**g**)	Shear stress (**kPa**)
Case 1	position **A**	3.41	126.61	-116.86	249.19	32.76
	position **D**	5.27	158.37	-181.68	268.77	58.01
	Magnification %	**54.55**	**25.08**	**55.47**	**07.86**	**77.05**
Case 2	position **B**	2.19	80.13	-100.61	222.7	32.95
	position **E**	4.45	217.54	-278.09	345.3	66.04
	Magnification %	**103.20**	**171.48**	**176.40**	**55.05**	**100.42**
Case 3	position **C**	1.46	69.60	-76.78	175.96	48.98
	position **F**	6.05	236.66	-249.48	398.78	115.46
	Magnification %	**314.32**	**240.03**	**224.93**	**126.63**	**135.73**

Blast as a major cause of TBI was more injurious when it occurred near walls. In such circumstances, the biomechanical parameters on the head were increased significantly. In this research, six different blast scenarios were considered for which the brain ICP, acceleration, shear stress, principal stresses, and strains were determined and compared. The scenarios consisted of pairs of locations in which the head was near or away from the walls. The results showed that the blast wave overpressure was intensified near the walls, but the magnification might not be entirely transferred to the head. In reality, the position of the head and the wall, with respect to the explosive material, could determine whether the reflected pressure waves were transferred entirely to the head. This study also explained that corners intensify the pressure more than other places, as multiple summed reflections were expected from the neighboring walls. In the case studies presented in this chapter, the pressure on the head near a corner was magnified almost four times, and as such the brain could experience a higher level of injury. Similar explanations could be discussed regarding the level of accelerations and shear stresses on the brain tissue.

Comparing the brain biomechanical parameters illustrated that when the head was located near a wall, especially near a corner, not only ICPs, acceleration, and shear stresses on brain tissue could be increased significantly, but they also remained for a longer period of time. According to De Candole (56)**,** in short durations the brain can bear a large amount of overpressure, but if the duration of loading on the head is extended, the tolerance thresholds of the brain drop and injurious scenarios result. As a consequence, the reflected waves hitting the head could considerably increase the level of primary blast induced TBI.

CHAPTER 7. EFFECT OF BLAST IN CONFINED SPACES ON THE HEAD

7.1. Open, Semi-Confined, and Confined Blast Spaces

To examine the impact of the blast environment, the head model was placed in three different spaces (Figure 33a); a closed or confined space where the reflections of the walls were accounted for in the modeling procedure; a semi-closed or semi-confined space, where only the roof was open; and an open space where the roof and the walls across from the detonation were removed so no reflections were realized. The explosive material was inserted at the corner of the computational space on the ground (see Figure 33). The dimensions of the computational space as well as the position and orientation of the head are illustrated in Figure 33b. Three detonation weights of 95, 145, and 215g TNT as HE material were considered for all of the three spaces examined. The stand-off position of the head was 950 mm from the explosive charge and the orientation of the head in all cases was kept constant, looking towards the explosive location. As an important part of the simulation, discretized domain is shown in Figure 33c, illustrating the fine mesh for the HE.

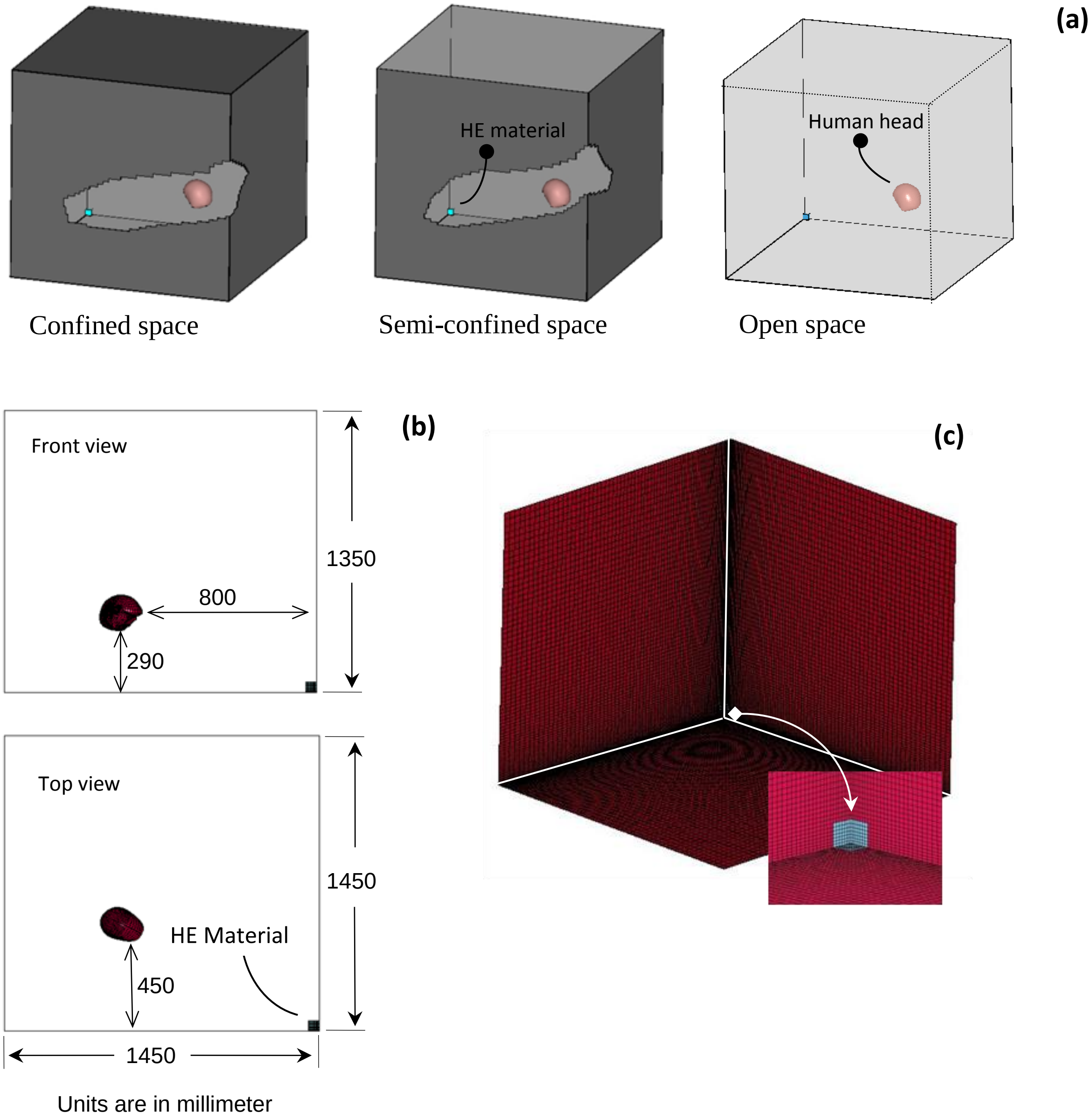

Figure 33. (a) The three blast spaces considered: closed or confined, semi-closed or semi-confined, and open; (b) Geometry of the spaces, position and orientation of the head as well as the cubic detonation; (c) Discretized domain and HE material (60)

7.2. Results

7.2.1. The Shock Waves Pressure

Figure 34 illustrates a comparison of the pressure at two identical locations in the confined space with the corresponding points in the open space. Figure 34a shows a point at about 950 mm from the detonation position, which was located inside the space. The first sudden rises were the same, but in the confined space, there were a number of subsequent peaks due to the reflections which produced pressure gradients comparable with the first peak even after several milliseconds. In the open space, though, the first sudden rise was followed by a drop to a slightly negative value and then predictably converged to the atmospheric pressure.

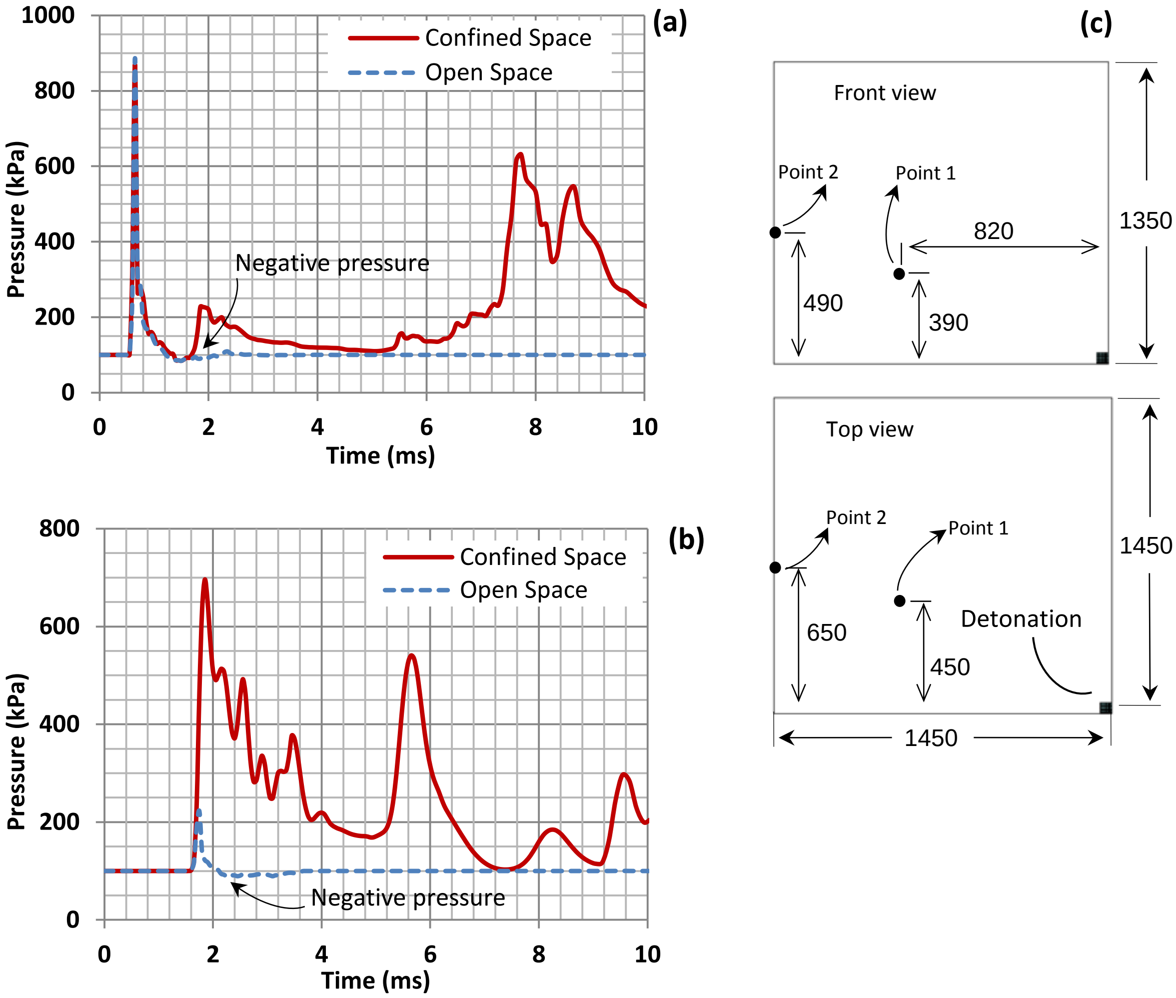

Figure 34. Pressure due to blast of 95gr HE material at two different locations in the confined space and their corresponding locations in the open space: (a) at location 1, inside the space; (b) at location 2, on the wall behind the head, and; (c) approximate locations of the two points in the space (60)

Figure 34b illustrates pressure in a location at about 1650 mm from the detonation position on the wall behind the head in the confined environment and compares it with its corresponding location in the open space. Due to the wall, the amount of pressure at this specific location was magnified about three times compared with that of open space. Also, the following reflected pressures on the wall were notably high and their effects could be seen after the first peak for the particular position. The peaks, created shortly after the initial peak, were reflected from the wall behind the head. But there were a number of considerable peaks such as the ones at about 7.6 ms in Figure 34a and 5.6 ms in Figure 34b that were even more powerful than the ones created before due to the cumulative effect of the blast waves at those locations.

7.2.2. Brain Kinematics

The resultant rigid body velocities of the brain and skull as well as the relative velocity of the brain with respect to the skull were studied under detonation of 215gr HE material for the three environmental spaces considered. As shown in Figure 35, larger differences in the relative velocities were seen at the initial stage once the waves hit the head. In the open space, the velocities converged to an almost constant value after 15 milliseconds (Figure 35a).

The final velocity of the head in the open space was the highest and markedly more than that of the confined and semi-confined spaces. In the semi-confined space, the indirect blast waves due to the reflections hit the head in such a way as to reduce its velocity (Figure 35b). This effect dissipated very soon, contributing to a steady state motion after about 15 milliseconds. In the fully confined space, on the other hand, the fluctuations due to the reflected waves were seen for a longer duration (Figure 35c).

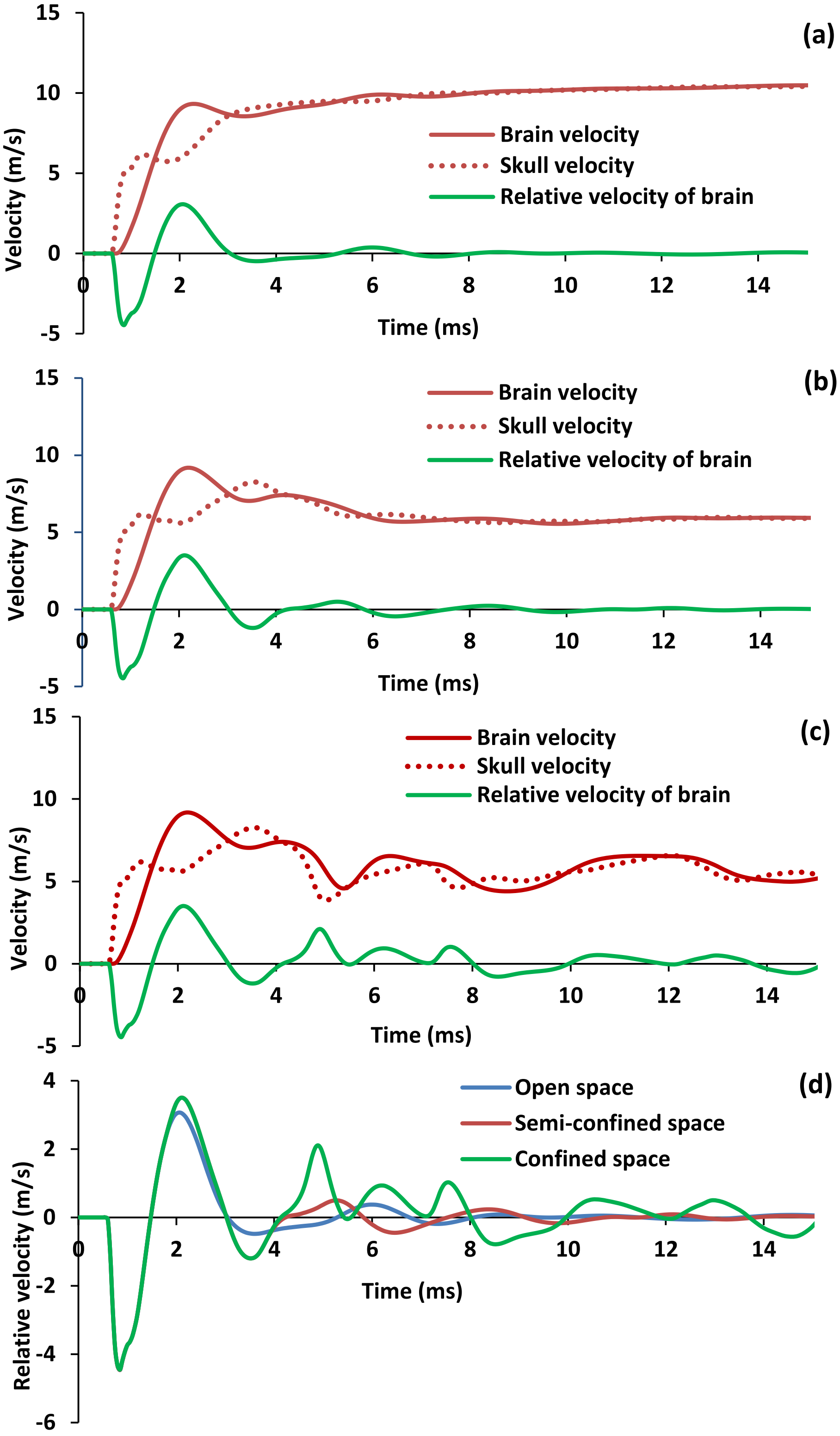

Figure 35. The velocities of the brain and the skull and their relatives under a blast of 215gr HE material in (a) open space, (b) semi-confined space, (c) confined space, and (d) the relative velocities of the brain and skull in all spaces compared (60)

The reflections also hit the head from different direction to reduce or increase the head motion. To compare the motion of the brain, Figure 35d shows the relative velocity of the brain with respect to the skull in different spaces. In Figure 36, the rigid body acceleration of the brain with time is plotted for all three spaces under the detonation of 215gr HE. As seen, the brain initially underwent an acceleration of 1000 G for all cases, but it dropped to zero in the open and semi-confined spaces soon. In the confined space, however, several other peaks due to arrival of the reflected waves from the confined boundaries were shown.

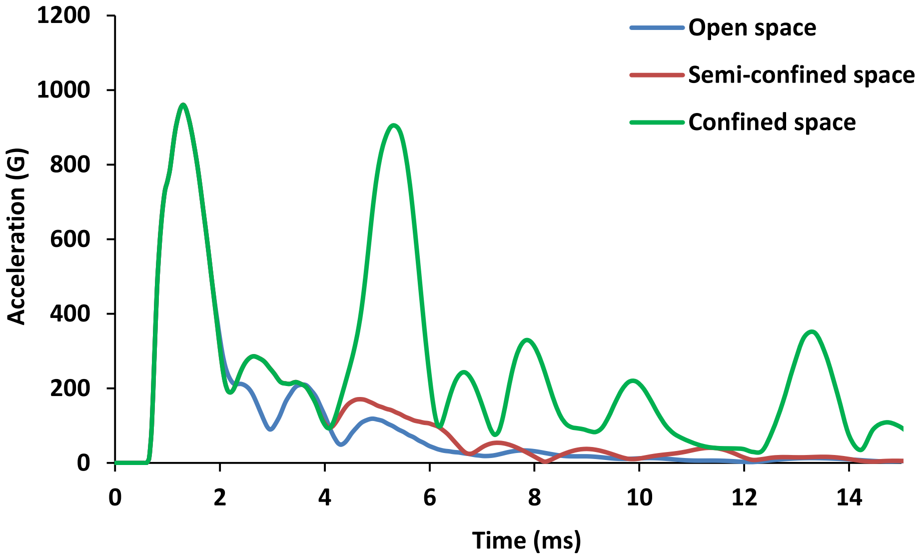

Figure 36. Variation of the brain rigid body acceleration at its center of gravity over time when imposed to blast shockwaves of 215gr HE material (60)

7.2.3. Brain ICP

Figure 37 shows the ICP contours of the brain when the head is subjected to blast waves in the open space. The pressure distributions in coup and contrecoup sites were presented at different times for the first few milliseconds of the blast wave incident. As depicted, different parts of the brain at different times experienced positive and negative pressures, with the temporal lobe bearing the most.

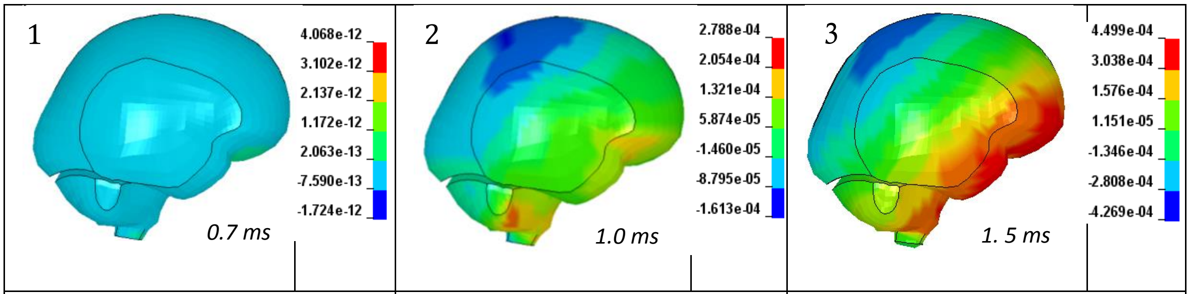

Negligible ICP

Max: Midbrain, Min: Parietal lobe

Max: Temporal lobe, Min: Parietal lobe

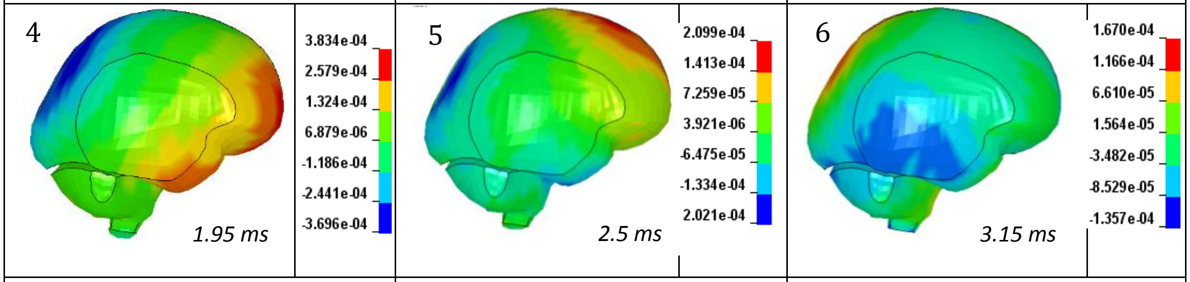

Max: Frontal pole, Min: Occipital lobe

Max: Frontal pole, Min: Occipital lobe

Max: Occipital lobe, Min: Temporal lobe

Figure 37. ICP (GPa) contours of the human head model in the open space at different times after exposure to blast waves of 95gr HE with the areas of brain bearing the maximum and minimum pressures at each time (60)

Figure 38 shows the averaged values of ICP with time in the temporal lobe against different amounts of HE for all the environments. As expected, when increasing the charge weight, the ICP was increased accordingly in the brain. In order to evaluate the response of the brain in different spaces, ICPs due to blasts of 145gr HE were also compared (Figure 39). While the maximum ICP for all of the cases were nearly the same, it is clearly obvious that the brain experienced the most pressure variations with a longer duration in the confined space.

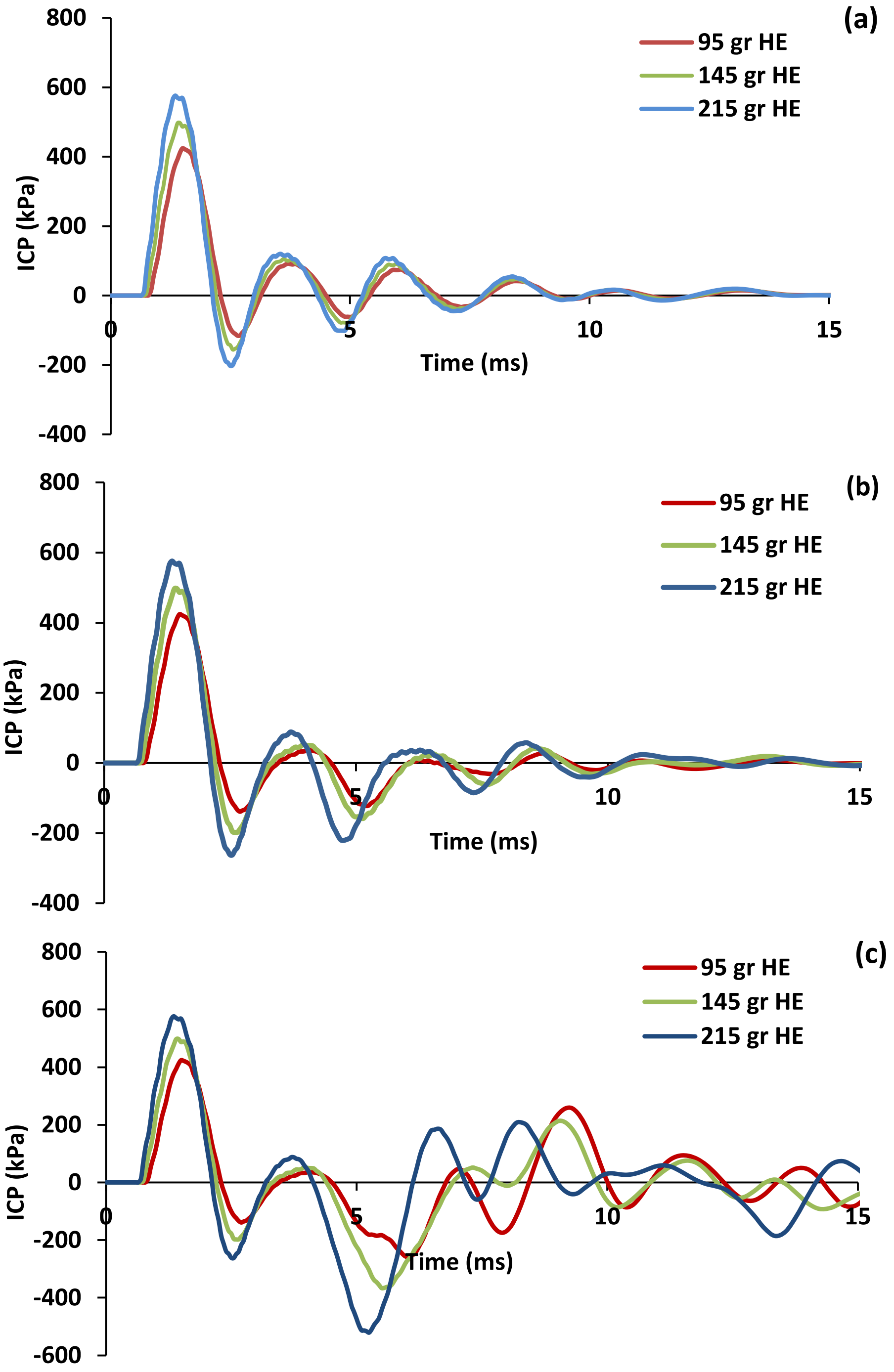

Figure 38. ICP variations in coup site of the brain (temporal lobe) under different blast intensities in: (a) open, (b) semi-confined, and (c) confined space (60)

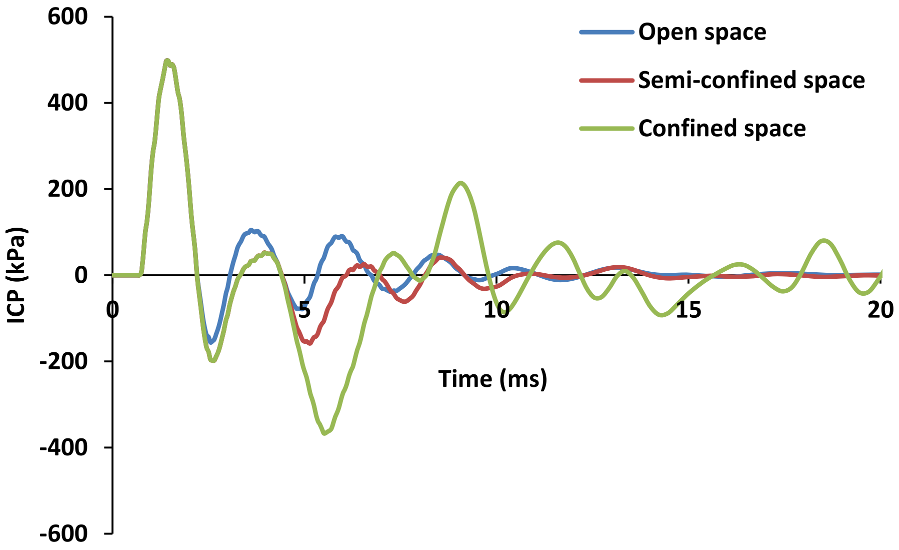

Figure 39. ICP variations over time in coup site of the brain in all spaces for explosions of 145gr HE material (60)

7.2.4. Brain Shear Stress

The variation of shear stress distributions on the brain are shown in Figure 40in blast scenario. Unlike the ICP distribution, the shear stress distribution did not have a predictable pattern due to complexity in brain geometry and its material properties. Variations of shear stress over time on two different regions of the brain are also illustrated in Figure 40. Shear stress in a region on the temporal lobe presented a similar pattern and values in all three scenarios with only a slight difference in the open space (see Figure 40a). The observation however, showed that the highest shear stress happens in the brainstem region, and as shown in Figure 40b, there was a large discrepancy between the shear stress fluctuations in the confined space and the other two environments.

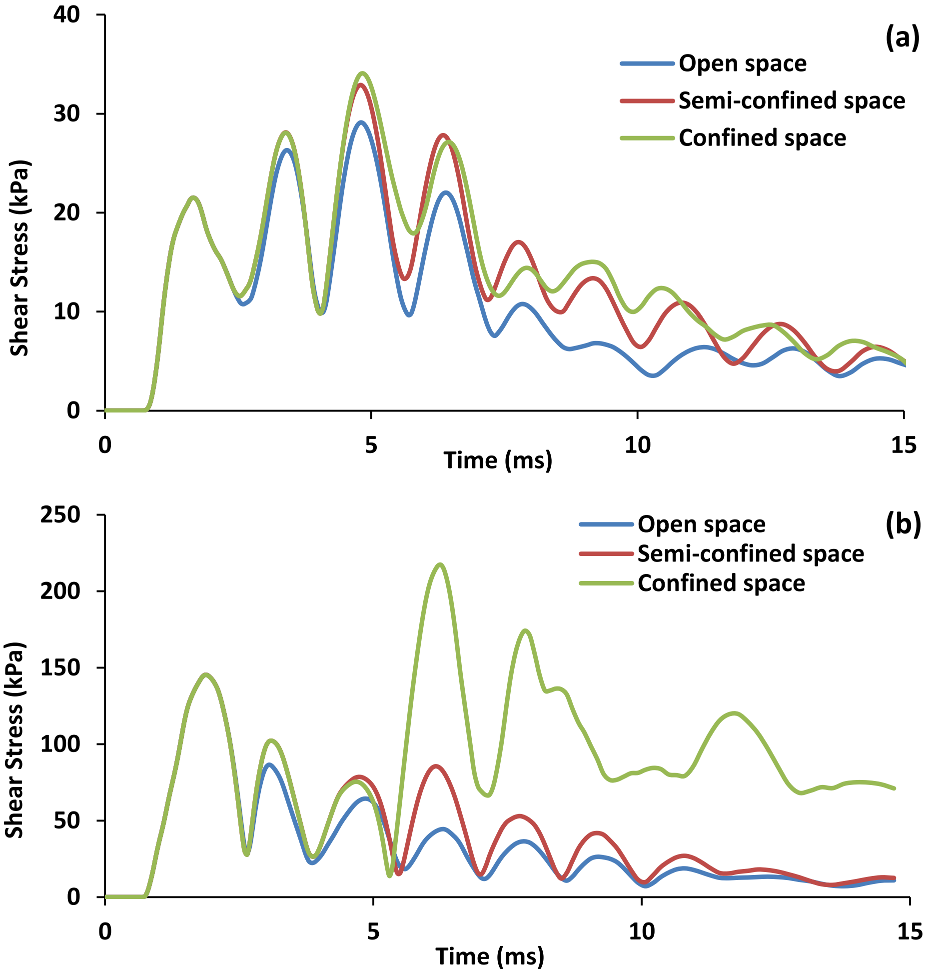

Figure 40. (a) Average shear stress with time in temporal lobe (b) in brainstem, bearing maximum shear stress, under the blast of 145gr HE material (60)

7.3. Discussion and Conclusion

From a clinical point of view, it is crucial to have an understanding of what happens in confined spaces, as such environments are more prone to cause head injuries during explosions. With no doubt, most computational studies on the blast-head interactions have provided remarkable insight on the behavior of the brain under different blast situations. They, however, have presented the behavior of the brain for the first few milliseconds after the blast such that the brain motion has not been studied. In addition, the effect of confinement and walls, producing reflections, have not been seriously investigated. Our current study investigated the effect of walls in the confined and semi-confined spaces under different explosion intensities compared with that of the open space. Data was collected for about 40 milliseconds to follow the behavior of the walls until the reflections disappear. This chapter also examined the reasons for the harshness of the situations in confined spaces.

The walls in semi-confined and confined environments produced reflections which might add to the biomechanical parameters already created by the direct shock waves. The impact of reflections was very difficult to evaluate or predict at any point and any time in such 3D physical domains. They could amplify the cumulative effects in one place/time or otherwise at another place/time. According to Figure 36, the brain rigid body acceleration in the open space included one peak followed by successive peaks, which were comparatively small and vanished in a matter of a few milliseconds. In the confined space, on the other hand, the reflections caused successive jumps at the later stages, producing motion and acceleration for a longer duration, and consequently, further peaks. The generated ICP in the open space gradually diminished with time, usually after about 10 milliseconds, regardless of the HE weight (Figure 38a). The highest amount of pressure was realized on the head after approximately 1 millisecond. The averaged ICP buildup with time in the semi-confined space was slightly harsher, but behaved similarly to that of the open space (Figure 38b), and the pressure dissipated after nearly 15 milliseconds. In the confined space scenario, however, the pressure lasted notably longer and lessened more slowly (Figure 38c) as the explosive material could not leave the space. The pattern of shear stress was also explained similarly in different spaces. The brainstem in the open space suffered less and in the closed space experienced the most shear stress (Figure 40b).

The level of severity cannot be evaluated according to different available criteria. For instance, head injury criterion (HIC) derived from acceleration-time history, is based on skull fracture and not brain injury. More importantly, they are mostly applicable for low-velocity impacts in which the duration is more than three milliseconds (79). There are also a number of thresholds that have been previously proposed such as an ICP threshold of 235 kPa by Ward et al. (80) or shear stress threshold of 8 to 16 kPa by Anderson (81). However, these thresholds have not considered the duration and time-history characteristics, but it is acceptable to compare these injury-related parameters in the open space with the ones in the confined or semi-confined environments.

Considering Figure 36, Figure 39, and Figure 40a, it was shown that the earliest peaks in all cases were identical, indicating that the head, at this point in time, suffered from the direct shockwave from detonation only. The impact of reflected waves was not realized yet. In the open space scenario, the shockwave overpressure passed quickly and diminished in a matter of few milliseconds. In the semi-confined space, the direct and reflected waves exited from the open-top surface, so their impacts diminished much faster than the fully confined space. The discrepancies in the parameters such as ICPs for the confined space in comparison with those of open and semi-confined space settings were notable. Many fluctuations in all of the parameters in this case were not predictable, because the pattern of the overpressure on the head changed due to the surrounding walls. Also, the durations for all scenarios showed that the blast waves could not exit quickly in confined spaces and it took much longer for the blast energy to be diminished. Thus, the effects of environmental situations in confined spaces were much more severe as indicated by the number of sudden increase/decrease and the duration of the parameters.

To form an appropriate picture of why the situation is more injurious to the brain in closed spaces, mechanical properties of the brain can be considered as a key factor. Brain, materially, is viscoelastic, having a time-dependent behavior and a phase lag between the input stress and output strain. While the first peaks, due to the direct shock waves in Figure 36 and Figure 39 were the highest levels of acceleration and ICP respectively, the rest of the peaks were markedly important for the brain. After the first peak, the deformed region of the brain tended to return to its original position once the overpressure was removed. In open and even semi-confined settings, this might happen, as the fluctuations after the first peaks were negligible. In the confined space, however, the brain experienced subsequent overpressure loads. For instance, note Figure 39 in which the magnitude of negative pressure after 5 milliseconds was similar to the earliest peak positive pressure in all scenarios from the impact of reflected waves on the posterior aspect of the head. In such situations, while the brain tissue was deformed by the first positive peak overpressure, it suffered a negative overpressure due to the reflections in the opposite direction shortly afterward. In such a case, the brain tolerated the strain even after the first peak vanished due to the phase lag and, at the same time, experienced more fluctuations. For brain tissue, these circumstances were catastrophic and could create additional damage to the cells and axons. Therefore, direct blast waves together with indirect waves in confined environments contributed to cumulative injuries, increasing the risks of PBI due to transferring more damaging energy to the head. The semi-confined space, on the other hand, behaved similar to the open space in that the first peaks of the biomechanical outputs were dominant, and one could neglect the remaining fluctuations. In light of the increased severity of injury which occurred from blast in closed environments, the study suggests adding feasible openings or pressure relief systems in structures or vehicles which may be potentially subject to explosive forces. This may improve survivability, as the particularly harmful aspects of blast in closed environments are minimized.

CHAPTER 8. BRAIN PRIMARY VS. TERTIARY BLAST INJURIES

8.1. Modeling for the Assessments of Brain PBI and TeBI

In the case of a blunt impact, an object hits only the head while the whole body stands still. In this case, after only a few milliseconds, the impact will be realized by the neck and then the rest of the body. Therefore, analyzing a human head model without torso for longer durations certainly invalidate the results. In a blast scenario, on the other hand, the blast wind hits both the head and the body and throws the whole body in the direction of the airflow (which is different from a blunt impact situation). However, the surface areas as well as the densities of the head and the body are not the same which makes them move very differently. Considering the fact that the head was close to the wall in chapter 6, the simplification of neglecting the body was logical, so it might be hypothesized that even the entire body traveled at nearly the same velocity until striking the wall. This fact could also be seen in the research of Fletcher and Bowen (69) on the translational effect of the blast wind.

The focus of the literature has been mainly on PBI. Salimi Jazi et al. (68) also studied the effect of the attached body on the biomechanical responses of brain tissue in an open-space blast scenario. They showed similar ICP and shear stress for the cases of head-neck free floating and attached torso to the head. Sarvghad-Moghadam et al. (82) also studies the effect of face shield in the mitigation of blast primary TBI. This chapter is thus focusing on the additional mechanical stresses and strains due to physical impact of the head with an obstacle or wall on top of the PBI due to blast, contributing to brain blast-impact trauma.

8.2. Biomechanical Data for Assessment of TeBI

Due to its complex architecture, the cross sectional geometry of the head varies, depending on the plane being considered. This results in different responses under insult from different directions. Frontal, occipital, and side impacts cause different ICP gradients, with occipital impacts having the highest ICP (63). Analysis under occipital impact is, therefore, a good scenario for the study of a tertiary blast injury (TeBI) assessment. Figure 41a shows an impact of the head with a rigid wall with data collected from an area of the occipital lobe. As the velocity of the head increased, the value of the ICP increased, but the duration of ICP elevation became shorter.

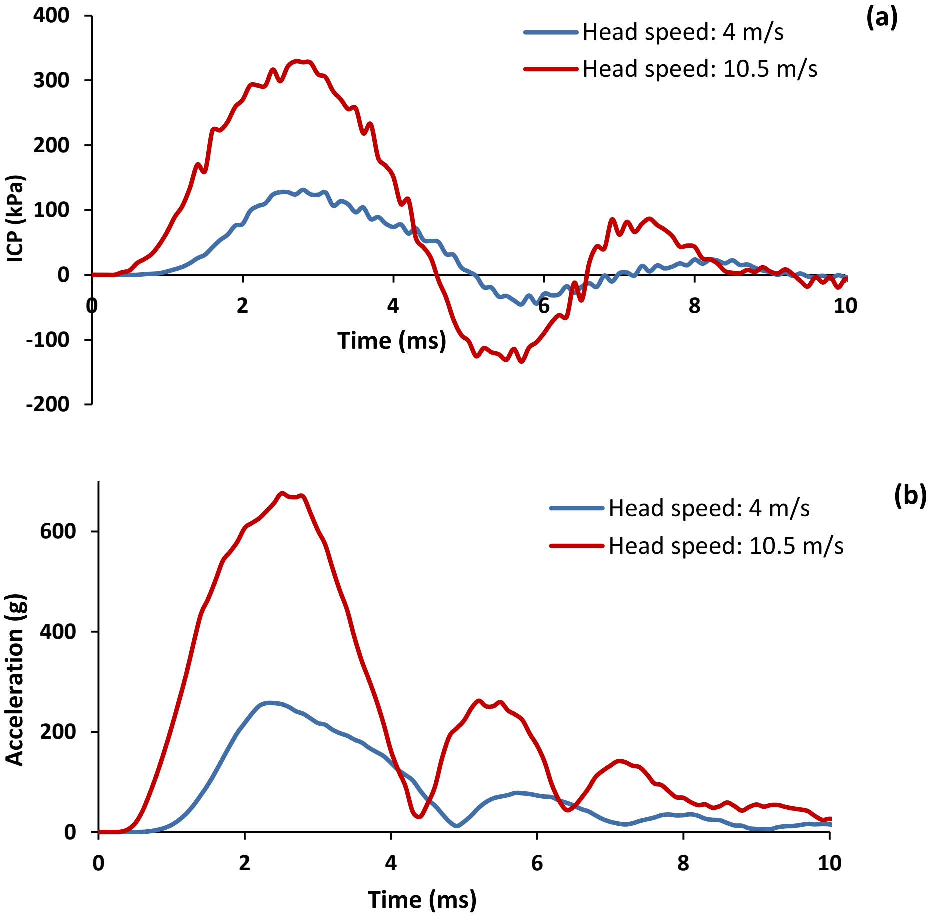

Figure 41. (a) ICP variation in occipital lobe and (b) brain rigid body acceleration under occipital impact of the head with a rigid wall over time (61)

Figure 41b shows that the rigid body acceleration displayed similar characteristics. It should be noted that all of the biomechanical parameters plotted were averaged values from specifically mentioned areas of the brain.

8.3. Methods of Modeling PBI and TeBI

Figure 42a shows the order of events from the point of detonation of a 95 g HE charge, the generation of shockwaves, exposure of the head to the waves (PBI), the head striking the wall, and the contours of the brain ICP (TeBI). Figure 42b further illustrates the development of ICP with time created in such a scenario.

During the interval between the dissipation of the blast overpressure and the onset of the impact of the head with the wall, brain stresses/strains were reduced to normal (the green region interval in Figure 42b). The analysis of PBI and TeBI can be performed separately. In the first analysis, PBI was considered, and kinematical and mechanical parameters were determined. In the second analysis, the final velocity of the head, due to the PBI, was used as the input parameter for the determination of the TeBI that occurred under head impact and it was assumed that there were no residual stresses/strains from the PBI analysis (61).

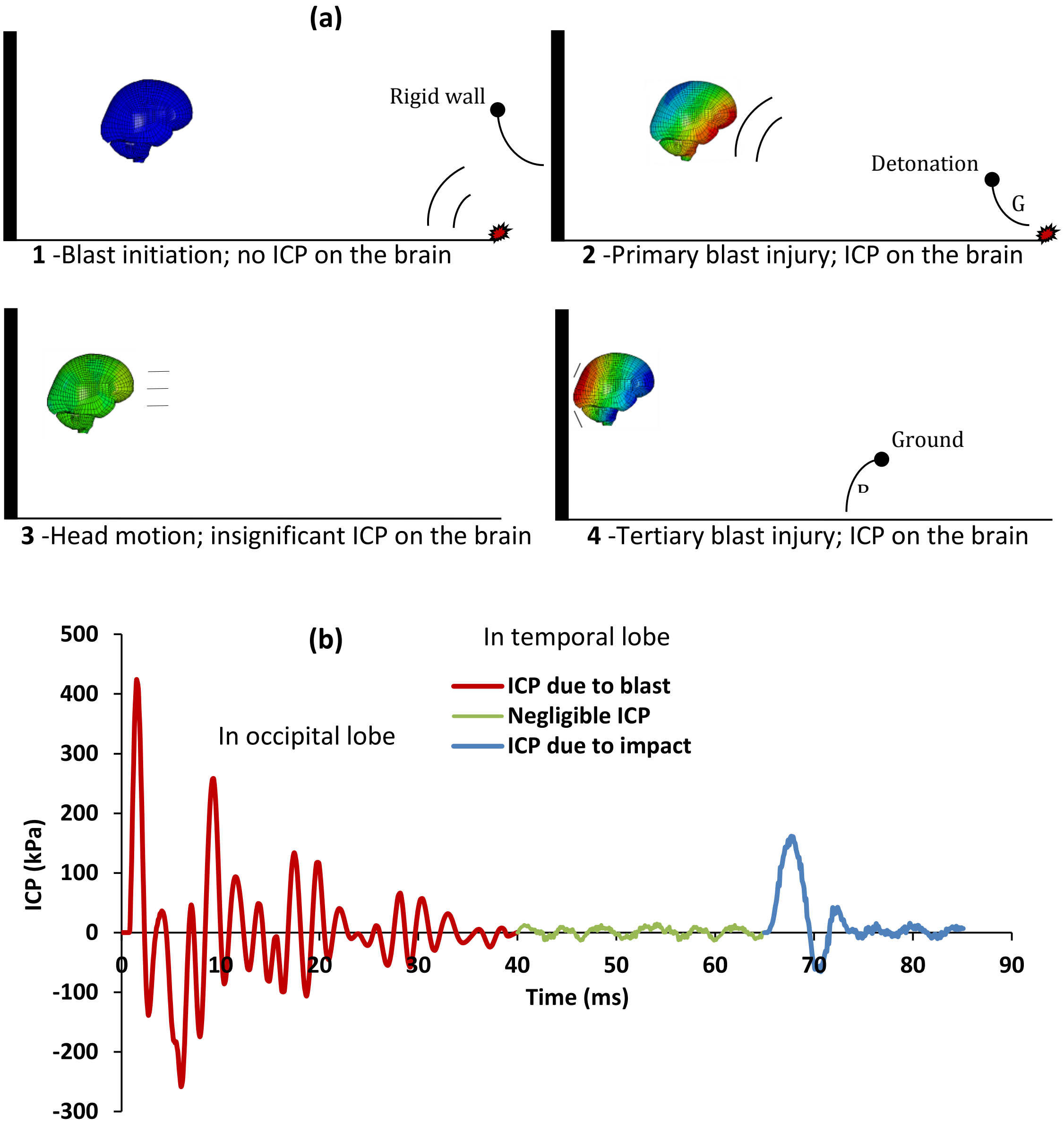

Figure 42. (a) Schematic representation of the setting for a combination of PBI and TeBI when the head was hit by blast load (95gr HE) and then struck the wall (b) ICP variation over time (61)

8.4. Results

8.4.1. Biomechanical Data for Assessment of PBI

8.4.1.1. Brain ICP and shear stress

The averaged values of the ICP over an area of the temporal lobe are plotted vs. time in Figure 43a, following the explosion of 95g of HE in the two space settings. It is shown that in both environments, the first peak of ICP, due to the direct shockwave effect, was almost identical. Over time, however, the ICP in the confined space deviated from that in the open space because of the interactions of the blast waves with the walls of the confined space and the creation of reflected waves which subsequently hit the head.

To better visualize this, Figure 43b shows the brain ICP contours when the head was exposed to a 95g HE blast in the open space. As shown, different parts of the brain suffered from the variation of ICP in coup and contrecoup sites. The negative ICP in the contrecoup site was due to the dynamics of the head components, but it was amplified in the confined space due to the addition of reflected blast waves. In both the open and closed spaces, the ICP reached its maximum in the temporal lobe because of the fact that this part of the brain was the first part exposed to the blast.

The average shear stress with time in an area of the temporal lobe is illustrated in Figure 43c. As shown, in the case of the confined space, the temporal lobe sustained higher shear stress with longer duration due to the addition of exposure to waves from wall reflections. After about 40 milliseconds, the blast wave overpressure strength diminished and, consequently, the entire load on the head was removed, although the head was still in motion.

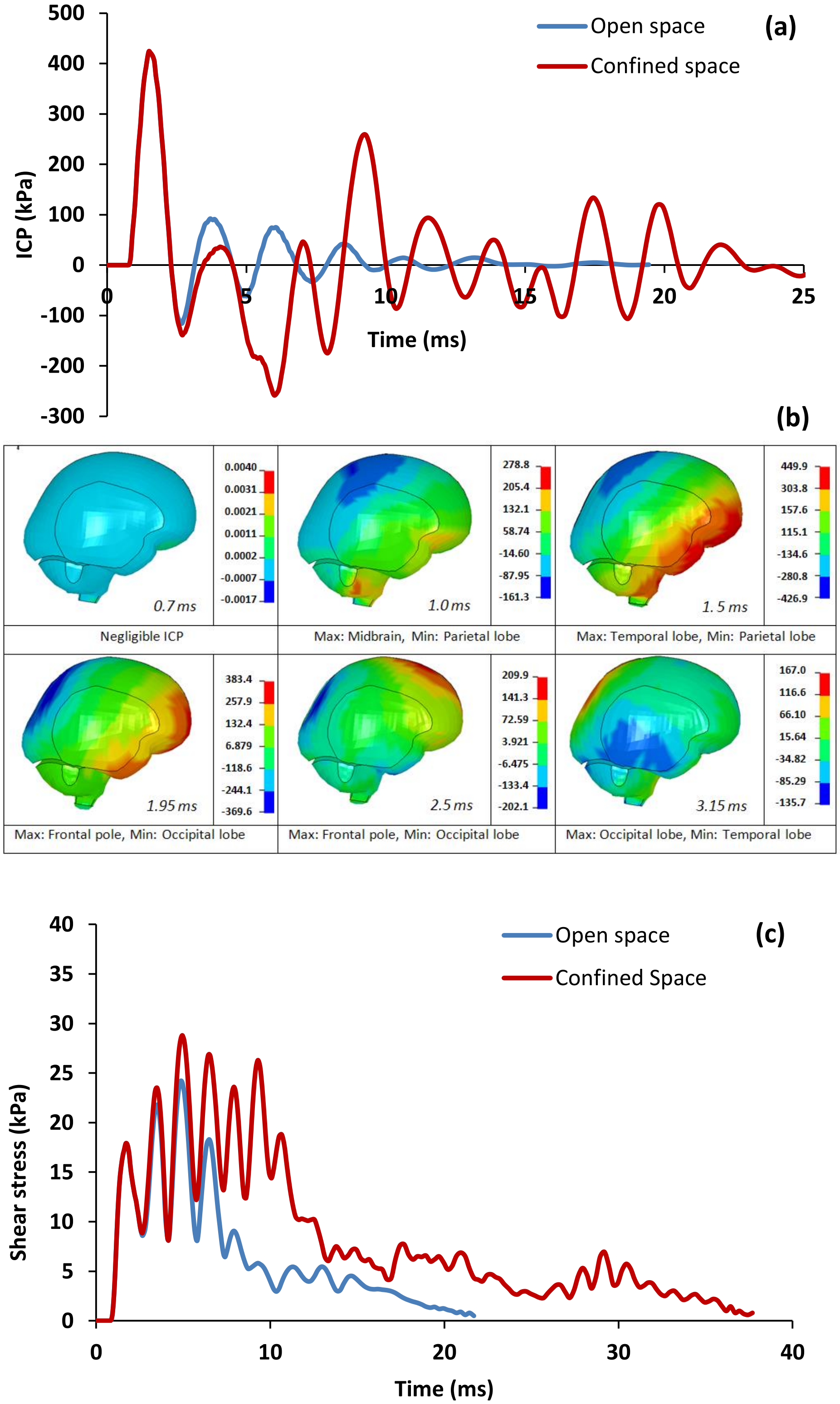

Figure 43. (a) Comparison of averaged ICP in the temporal lobe; (b) ICP contours of the human brain in the open space; (c) Shear stress change in the temporal lobe; all from 95g HE charge (61)

8.4.1.2. The head motion in different blast space settings

Figure 44 shows the velocity of the head in the two space settings with different amounts of HE. As expected, the brain was initially accelerated rapidly at the onset of the exposure to blast waves, followed by a sudden transient deceleration due to the negative ICP that was produced immediately after the shock front. In the open space environment, the brain then accelerated at a slower pace until reaching a constant speed. In all of the cases, the damping properties of the air were ignored so that the head traveled steadily after the waves' strength diminished. In the open space scenario, the speed became steady after about 15 milliseconds. The situation in the confined space, however, was different and complicated with the reflections lasting longer and reducing the speed of the head when they acted opposite to the head's direction of movement.

As the weight of the HE charge increased, the magnitude of the overpressure increased and caused head motion of higher velocity (see Figure 44a-c). In the open space, the increase in velocity was clear and predictable, but in the confined space scenario it became difficult to predict. In Figure 44, many fluctuations in the velocity of the head model were seen in the confined environment, and the final speed of the head was clearly different from that in the open space. As depicted, the speeds of the skull and brain finally converged to an almost equal value after about 40 milliseconds. It should be mentioned that there might be slight changes in velocities in the confined space if the simulation continued, but they would have been insignificant as the energy of the blast waves and their reflections had kept dissipating over time. Using 40 milliseconds as the simulation time, therefore, seemed reasonable.

Figure 44d shows the velocity of the brain and skull over time under different HE charge weights in the open space setting, helping to examine the effect of the intensity of the blast on the velocity of the head. Unlike the confined space, the velocity was proportional to the HE charge weight as expected.

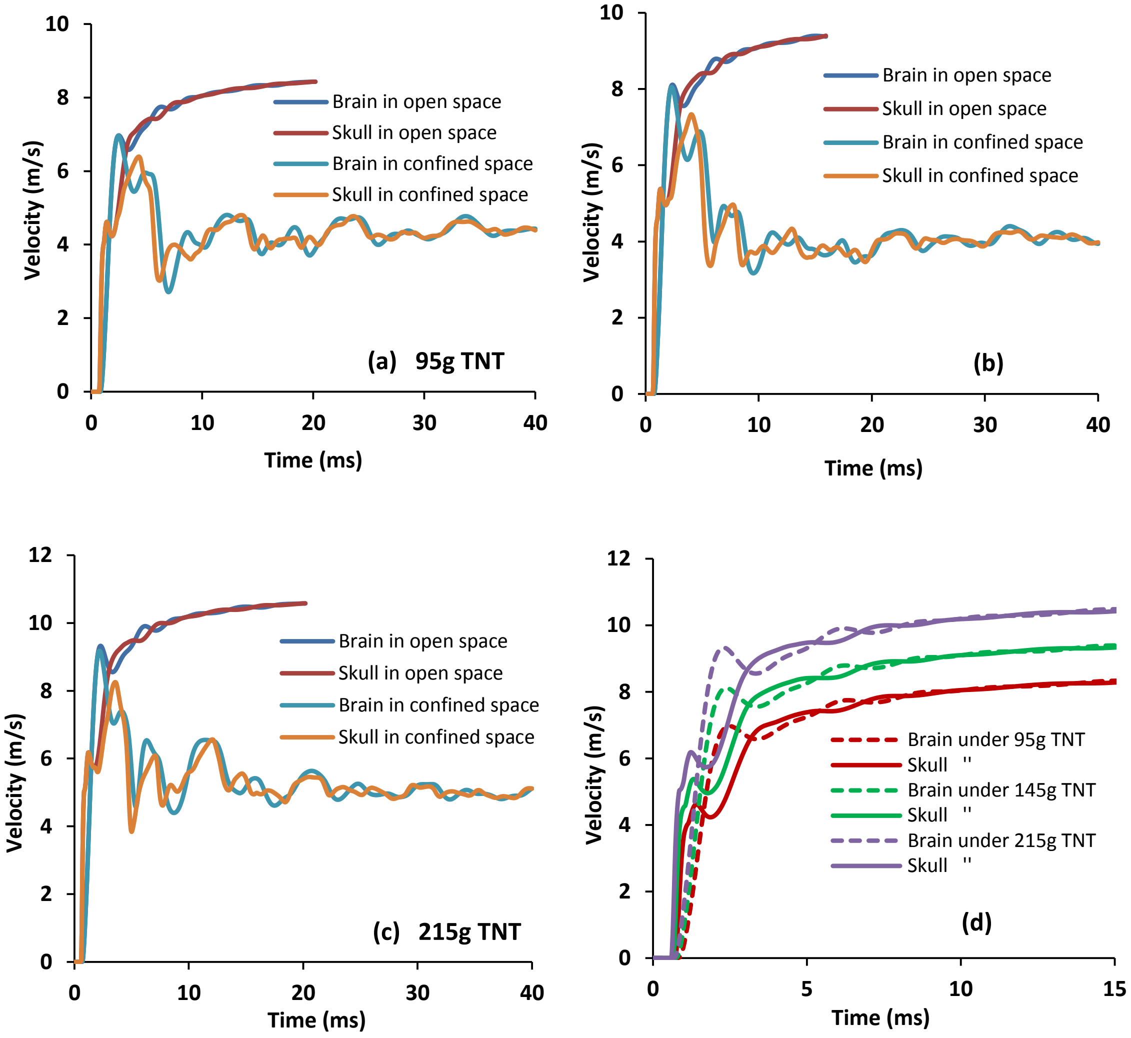

Figure 44. Velocity of the skull and brain in the two spaces under: (a) 95g, (b) 145g, and (c) 215g HE material; (d) Velocities of skull and brain in the open space (61)

8.4.2. Comparison of Biomechanics Data for the Two Space Settings

8.4.2.1. Open space

With no walls in an open space setting, the head continues in motion even after the blast wave passes. It is easier to understand the motion in an open space than in a confined space environment. Consider the case of a blast from 95 g of HE. The front of the head is exposed to blast waves and a confronting rigid surface is assumed to follow fairly close (400 mm) behind it (Figure 45a). As the head starts moving under the impulsive load of the shockwave, it impacts the rigid surface. In Figure 45, the ICP in the coup site of the brain, due to blast wave overpressure (red line) and occipital impact (blue line), are compared for the open space setting. While the ICP in the coup site of the brain (temporal lobe) reaches 424 kPa due to the blast, its maximum due to the blunt impact (occipital lobe) with the rigid surface is 267 kPa. The velocity of the head, due to the blast wind, approaches 8.5 m/s prior to impact with the rigid surface. Similar data for the ICP are shown in Figure 45b when the HE charge weight increases to 215 g.

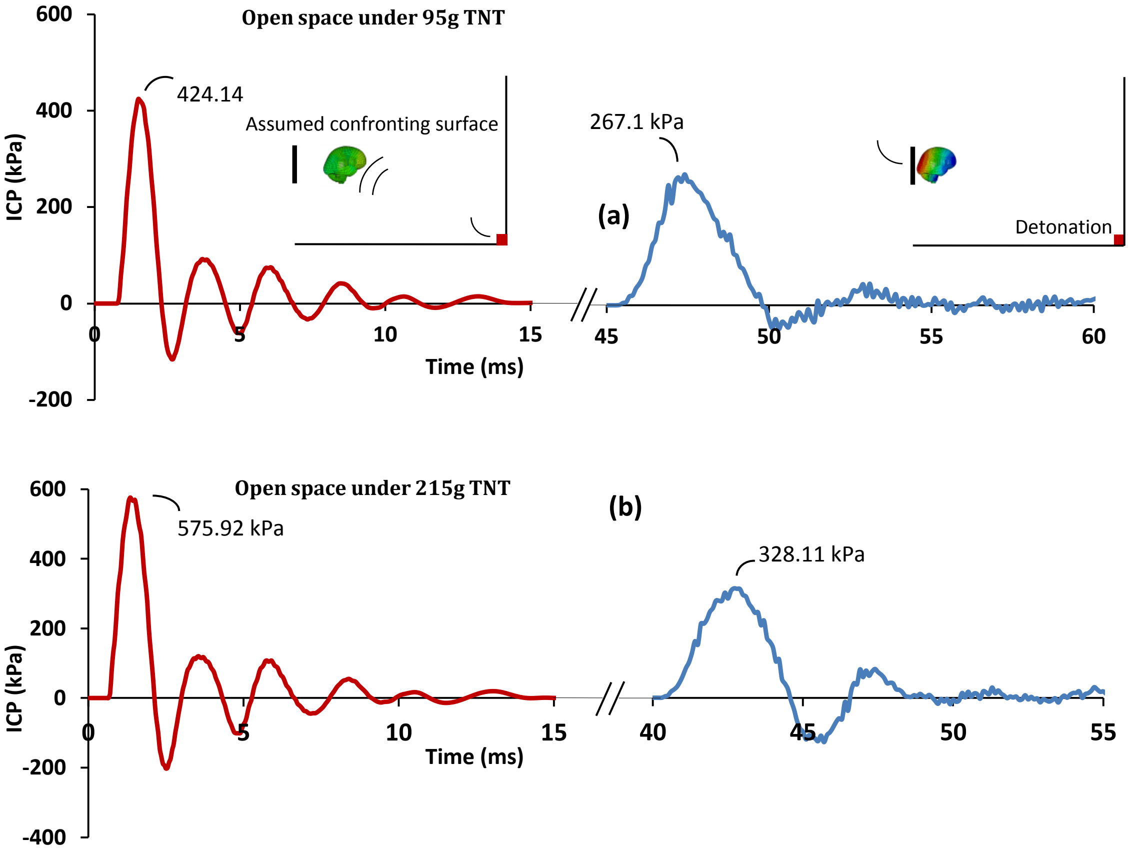

Figure 45. ICP change with time in the open space under PBI and TeBI of: (a) 95g HE with head velocity of up to 8.5 m/s, (b) 215g HE with head velocity of up to 10.5 m/s at impact; ICPs from blast and impact collected from temporal and occipital lobes, respectively (61)

8.4.2.2. Confined space

According to Figure 44, in the open space setting, the maximum speed of the brain and skull was much higher than that in the confined space setting. This is due to the reflections from the enclosing walls working against the accelerating head model. Figure 46a shows ICPs when the head was placed in the confined space and subject to the detonation of a 95g HE material. For the confined space, the ICP at the initial stage of exposure to the blast wave was greater than that resulting from impact with the rigid surface. In Figure 46b and c, the rigid body acceleration and the shear stress are plotted in the confined space setting and it is noted that, as with the ICP, the impact results were much less than the blast results. In Figure 46c, the maximum shear stresses were 30 and 15 kPa, due to shockwaves and impact, respectively.

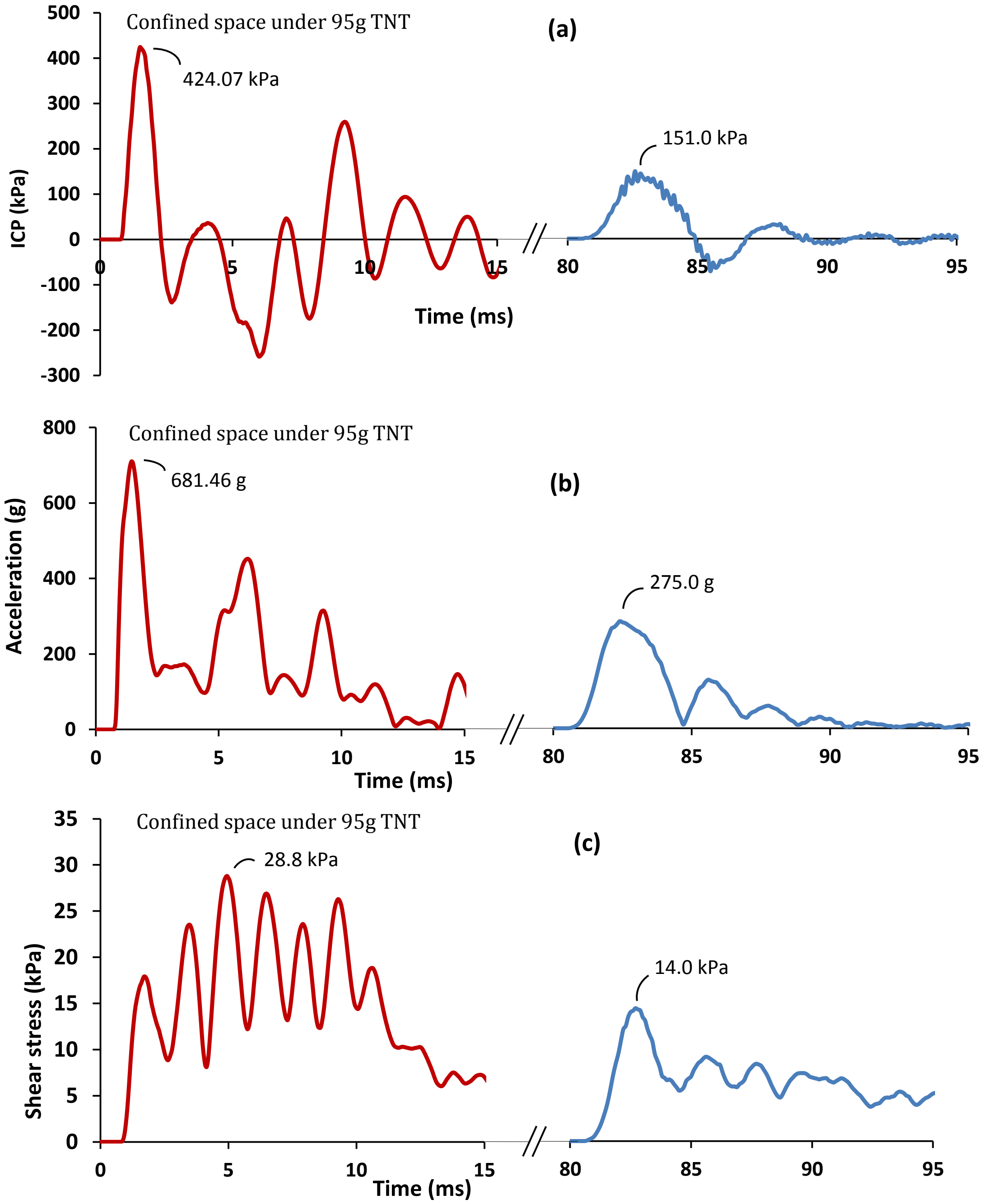

Figure 46. Brain under blast of 95g HE and corresponding wall impact (4.3 m/s) in confined space; (a) ICPs from temporal lobe under blast, and from occipital lobe under impact, (b) rigid body acceleration, and (c) shear stress from areas sustaining maximum ICPs (61)

8.5. Discussions and Conclusions

PBI has been studied for several years while TeBI has barely been examined. Both PBI and TeBI have their origins in a blast, but the mechanisms of the two injuries are different, which makes their comparison interesting. In particular, PBI is a silent injury and, while the brain can be severely injured, there is no sign of external trauma. TeBI, however, can lead to skull fracture along with external signs of injury. In this chapter, analyses were carried out in two blast settings; open and confined spaces, to examine the effect of the blast environment on selected biomechanical parameters. Different weights of the HE charge were considered to show the influence of the blast intensities. The velocity of the head was a function of the blast intensity and has a major effect on the level of the blunt impact load on collision with the enclosing wall.

As seen in Figure 45a, in the open space setting the brain initially experienced a sharp rise in ICP due to the blast. ICP values oscillated at a high frequency as they diminished. Under the blunt impact, an elevated ICP at a markedly lower frequency was recorded, but the initial peak value was nearly 40% less. Compared to the blast wave, after the first ICP peak due to the blunt impact, fewer fluctuations were observed. For both the blast-wave and impact-related ICPs in the open space setting, the fluctuations in this mechanical parameter were negligible compared to the initial peaks. When the HE weight in the open space environment increased from 95 to 215 g, a 36%, increase in the maximum ICP was found due to blast waves and a 23% increase due to the blunt impact with the obstacle. This demonstrated that increasing the HE charge weight in the open space setting had a more pronounced effect on the magnitude of the shockwave ICP than on the blunt impact ICP. If an ICP value of 235 kPa was used as a threshold for injury, as proposed by Ward et al.(80), ICP values from both PBI and TeBI exceeded this threshold in the open space environment. PBI, however, was found to be more serious.

Figure 46 shows the variation of mechanical parameters in the confined space under 95g HE, and, in contrast to the open space environment, the pattern of the ICP variations was very complex and unexpected. There were several sizeable peaks following the initial spike in ICP, which made the analysis more difficult. Also, the duration of different loads on the brain was markedly longer than in the open space environment, and this likely played an important role in causing different types of injury (55), due to transferring of more energy to the brain tissue. To compare the injury-related mechanical outputs, therefore, it is crucial to assess the whole response of the tissue. The waveform analysis gave a good image of what happen to the brain tissue, and demonstrated that the concern was not only the first peak, although it might be the highest. Since the brain was viscoelastic, having a phase lag between the input load and output response, the effect of these fluctuations on the tissue was cumulative, and this caused more severe injury. In this regard, the number of peaks and their duration were significant in interpreting the injury-related mechanical parameters. Figure 46a shows ICP fluctuations with variable frequencies and longer durations than in the open space environment shown in Figure 45a. Rigid body acceleration, as well as shear stress on the brain in the confined space, followed a similar trend to ICP. The injury-producing environment in the confined space was, therefore, even more severe.

Comparison of the PBI and TeBI parameters in the closed space environment with the open space scenario revealed that the velocity of the head was decreased in the closed space due to blast wave reflections. The reduced head velocity produced a lower level of impact trauma. The effect of the direct and indirect blast waves on the head, however, created an overall highly injurious situation. The data clearly showed that all the brain PBI mechanical outputs were dramatically higher than their TeBI counterparts. In the case of impact trauma, since the first peak was dominant, it would be possible to evaluate the severity of injury based on a comparison of this initial peak with different published thresholds. For instance, the maximum ICP value due to wall impact under the blast of 95g of HE in the closed space environment (151.0 kPa, Figure 46a) was less than the ICP threshold (235 kPa), indicating a lower possibility of injury based on this parameter. The maximum shear stress for the wall impact in a closed space environment, however, was 14 kPa (Figure 46c) and was, therefore, clearly in the range of the injury threshold for this parameter (8 to16 kPa) introduced by Anderson et al. (81). As noted previously, and in contrast to the impact trauma just discussed, the severity of the PBI in a confined space depended not only on the initial encounter with the shockwave, but also on the full evolution of reflected waves over a period of 15 ms or more.

Although the conclusions in this chapter were based on a limited number of scenarios, the results were likely to be valid for any open, or closed space circumstances. The results showed that the severity of PBI was higher than TeBI in both spaces and that the seriousness of the PBI was dramatically increases in confined spaces. The findings were similar to the conclusions made in a previous whole-body PBI analysis of several blast victims in both open and confined spaces conducted by Leibovici (3). The results could be also compared with the conclusions of Sevagan et al. (58) in both blunt and blast impact scenarios.

CHAPTER 9. CONCLUSIONS AND FUTURE WORKS

The first part of this thesis was dedicated to brain tissue characterization. Linear and QLV models were implemented to explain the response of brain tissue samples. Using the QLV theory, a strong linear correlation was found between the short-term and long-term behaviors of porcine brainstem tissue. The short-term stress for our porcine brainstem samples was 11 times larger than the long-term stress, similar for all initial strain levels. This finding is beneficial, as the short-term stress can be estimated by experimentally measured long-term stress on the tissue. Additionally, it was found that the reduced relaxation modulus varied with strain. This finding suggests that the characterization of brain tissue using the QLV theory at only one strain amplitude may not be applicable for a wide range of tissue deformations. Multiple strain amplitude experiments must be performed to calculate a reasonable set of constants.

As a main limitation, the study did not show that the instantaneous and long-term stresses were purely elastic, especially for the instantaneous stresses measured indirectly using QLV. This deserves further investigation. Also, the irregular geometries of the brainstem samples, varying from sample to sample, may have affected the estimated constants of the QLV model. More experiments are needed on brain tissue with regular geometries to address the performance of the QLV model. Our stress relaxation experiments were conducted at only one initial strain rate. To find the limits of the QLV theory for a wide range of strain values, similar stress relaxation experiments needs to be performed at different test speed strain rates. An understanding of the role of the test speed may contribute to a better understanding of the theory. Perhaps using a unified model to determine the relaxation constants on all six strain amplitudes simultaneously may lead to a more robust estimation of relaxation constants over a large range of strains.

The second part of the thesis described computational investigation on the effect of blast loads on human brain with a focus on confined spaces where reflections off walls may intensify the level of transferred mechanical loads to the brain. It was found that the blast overpressure on the head was magnified by almost four times with the maximum at corners, and as such the brain could experience a higher level of injury. In terms of the severity of blast load transferred to the brain, head-blast interactions were compared in confined as well as open spaces. In the open space, the head experienced a simple pressure waveform that vanished after a few milliseconds. In the confined space, on the other hand, the head tolerated a complex pressure waveform with several peaks, some of which were larger than the single peak found in the open space. More importantly, the duration of the pressure wave remaining on the head was considerably larger than in the open space. The brain PBI and TeBI were compared in a case study and found that PBI was considerably more severe than TeBI in both open and confined spaces.

The main limitation of the computational studies was a lack of experimental data to validate our modeling. The study compared the results of pressure shockwaves with experimental data in a confined space, showing that the pressure, computationally generated in the air domain, was acceptable. However, the study was not able to verify whether the pressure generated on the skull and in the brain were accurate. There are several factors that may play an important role in the accuracy of the modeling, such as element type and size, the ratio of the element size in both the air domain and the structure at their interface, and material properties of the solid structure that is hit by blast pressure waves. Further experimental studies on dummy head models should be conducted to verify the computational studies. Due to technical limitations in modeling a torso attached to the head, the effect of torso and reflections off the body were ignored. To add a torso to the computational modeling, the air domain should be several times larger, leading to generating millions of small elements that made it impossible to investigate the influence of the rest of the body. The effect of torso may be more pronounced while modeling the translational effect of the blast wind for TeBI. The effect of torso should be considered as a future work to more realistically address the blast-head interactions in confined spaces. Also, the walls of confined spaces were considered as rigid in this study. In reality, however, the reflections might be weaker than what were reported, because material properties of walls are not rigid, showing reflection attenuation. This suggests the use of appropriate material properties for walls to be able to absorb a portion of the pressure wave reflections. This also needs to be studied as a future work.

REFERENCES

1. Edri I, Savir Z, Feldgun VR, Karinski YS, Yankelevsky DZ, 2010. On blast pressure analysis due to a partially confined explosion: 1. Experimental studies. International Journal of Protective Structure **2:**1-20.
2. Humphreys I, Wood RL, Phillips CJ, Macey S, 2013. The costs of traumatic brain injury: a literature review. ClinicoEconomics and outcomes research: CEOR **5:**281.
3. Leibovici D, Gofrit O, Stein M, Shapira S, Noga Y, Heruti R, Shemer J, 1996. Blast injuries: bus versus open-air bombings- A comparative study of injuries in survivors of open-air versus confined-space explosions. Journal of Trauma **41**(6)**:**1030-1035.
4. Faul M, Likang X, Wald M, Coronado V, 2010. Traumatic Brain Injury in the United States: Emergency Department Visits: Hospitalizations and Deaths 2002–2006.
5. Babbs CF, 2005. brain motion and deformation during closed head injury in the presence of cerebrospinal fluid. Journal of Mechanics in Medicine and Biology **6**(4)**:**349-371.
6. Javid S, Rezaei A, Karami G, 2014. A micromechanical procedure for viscoelastic characterization of the axons and ECM of the brainstem. Journal of the Mechanical Behavior of Biomedical Materials **30:**290-299.
7. Willinger R, Kang H, Diaw B, 1999. Three-dimensional human head finite-element model validation against two experimental impacts. Annals of Biomedical Engineering **27:**403-410.

8. Mahinda H, Murty O, 2009. Variability in Thickness of Human Skull Bones and Sternum–an Autopsy Experience. Journal of Forensic Medicine and Toxicology **26**(2)**:**26-31.

9. Martini F, 2005. Human anatomy-/Frederic H. Martini, Michael J. Timmons, Robert B. Tallitsch; with William C. Ober...[etc.]. San Francisco, PA [etc.]: Pearson/Benjamin Cummings.

10. Estes MS, 1969. Mechanical response of brain in free standing compression. In: University WV (ed.) Master Thesis, Morgantown, WV, USA.

11. Galford J, McElhaney J, 1970. A viscoelastic study of scalp, brain, and dura. Journal of Biomechanics **3:**211-221.

12. Bilston LE, Lawrence ET, 1996. The mechanical properties of the human cervical spinal cord in vitro. Annals of Biomedical Engineering **24:**67-74.

13. Donnely BR, Medige J, 1997. Shear properties of human brain tissue. Journal of Biomechanical Engineering **119:**423-432.

14. Miller K, Chinzei K, 1997. Constitutive modeling of brain tissue: experiment and theory. Journal of Biomechanics **30:**1115-1121.

15. Hrapko M, van Dommelen JAW, Peters GWM, Wismans JSHM, 2006. The mechanical behaviour of brain tissue: large strain response and constitutive modeling. Biorheology **43:**623-636.

16. Laksari K, Shafieian M, Darvish K, 2012. Constitutive model for brain tissue under finite compression. Journal of Biomechanics **45:**642-646.

17. Prevost TP, Balakrishnan A, Suresh S, Socrate S, 2011. Biomechanics of brain tissue. Acta Biomaterialia **7**(1)**:**83-95.

18. Miller K, 2001. How to test very soft biological tissue in extension? Journal of Biomechanics **34:**651-657.

19. Arbogast K, Margulies S, 1998. Material characterization of the brainstem from oscillatory shear tests. Journal of Biomechanics **31:**801-807.

20. Arbogast K, Meaney D, Thibault LE, 1995. Biomechanical characterization of the constitutive relationship for the brainstem. SAE Technical Paper.

21. Ning X, Zhu Q, Lanir Y, Margulies S, 2006. A transversely isotropic viscoelastic constitutive equation for brainstem undergoing finite deformation. Journal of Biomechanics **128:**925-933.

22. Mendis KK, Stalnaker RK, Advani SH, 1995. A constitutive relationship for large deformation finite element modeling of brain tissue. Journal of Biomechanical Engineering **117:**279-285.

23. Ruan JS, Khalil T, King AI, 1994. Dynamic response of the human head to impact by three-dimensional finite element analysis. Journal of Biomechanical Engineering **116**(1)**:**44-50.

24. Claessens M, Sauren F, Wismans J, 1997. Modeling of the Human Head Under Impact Conditions: A Parametric Study. SAE Technical Paper.

25. Willinger R, Baumgartner D, 2003. Human head tolerance limits to specific injury mechanisms. International Journal of Crashworthiness **8:**605-617.

26. Zhang L, Yang KH, King AI, 2004. A Proposed Injury Threshold for Mild Traumatic Brain Injury. Journal of Biomechanical Engineering **126:**226-236.

27. Horgan TJ, Gilchirst MD, 2003. The creation of three-dimensional finite element models for simulating head impact biomechanics. International Journal of Crashworthiness **8**(3)**:**1-14.

28. Taylor PA, Ford CC, 2009. Simulation of blast-induced early-time intracranial wave physics leading to traumatic brain injury. Journal of Biomechanical Engineering **131**.

29. Dirisala V, Karami G, Ziejewski M, 2012. Effects of neck damping properties on brain response under impact loading. International Journal for Numerical Methods in Biomedical Engineering **28:**472–494.

30. Salimi Jazi M, Rezaei A, Karami G, Azarmi F, Ziejewski M, 2013. A computational study of influence of helmet padding materials on the human brain under ballistic impacts. Computer methods in biomechanics and biomedical engineering**:**1-15.

31. Findley W, Lai J, Onaran K, 1989. Creep and relaxation of nonlinear viscoelastic materials: with an introduction to linear viscoelasticity. Dover Publications, Mineola, NY.

32. Brands DW, Bovendeerd PH, Wismans JS, 2002. On the potential importance of non-linear viscoelastic material modeling for numerical prediction of brain tissue response: test and application. Stapp Car Crash Journal **46:**103-121.

33. Galford JE, McElhaney JH, 1970. A viscoelastic study of scalp, brain, and dura. Journal of biomechanics **3**(2)**:**211-221.

34. Brands IDWA, 1998. Constitutive modeling of brain tissue: Literature review.

35. Tamura A, Hayashi S, Watanabe I, Nagayama K, Matsumoto T, 2007. Mechanical characterization of brain tissue in high-rate compression. Journal of Biomechanical Science and Engineering **2**(3)**:**115-126.

36. Rashid B, Destrade M, Gilchrist MD, 2012. Mechanical characterization of brain tissue in compression at dynamic strain rates. Journal of the Mechanical Behavior of Biomedical Materials **10:**23-38.

37. El Sayed T, Mota A, Feraternali F, Ortiz M, 2008. A variational constitutive model for soft biological tissues. Journal of Biomechanics **41:**1458-1466.

38. Kohandel M, Sivaloganathan S, Tenti G, Drake JM, 2006. The constitutive properties of the brain parenchyma Part 1. Strain energy approach. Medical Engineering & Physics **28:**449-454.

39. Guth E, Wack PE, Anthony RL, 1946. Significance of the equation of state for rubber. Journal of Applied Physics **17:**347-351.

40. Fung YC, 1993. Biomechanics: Mechanical properties of living tissues. Springer, New York.

41. Toms K, Dakin GJ, Lemons JE, Eberhardt AW, 2002. Quasi-linear viscoelastic behavior of the human periodontal ligament. Journal of Biomechanics **35**(10)**:**1411-1415.

42. Abramowitch SD, Woo SL, 2004. An improved method to analyze the stress relaxation of ligaments following a finite ramp time based on the quasi-linear viscoelastic theory. Journal of Biomechanical Engineering **126**(1)**:**92-97.

43. Shafieian M, Darvish K, Stone JR, 2009. Changes to the viscoelastic properties of brain tissue after traumatic axonal injury. Journal of Biomechanics **42:**2136-2142.

44. Pervin F, Chen WW, 2009. Dynamic mechanical response of bovine gray matter and white matter brain tissues under compression. Journal of Biomechanics **42**(6)**:**731-735.

45. Leonardi AD, Bir CA, Ritzel DV, VandeVord PJ, 2011. Intracranial pressure increases during exposure to a shock wave. Journal of Neurotrauma 85-94.

46. Ommaya AK, 1995. Head injury mechanisms and the concept of preventive management: A review and critical synthesis. Journal of Neurotrauma **12:**527-546.

47. Ward C, Chan M, Nahum A, 1980. Intracranial pressure–a brain injury criterion. SAE Technical Paper.

48. Versace J, 1971. A review of the severity index. SAE Technical Paper.

49. Zuckerman S, 1940. Experimental study of blast injuries to the lungs. Lancet**:**219-224.

50. Kluger Y, Nimrod A, Biderman P, Mayo A, Sorkin P, 2007. The quninary pattern of blast injury. American Journal of Disaster Medicine **2:**21-25.

51. Ritzel DV, Park KH, Roseveare J, Rude G, Sawyer TW, 2011. Experimental Blast Simulation for Injury Studies RTO Human Factors and Medicine Panel (HFM) Symposium, Halifax, Canada.

52. Moss WC, King MJ, Blackman EG, 2009. Skull flexure from blast waves: a mechanism for brain injury with implications for helmet design. Physical Review Letters **103:**10–108702.

53. Chafi MS, Karami G, Ziejewski M, 2010. Biomechanical assessment of brain dynamic responses due to blast pressure waves. Annals of Biomedical Engineering **38**(2)**:**490-504.

54. Ganpule S, Alai A, Plougonven E, Chandra N, 2012. Mechanics of blast loading on the head models in the study of traumatic brain injury using experimental and computational approaches. Biomechanics and Modeling in Mechanobiology **12**(3)**:**511-531.

55. Chaloner E, 2005. Blast injury in enclosed spaces, all doctors should know the basic management of patients injured by explosive blast. BMJ **331:**119.

56. De Candole CA, 1967. Blast injury. Canadian Medical Association Journal **96:**207-214.

57. Zhang L, Sharma S, 2009. Computational modeling of causal mechanisms of blast wave induced traumatic brain injury - a potential tool for injury prevention. Wayne State University, Detroit, MI.

58. Sevagan G, Zhu F, Jiang B, Yang KH, 2013. Numerical simulations of the occupant head response in an infantry vehicle under blunt impact and blast loading conditions. Proceedings of the Institution of Mechanical Engineers, Part H: Journal of Engineering in Medicine **227**(7)**:**778-787.

59. Rezaei A, Jazi MS, Javid S, Karami G, Ziejewski M, 2014. Confined blasts, and the impact of shock wave reflections on a human head and the related traumatic brain injury. International Journal of Experimental and Computational Biomechanics **2**(3)**:**205-222.

60. Rezaei A, Salimi Jazi M, Karami G, 2014. Computational modeling of human head under blast in confined and open spaces: primary blast injury. International journal for numerical methods in biomedical engineering **30**(1)**:**69-82.

61. Rezaei A, Salimi Jazi M, Karami G, Ziejewski M, 2014. A computational study on brain tissue under blast: primary and tertiary blast injuries. International journal for numerical methods in biomedical engineering.

62. Thomas LM, Roberts VL, Gurdjian ES, 1966. Experimental intracranial pressure gradients in the human skull. Journal of Neurology, Neurosurgery and Psychiatry **29:**404-411.

63. Ruan JS, Khalil T, King AI, 1993. Finite element modeling of direct head impact. SAE Technical Paper**:**69-81.

64. Willinger R, Taled L, Pradore P, 1995. Head biomechanics: from the finite element model to the physical model IRCOBI, Brunnen, Switzerland, pp 245-260.

65. Willinger R, Kang H, Diaw B, 1999. Three-dimensional human head finite-element model validation against two experimental impacts. Annals of Biomedical Engineering **27:**403-410.

66. Kleiven S, Hardy WN, 2002. Correlation of an FE model of the human head with local brain motion– consequences for injury prediction. Stapp Car Crash Journal**:**123-143.

67. Nahum AM, Smith R, Ward C, 1977. Intracranial pressure dynamics during head impact. SAE Technical Paper.

68. Salimi Jazi M, Rezaei A, Karami G, Azarmi F, Ziejewski M, 2013. Effects of attached body on biomechanical response of the helmeted human head under blast Proceedings of the ASME 2013, San Diego CA, USA.

69. Fletcher ER, Bowen IG, 1966. Blast Induced Translational Effects, Albuquerque, New Mexico.

70. LS-DYNA, 2007. LS-Dyna keyword user's manual Ver. 971. Livermore Software Technology Corporation, pp 18.13(INITIAL) and 50(MAT).

71. Dobratz BM, Crawford PC, 1985. LLNL Explosive Handbook, Properties of Chemical Explosive and Explosive Stimulants. Lawrence Livermore National Laboratory, California.

72. Larcher M, 2007. Simulation of the effects of an air blast wave. JRC Technical Notes, Institute for the Protection and Security of the Citizen.

73. Chafi MS, Karami G, Ziejewski M, 2009. Numerical analysis of blast-induced wave propagation using FSI and ALE multi-material formulations. International Journal of Impact Engineering **36:**1269-1275.

74. Roberts JC, Harrigan TP, Ward EE, Taylor TM, Annett MA, Merkle AC, 2012. Human head-neck computational model for assessing blast injury. Journal of Biomechanics **45:**2899-2906.

75. Troseille X, Tarriere C, Lavaste F, Guillon F, Domont A, 1992. Development of a FEM of the human head according to a specific test protocol. SAE Technical Paper**:**235-253.

76. Hardy WN, Foster C, Mason M, Yang K, King A, Tashman S, 2001. Investigation of head injury mechanisms using neutral density technology and high-speed biplanar x-ray. Stapp Car Crash Journal **45:**337-368.

77. Chafi MS, 2009. Biomechanical Analysis of Blast-induced Traumatic Brain Injury Using Multiscale Brain Modeling. ProQuest.

78. Rezaei A, Karami G, Ziejewski M, 2014. Examination of Brain Injury Thresholds in terms of the Severity of Head Motion and the Brain Stresses, International Neurotrauma Letter.

79. Henn HW, 1998. Crash tests and the head injury criterion. Teaching Mathematics and Its Applications **17**(4)**:**162-170.

80. Ward C, Chan M, Nahum A, 1980. Intracranial pressure–A brain injury criterion. SAE Technical Paper.

81. Anderson RWG, Brown CJ, Blumbergs PC, Scott G, Finney JW, Jones NR, A.J. M, 1999. Mechanisms of axonal injury: An experimental and numerical study of a sheep model of head impact IRCOBI, Sitges, Spain, pp 107-120.

82. Sarvghad-Moghaddam H, Jazi MS, Rezaei A, Karami G, Ziejewski M, 2015. Examination of the protective roles of helmet/faceshield and directionality for human head under blast waves. Computer methods in biomechanics and biomedical engineering **18**(16)**:**1846-1855.